THE UNIVERSITY OF
WARWICK

University of Warwick institutional repository: http://go.warwick.ac.uk/wrap

**A Thesis Submitted for the Degree of PhD at the University of Warwick**

http://go.warwick.ac.uk/wrap/63943

This thesis is made available online and is protected by original copyright.

Please scroll down to view the document itself.

Please refer to the repository record for this item for information to help you to cite it. Our policy information is available from the repository home page.

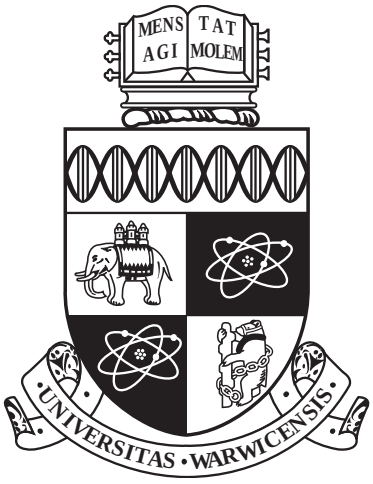


# The development of magnetic granulometry for application to heterogeneous catalysts.

by

**Robert Michael Cook**

**Thesis**

Submitted to the University of Warwick

for the degree of

**Doctor of Philosophy**

**Department of Physics**

May 2014

THE UNIVERSITY OF
WARWICK

# Contents

# Acknowledgments

At the beginning of this PhD I had no idea the level of challenge I had agreed to in trying to convert an undergraduate degree in Chemistry into a PhD in Physics, but for the opportunity I will be forever grateful to my supervisor Martin Lees. Over this 4 year period Martin has taught me more about magnetism, pedantry, and the use of the Oxford comma than would have been possible through any other means.

I must also take this opportunity to thank my range of industrial collaborators from within Johnson-Matthey and, in particular, thank Peter Ellis, Laura Ashfield, and Daniel Cairns for the numerous discussions and invaluable meetings. They have been a bastion of Chemistry and practicality in a world dominated by blue sky physicists.

Alongside this team I would also like to thank the various academics I have had the pleasure to work alongside, including the comedy double act of Don Paul & Charles Dewhurst (without whom I may have returned from the ILL with slightly more sanity but distinctly less data), the scattering duo of Tom Hase & David Walker as well as Tom Orton, without whom this thesis would contain significantly less data. I would also like to extend my thanks to Oleg Petrenko, Geetha Balakrishnan, and Paul Goddard for not raising the Christmas meal of 2010 more than once a year.

A PhD thesis requires more than academic support, and I would like to take this opportunity to thank numerous friends including Chris Collins, Duncan Chase, Matthew Breeze, and Emma Costerton without whom escape from the world of academia would have been few, far between and slightly more sober. In a similar vein I must thank my fellow students, choosing to name Michael Smidman (who still cannot catch a frisbee), Mohammed Saghir (who is looking trimmer by the day), Andrew Clough (may his arms one day be fixed), Olga Young (HRH Crazy Cat Lady), Kevin McAughey (may he never get sunburn), James Richardson-Bullock (who owned a paisley shirt), Daniel Pearce (a continuous source of snow based fun) and Rob Hughes (the reason for far too many good/bad ideas) among many.

In closing I must thank my family for their continued support and understanding that, yes, I am still alive I just forgot to phone home. They have been a continuous supply of unconditional love, free food, and guidance - I love you all.

This work was supported by the Engineering and Physical Sciences Research Council and by Johnson-Matthey plc.

# Declarations

The work presented in this thesis was carried out by myself with the exception of the synthesis of the catalytic materials presented in chapter 4 and the collection of data for gas adsorption isotherms and degree of reduction, all of which had been carried out prior to the commencement of the studentship by Johnson-Matthey. The research was carried out in the Department of Physics at the University of Warwick, at the Johnson-Matthey Technology Centre, Sonning Common or at the Institut Laue-Langevin, Grenoble, France. In all cases I was either the sole experimentalist or a leading member of the experimental team, with the experimental work taking place in the period of October 2010 to June 2014. No part of this work has been submitted for examination at any other institute.

Some of the work described in this thesis is currently in preparation for publication.

# Abstract

Nano-deposits of Ni and Co, supported on porous oxide materials, serve as heterogeneous catalysts within Johnson-Matthey plc. in the steam reforming and Fischer-Tropsch processes, with the size, shape and dispersity of the metal crystallites linked to the catalytic profile. Here we study the magnetic properties of nickel systems synthesised on the nano-scale, with the aim of developing an industrially viable technique by which the diameter of the nickel species can be evaluated.

A series of nickel nanoparticles, synthesised via the thermal decomposition of $Ni(acac)_2$, are studied as a model for the catalytic systems. The nanoparticles were studied via magnetometry and microscopy to identify the super-paramagnetic and nuclear volume of the particles, respectively. The magnetisation studies demonstrate that the widely used Langevin function based method of particle sizing does not reflect the total nuclear volume, and a surface correction term is introduced based on the low temperature, high applied field magnetisation.

To demonstrate the applicability of the proposed analysis, the study of a series of industrially-viable precipitation catalysts are reported. The catalysts are studied via x-ray diffraction (XRD) and gas adsorption to establish comparable values of crystallite diameter. The values of crystallite diameter determined from the magnetic analysis are demonstrated to be consistent with the range of sizes determined from the XRD and gas adsorption studies, with additional sensitivity to the polydispersity of the crystallites.

During the study of the precipitation catalysts, the magnetic volume was demonstrated to be reduced from the nuclear volume. This behaviour was also confirmed via small angle neutron scattering experiments, which demonstrated a magnetic scattering volume reduced from the nuclear by $\approx$ 1 nm, on the order previously reported for nano-ferromagnetic materials.

Through these studies we have established the methods for determining the surface correction term to magnetic granulometry studies. We have demonstrated that the corrected values are in agreement with the nuclear volumes determined via TEM, gas adsorption and XRD and that our proposed technique for the study of catalyst crystallites requires a short time scale, is insensitive to the catalytic support and is sensitive to the distribution of crystallite diameters.

# List of Figures

# Chapter 1

# Preface and motivation

This thesis details the development of a method for determining the size of nanodeposits of ferromagnetic materials via the study of their magnetic properties. These studies take the form of two main investigations - the study of discrete nickel nanoparticles and the study of supported nickel and cobalt deposits as a mirror for industrial catalysts. Catalysts are used extensively in industrial chemistry settings[1] - originally as a method for increasing yields and speeding up reactions, but increasingly new reaction pathways are being created by novel catalytic materials.[2] All catalysts function by altering the potential energy space of the reaction, allowing the chemical reaction to occur at lower temperatures and pressures, and in some cases allowing for otherwise unfavourable processes to dominate the chemistry (e.g. the creation of chiral molecules[3] and the growth of carbon nanotubes[4]).

This study has been carried out in tandem with the Johnson-Matthey (JM) Process Technologies Group, with experiments performed at both the JM Technology Centre, Reading, and the JM Catalysts, Billingham sites (specialising in laboratory scale and industrial application, respectively). JM is an international chemical company with branches specialising in environmental, automotive and pharmaceutical technologies.[5] The Process Technologies Group focus on the development of catalysts for several prominent industrial methods - most notably the Fischer-Tropsch[6] and steam reforming[7] reactions.

## 1.1 Heterogeneous catalysis

Catalyst system can be broadly divided into two families, heterogeneous and homogeneous catalysts. A homogeneous catalytic material is one in which the catalyst

exists in the same fluid phase as the reagents (generally as part of a solution) acting as a recycled reagent. A common example of this type of system is base catalysis for the hydrolysis of esters, in which the addition of hydroxide ions (e.g. from NaOH) leads to a lower energy reaction pathway, increasing the rate of the reaction and regenerating the hydroxide ion at the end.

Heterogeneous systems, conversely, utilise a catalyst which is in a different phase to the reagents, commonly a solid catalyst and fluid reagents. In comparison to the homogeneous systems, the heterogeneous catalyst does not mix freely with the reagents and hence a porous material is used (e.g. $Al_2O_3$ or $SiO_2$) to support nano-sized deposits of the catalytic material. Due to the small length scale of these nano-deposits they are generally treated as single grains of the catalyst, and hence referred to as crystallites.

### 1.1.1 Fischer-Tropsch

The Fischer-Tropsch (FT) reaction was first developed by Franz Fischer and Hans Tropsch in 1925 as a series of chemical reactions that convert synthesis gas (a mixture of CO and $H_2$) into longer chain hydrocarbons. A typical FT process can be summarised by the general chemical scheme given in equation 1.1.[6]

$$(2n+1)H_2 + nCO \rightarrow C_nH_{(2n+2)} + nH_2O \tag{1.1}$$

In the FT process the chemical reaction occurs while the substituant atoms are adsorbed onto the surface of the catalyst (normally a metallic deposit, e.g. Co, Ni or Fe).[8] The carbon species react, increasing the length of the carbon-carbon chain until the chain desorbs from the surface and the FT reaction terminates.[9] These two processes (propagation and termination) are in constant competition and small changes to the reaction conditions can have a marked effect on the kinetics, changing the catalytic profile (the combination of yield, rate of reaction and selectivity). Aside from the standard variables - temperature, pressure and reagent composition - heterogeneous catalysts add an extra level of complexity to the reaction dynamics, with variations in morphology, crystallite size, support material, degree of reduction and surface chemistry all being linked to the hydrocarbon profile produced.[10]

The interest in the Fischer-Tropsch process is dominated by financial considerations. Petrochemicals have a wide influence on the development of modern society and technology, being the basic starting material for several fuels, lubricants, plastics and paints.[11] However, the dominant source of these materials are currently

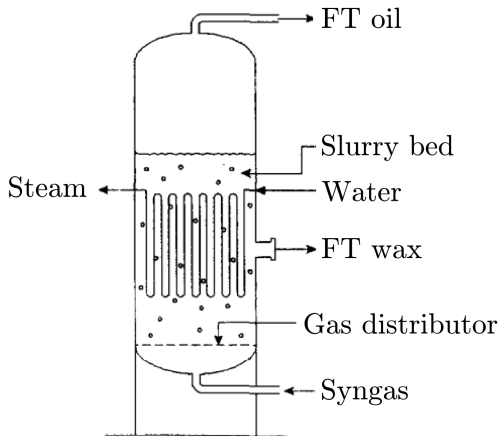


Figure 1.1: Schematic representation of the Sasol slurry bed reactor, reproduced from Jager et al.[15]

naturally occurring oils, such as crude oil, which have a limited availability due to the long time scale associated with their production. As global demand for petrochemical technology has increased, so too has the cost (with a crude oil currently trading at \$110 a barrel)[12] leading to a growing investment in gas-to-liquid (GTL) processes, such as the Fischer-Tropsch process.[13]

The increased industrial interest in Fischer-Tropsch process has been reflected over the previous two decades by the commissioning of several large scale plants (utilising a slurry bed reactor as shown in figure 1.1), notably the Shell Bintu at 12,500 barrels per day (bpd) in 1993 and the Sasol Oryx at 34,000 bpd in 2006.[10] The output from these facilities refers to 1 barrel as equivalent to 210 litres of hydrocarbon which, for GTL technologies, is generally composed of a mixture of lighter hydrocarbons ($C_5$ to $C_8$) and paraffin with a notable reduction in sulphur when compared to crude oil derived hydrocarbons. These plants, however, are due to be dwarfed by the opening of two gas-to-liquid Fisher-Tropsch plants in a joint Shell/Exxon venture due to produce 140,000 and 150,000 bpd, respectively, of GTL oil.[14]

When dealing with a catalytic profile with the complexity of the Fischer-Tropsch process on this scale the techniques used to characterise the catalysts need to be both accurate and rapid, a single hour of halted production can reflect a large financial loss.

### 1.1.2 Steam reforming

Steam reforming, like the Fischer-Tropsch process, deals with the production of a chemical feedstock and fuel, but unlike FT, the end goal is much simpler - to obtain hydrogen.[16] The development of the hydrogen economy has been on a rapid rise over the previous decade due to the promise of a clean, readily available fuel stock - with hydrogen fuels cells promising to revolutionise transport[17] - but hydrogen is already a key feedstock for the production of ammonia and hydrogenated products.[18]

Steam reforming allows for the production of hydrogen gas from methane, which can be readily formed via cracking from larger, non-profitable hydrocarbons, via a collection of three chemical reactions:

$$CH_4 + H_2O \rightleftharpoons CO + 3H_2 \tag{1.2}$$

$$CH_4 + CO_2 \rightleftharpoons 2CO + 2H_2 \tag{1.3}$$

$$CO + H_2O \rightarrow CO_2 + H_2 \tag{1.4}$$

representing the steam reforming, $CO_2$ reforming and water-gas shift reactions respectively.

Unlike FT, for steam reforming catalysts the catalytic profile is simplified as selectivity is a reduced issue and instead we aim for the optimum yield - achieved when catalyst deactivation (a result of coking, sintering or poisoning of the catalyst)[19] is minimised. While noble metals such as Rh and Ru have the highest activity, Ni is generally the preferred catalyst in an industrial setting due to its reduced cost.[20]

The demands of the steam reforming catalyst differ from the FT catalyst predominantly in terms of the toughness of the catalyst. Steam reforming uses increased temperatures and pressures compared to Co catalysed FT,[21] and hence the physical and chemical robustness of the catalysts is of prominent importance. Changes in particle size can lead to a loss of catalytic performance,[22] affecting the profitability of the plants, or even lead to fire hazards as a result of concentrated catalytic activity.

### 1.1.3 Effect of crystallite size on Fischer-Tropsch and steam reforming

Investigations into the FT and steam reforming processes have addressed many of the variables discussed in the previous sections, however, a reliable method for determining the metallic crystallite size on a short time scale poses an interesting challenge. However, before we address this size issue we need to consider why, in particular, the crystallite size is of interest.

The simplest reason for an interest in catalyst crystallite size is due to the surface component of heterogeneous catalysis. As the chemical reaction occurs at the catalyst surface, a reduction in catalyst crystallite diameter will lead to a higher surface area for the same cost of material. While, in theory, this would suggest the aim would be to produce the smallest diameter crystallites possible this is not necessarily true. From a purely thermodynamic perspective, the rate of a reaction needs to be controlled. In the case of an exothermic reaction, if the rate of reaction increases, local heating will occur, leading to the development of hot spots in the catalytic material. The creation of hot spots would both shift the reaction parameters (pressure and temperature) and could lead to physical and chemical alterations in the catalyst (e.g. sintering and redox activity), as well as possible degradation of the catalyst support. The ideal crystallite size will be dictated by the desired catalytic profile, however, some trends have been identified.

For the FT process, a study of cobalt supported on carbon nanotubes[23] has demonstrated a marked decrease in activity when the crystallite diameter is reduced below $\approx 7$ nm, while above this value it is unaffected. Activity is not, however, the only concern. The same study followed variations in the selectivity and found that this size also represented a switch in selectivity, with larger particles favouring longer, $C_{5+}$ species with an increased likelihood of olefin (unsaturated) carbon chains, while the smaller particles favoured shorter, paraffin (saturated) carbon chains.

Steam reforming, however, generally utilises a harsher physical environment, with higher temperatures and pressures than the Co catalysed FT process. In these conditions it is the deactivation of the Ni catalysts that needs to be prevented, in order to obtain the longest active time per Ni crystallite. Smaller nickel crystallites have been shown to be less prone to the build up of surface carbon, known as "coking", which is liked to the deactivation of a catalyst.[24] This build up of carbon can be reversed by increasing the steam content of the reactive gas mixes.

The current sizing techniques with a short enough time scale to be industrially

viable (x-ray diffraction and gas absorption) only give a bulk average diameter.[24;25] Similarly, the technique which is distribution sensitive (transmission electron microscopy, TEM) requires highly specialised equipment, a long time period (for both sample preparation and to reflect the average properties) and offers poor resolution for supported materials.[21;26]

So, the size of the heterogeneous catalyst deposits has been demonstrated to have an effect of the reliability and profitability of the chemical process, but the current techniques do not offer a sensitivity to poly-dispersity on a short enough time scale to be industrially viable. A possible alternative method is magnetometry which is rapid, significantly simpler for operational training and sample preparation than TEM and offers a sensitivity to poly-dispersity for ferromagnetic nanoparticles.

# Chapter 2

# Introduction

The use of magnetometry to study catalyst system has previously been considered, with several publications exploring the magnetic properties of the catalysts,[27] focusing on changes in magnetisation with reaction with different feed gasses.[28] However, it is possible that the catalytic crystallites will behave, magnetically, like their equivalent nanoparticles and, if this is true, we can apply the approaches used for analysing the link between physical and magnetic properties currently applied to recording media[29;30;31] and magneto-hyperthermia medical treatments.[32;33]

Before we consider the theoretical background to magnetism, on both the bulk and nano scale, it is important to address how the field of nano ferromagnetic materials developed, and what challenges still exist.

## 2.1 Magnetic investigations of ferromagnetic nano-particulates

Investigations into ferromagnetic materials reduced to the nanometre scale have their roots in the experimental work of Elmore,[34] in which he studied the magnetic properties of solution suspended ferromagnetic colloids, and its support of the earlier theoretical work of Frenkel and Dorfman.[35] Elmore's work served two purposes, i) to identify that nano-particles of ferromagnetic materials can exist as "single-domain" nanoparticles and ii) to liken the response to an applied magnetic field to a modified form of the Langevin curve which describes atomic paramagnetic materials.

The early studies focused on determining the average moment per atom via a comparison of the saturation magnetisation and mass of magnetic materials and hence, alongside the average moment per particle from the Langevin analysis, pre-

dict an average particle size. However, these investigations were limited to liquid suspensions as the precipitation of nano-particles led to the formation of clusters, resulting in an increase in the inter-particle magnetic interactions and a loss of the reversible magnetic behaviour.[36]

The concept of the "single-domain particle" received marked interest for several theoretical studies. Kittel[37] estimated a general upper limit to the single domain particle size of $\approx 150$ Å prior to more rigorous studies by others,[38;39] in which the critical size was linked to individual material properties, including the particle shape, the strength of the intra-particle ferromagnetic exchange, and the saturation magnetisation. However, it was during this period that Néel[40] determined that the smallest of the particles could undergo a magnetic analogue to Brownian motion, with spontaneous reversal and rotation of the magnetic moment provoked by thermal fluctuations. These thermally fluctuating particles possessed a magnetic susceptibility akin to that observed by Elmore[34] even at high concentrations, but only at high temperatures.

Alongside investigations into the thermally driven properties of the ferromagnetic nano-particulates a theoretical study by Stoner and Wohlfarth[41] produced a description of the hysteretic magnetic behaviour of a ferromagnetic nanoparticle without such thermal fluctuations. The model predicts that the coercivity (the applied magnetic field, $H$, require to reverse the magnetisation) and remanent magnetization (the magnetisation post magnetic saturation at $H = 0$) of the particle at a given temperature can be tuned by several parameters including particle shape, size and surface properties. Nanoparticles can hence offer a much higher coercivity than their bulk counterparts (see figure 2.1) as well as control of the coercivity with the system temperature and has led to several prominent developments over the previous 60 years, leading directly to application in information storage, ferrofluids and high energy electronics.[42]

Applications of ferromagnetic nano-particles have also begun to spread beyond the scope of engineering and physics, with increasing biological applications.[43] Nano-science in general is appealing to inter-disciplinary endeavours that include a biological aspect due to the reduced scale (cell: 10 - 100 $\mu$m, virus: 20 - 450 nm, protein 5 - 50 nm, gene: 2 by 10 - 100 nm) allowing for close proximity between the nano-particle and the biological entity. The addition of magnetic properties adds a remarkable opportunity for applications, allowing for the particle to be controlled via an external magnetic field and hence used for the targeted delivery of a biological package such as an anti-cancer drug.[44]

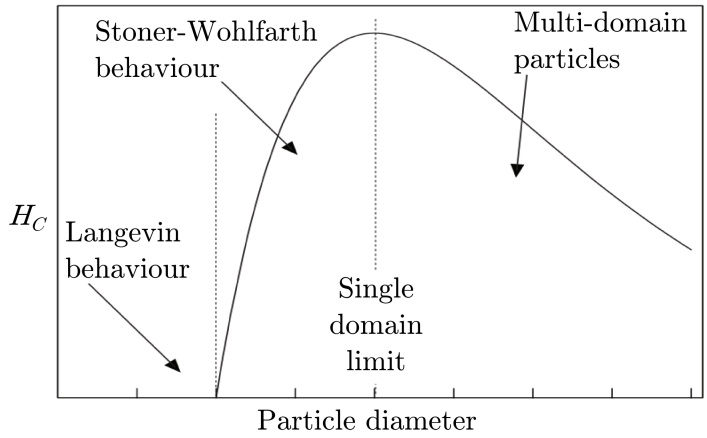


Figure 2.1: Variation in coercive field ($H_C$) with particle diameter at room temperature, reproduced from Chernavskii et al.[27]

The utility of ferromagnetic nano-materials as a biologically compatible component, however, extends beyond targeted delivery due to the novel thermal properties arising from the earlier studies of thermal fluctuations. Néel's studies of the thermal properties determined the magnetic moment will undergo a magnetic flip (with the flipping rate a function of the system temperature) however, if the moment is driven to reverse at a faster rate by an applied alternating magnetic field a torque is generated between the magnetic moment and the magnetically favourable direction.[45] This torque leads to an excess of energy - released thermally i.e. a localised heating. This magnetically driven heating allows for the use of the particles as hyperthermia agents, leading to remarkable improvements in the treatment of tumours - either via the delivery of a toxic dose of thermal energy or as chemo- and radio-therapy enhancement agents (with localised tissue warming increasing the treatments effectiveness).[46]

The plethora of applications of nano-ferromagnetic materials has meant that the focus of the research has shifted away from the magnetic granulometry associated with the early studies, and is now also concerned with how alterations in particle loading, surface chemistry, and particle morphology effect the magnetic behaviour.[47] One fundamental issue raised by recent studies that will impact the accuracy of granulometry studies has been the possible "dead-layer" structure of the nanoparticles.[48;49] It is common[48;50;51;52] when comparing particle sizes determined from TEM and via magnetic granulometry to arrive at a magnetic moment per particle reduced from the TEM size (assuming the bulk magnetic moment per atom).

This leads to two competing hypotheses, i) a reduction in the magnetic moment per atom, or ii) the outer layer of the particle does not ferromagnetically order with the rest of the particle and hence the moments do not contribute to the "single domain" moment.

A reduction in magnetic volume has been measured on several occasion via small angle scattering techniques e.g. polarisation-analysed small angle neutron scattering (SANS),[53;54;55] however, the behaviour of this outer layer, referred to as the "dead-layer" structure, has not been fully understood. A variety of surface magnetic behaviours can be achieved via the creation of a core-shell nanoparticle structures (most notably the Co/ CoO exchange biased systems[56]). However, even when composed of a single ferromagnetic material a variation in the surface magnetic behaviour has been shown.[57;58] The magnetic behaviour arises due to the fine balance between parameters (including the magneto-crystalline and surface anisotropies, and the inter-particle interactions) which can lead to a range of behaviours.[59;60;42]

The current applications of ferromagnetic nanoparticles do not rely on these surface moments, and hence a development of a correction to the magnetic granulometry technique has been largely overlooked, instead focusing characterisation on the room temperature and reversible magnetic behaviours and novel synthesis methods.[61;62] We believe a closer investigation of the low temperature magnetic behaviour may provide the correction term required to both understand and quantify the "dead-layer" behaviour and hence reflect the size of the total crystallite (as opposed to just the single domain volume) when the magnetic granulometry approach is applied to Fischer-Tropsch and steam reforming catalysts.

### 2.1.1 Interacting nanoparticle studies

One aspect of nanoparticle magnetism that may have an effect on the study of catalyst materials is the effect of inter-particle interactions, and the growth of order between the super-paramagnetic moments. As the inter-particle interactions increase in strength, generally a result of decreasing inter-particle distance, the ensemble of multiple super-paramagnetic moments can form ordered systems - with either a random distribution of inter-particle distances, creating a super-spin glass (SSG) behaviour, or with equivalent inter-particle distances creating a super-ferromagnetic (SFM) behaviour. The recent work involved in this field has been reviewed by Bedanta and Kleemann,[42] with a focus on the growth of interactions as particle loading increases.

The terms super-spin glass and super-ferromagnetic have been used to describe situation in which an ensemble of super-paramagnetic (a species with a moment orders of magnitude larger than an atomic equivalent behaving as a free paramagnet) moments begin to demonstrate an ordered behaviour analogous to the atomic magnetic behaviour. Examples of the typical magnetic responses are shown in figure 2.2, with comparisons between, a) the SSG and spin-glass, and b) the SFM and ferromagnetic $M$ vs $T$ responses. In both cases at temperatures above the associated critical temperature the moments behave as paramagnetic materials with a Curie-Weiss behaviour, with a massively increased moment for the super systems. The super-spin glass (figure 2.2 a) systems typically show a dip in the field-cooled magnetisations at low $T$, however, a frequency dependence in ac-susceptibility studies is a clearer indicator of spin-glass behaviour. The super-ferromagnetic systems (figure 2.2 b) can demonstrate a sharp magnetic response if the preferred orientation of the ensemble ferromagnetic ordering is away from the direction of applied field.

The dominant inter-particle interactions are generally assumed to be either RKKY (Rudderman-Kittel-Kasuya-Yosida) interactions, if the particles posses a conducting pathway to mediate the interaction, or the dipole-dipole interaction. The dipole-dipole interaction can be expressed as,

$$E = \frac{\mu_0}{4\pi r^3}\left[\boldsymbol{\mu}_1.\boldsymbol{\mu}_2 - \frac{3}{r^2}(\boldsymbol{\mu}_1.\boldsymbol{r})(\boldsymbol{\mu}_2.\boldsymbol{r})\right], \tag{2.1}$$

where $\mu_0$ is the vacuum permeability constant and $\boldsymbol{\mu}_1$ and $\boldsymbol{\mu}_2$ are the vectors for the two interacting magnetic dipoles separated by the distance $r$[63] and is generally considered too weak to lead to an ordering above a few $mK$. However, this is for systems with an effective moment of $< 10\ \mu_B$, in the case of nanoparticles this moment can increase by a factor of 1,000 with a small equivalent increase in $r$, leading to long range order.

At dilute particle concentrations ($\leq 4\%$ by volume) the inter-particle interactions are generally reported to be too weak to induce a collective state (the SSG or SFM ordering) but can lead to a modification of the energy barriers to magnetic reversal of the single domain moment. This behaviour has been termed the modified super-paramagnetic behaviour and has been demonstrated for a system of Co/Fe nano deposits on an alumina matrix support[64] via ac magnetic susceptibility measurements. The study demonstrated an increased energy barrier to magnetic reversal (compared to the theoretical value for isolated Co/Fe particles) of $\frac{E}{k_B} \approx 450$ K cf. 150 K for the isolated case, but without an associated magnetic field "memory

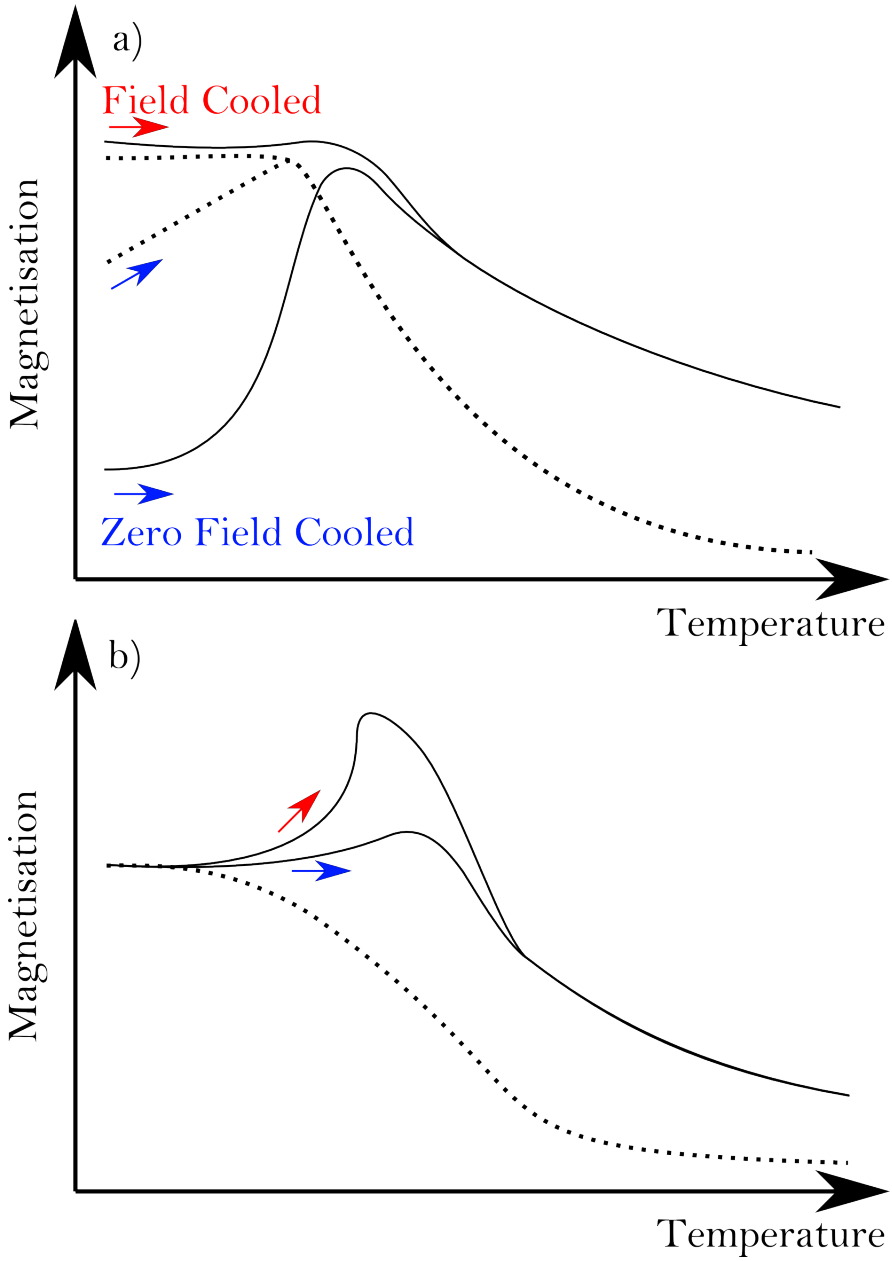


Figure 2.2: The typical magnetic responses of super-paramagnetic systems experiencing inter-particle ordering for a) the super-spin glass (solid line) and the atomic spin glass (dashed) and b) the super-ferromagnetic (solid) and atomic ferromagnetic (dashed) systems.

effect" expected of a SSG system.

Increases in particle loading lead to the creation of the super-spin glass (SSG) state, with the cluster of single domain magnetic moments taking on a cluster behaviour analogous to the traditional spin glass behaviour, more details of which can be found in the review by Binder and Young.[65] The SSG system requires an increased inter-particle interaction in comparison to the modified super-paramagnetic case and a degree of randomness introduced into the system, generally achieved by a random variation in nearest neighbour distances caused by the imperfect packing of poly-disperse nanoparticle samples. The creation of SSG dynamics has previously been followed by measuring the divergence of the time-dependent, ac-susceptibility from the Néel behaviour[66] however, evidence of classic spin glass characteristics such as ageing, memory and rejuvenation[67] are a more reliable identifier. These features can be measured via introducing a wait period during cooling of the sample (when following the variation in magnetisation as a function of temperature) at a temperature below the expected SSG transition before further cooling. On re-heating the sample a sharply defined dip in magnetisation is observed at the wait temperature. Such a "stop-and-wait" protocol has been used to identify "glassy" behaviour in several systems of higher concentration nanoparticles.[68;69]

The increase in inter-particle interactions has a marked effect on the thermal properties of the nanoparticles, and in general increases the energy barrier to the free reversal of the single domain moment. At the tightest particle packing, the inter-particle interactions become so dominant that the array of super-paramagnetic moments can order as an analogue to the traditional ferromagnetic structure. This super-ferromagnetic (SFM) state, first suggested by Mørup,[70] leads to a further thermal transition on cooling of the material (at a lower temperature than the standard super-paramagnetic to "blocked" behaviour) leading to a magnetisation akin to a macro ferromagnetic domain structure, in which neighbouring nanoparticles are aligned but with the ferromagnetic domain structure repeated on an increased scale. The inherent physical difference between the SSG and SFM situation is a question of control. For a SFM the inter-particle magnetic interactions need to lose the random quality inherent in the spin glass systems, leading to a synthetic challenge. SFM has been determined for 1D[71] and 2D[72] systems, using lithography to synthesise arrays of single-domain species with controlled spacing, and eventually for a 3D system[73] (again using an alumina supported $Co_{80}Fe_{20}$ sample) studied via x-ray photo-emission spectroscopy (XPS).

The increase in inter-particle effects and ordering of the single-domain mo-

ments introduce two practical considerations for applications; i) an increased effective energy barrier to the free single-domain moment and ii) limitations on the packing density of the nanoparticles as magnetic storage media (where each "bit" requires an isolated existence). In terms of magnetic granulometry this feature introduces a possibility for determination of inter-crystallite distance if we can determine the variation in behaviour with increasing particle interactions.

### 2.1.2 Surface alterations of nanoparticles

Due to the massively increased contribution of the surface to the overall properties for nano-materials over their bulk equivalents, a plethora of studies have been made both exploring and tailoring the effects of surface states for nanoparticles. A simple reason for introducing surface functionality as a means of preventing the interactions described in section 2.1.1, which may arise from a close packing of the nanoparticles. Nanoparticles systems will generally be designed to avoid agglomeration via a mixture of electrostatic and steric repulsions. Typical methods for preventing agglomeration are the addition of a surfactant system,[74;75] which prevents particle contact as well as controlling particle morphology, or the control of the surface charge.[76] The drawback with the charge stabilisation methods for biological applications is the inherent pH sensitivity, which limits these materials to solution systems and individual organ systems.

As well as acting as an agglomeration preventative, the surface can also impart a chemical resistance to the underlying magnetic material. In the case of metallic systems (e.g. Co, Ni, and Fe) protocols have been developed to create a controlled thickness of the relevant oxide, stabilising the metallic core to further oxidation.[77] This formation of an oxide can lead to more than a simple passivation of the surface. In the case of the Co/CoO system, the antiferromagnetic nature of the CoO can be used as to introduce an exchange bias into the low temperature magnetisation.[56] Exchange biasing allows for the magnetisation of a ferromagnetic material to be shifted with respect to the applied magnetic field, $H$, and hence vary the coercive field and remanent magnetisation.[78] This effect for nanoparticles has been of resounding success in supplying higher coercive fields than previously believed possible from single domain particles and, by varying the thickness of the oxide layer, imparts an extra parameter by which the desired magnetic response can be tailored.[79]

Due to the biological applicability of magnetic nanoparticles there has also been a drive towards the deposition of gold, due to its general low reactivity and the

possibility of functionalisation via the formation of thiol self assembled monolayers.[80] However, the addition of gold to magnetic particles has proved difficult to achieve due to the dissimilar nature of the two surfaces, but has been achieved for iron nanoparticles via several methods.[81;82] One of the more promising of these methods reported the magnetic properties of the iron pre- and post-the addition of gold, demonstrating that the iron-gold particles possess a reversible magnetisation at room temperature and are stable over time (with a magnetic saturation of 96% of the bulk iron value after 4 months of storage).[83]

Catalyst systems will generally employ a metal oxide, such as a silica ($SiO_2$), titania ($TiO_2$), or alumina ($Al_2O_3$), as a support for the metallic system and the catalyst-support interactions can also have an effect on the magnetic properties. Silica has received the most attention as a surface coating material, allowing for protection of the core and electrostatic retardation of agglomeration (see figure 2.3).[84;85;86] Nanoparticles stabilised with an outer layer of silica showed a reduction in the magnetic saturation in comparison to the uncoated particles,[87;88] suggesting either a decrease in the average moment per atom or a weakening of intra-particle interactions leading to the outermost nanoparticle atoms decoupling from the single domain moment.

### 2.1.3 Magnetic catalyst characterisation

Previous studies have been carried exploring the magnetic responses of several catalytic systems used in the the Fischer Tropsch (FT) process, and the magnetically sensitive aspects reviewed extensively by Chernavskii.[27] The magnetic studies of Co based FT catalysts are generally limited to one of 3 issues - the extent of Co reduction, the redox properties of the Co, and the Co crystallite size.

Reduction investigations have been carried out by coupling a magnetometer to a conventional temperature programmed reduction (TPR) apparatus.[89] In conventional TPR the sample is exposed to a continuous flow of hydrogen gas and the reduction in hydrogen measured via a thermal conductivity detector. One problem that arises is that TPR is limited to dilute hydrogen gas (due to the detection method) which results in a marked change in Co reducibility compared to if pure hydrogen is used.[28] The magnetometry methods, however, can use pure hydrogen and, by following changes in the magnetisation at a high applied field (i.e. at magnetic saturation), it is possible to quantify the formation of the metallic Co species as a function of temperature and time. The metallic Co can be discerned from the cobalt

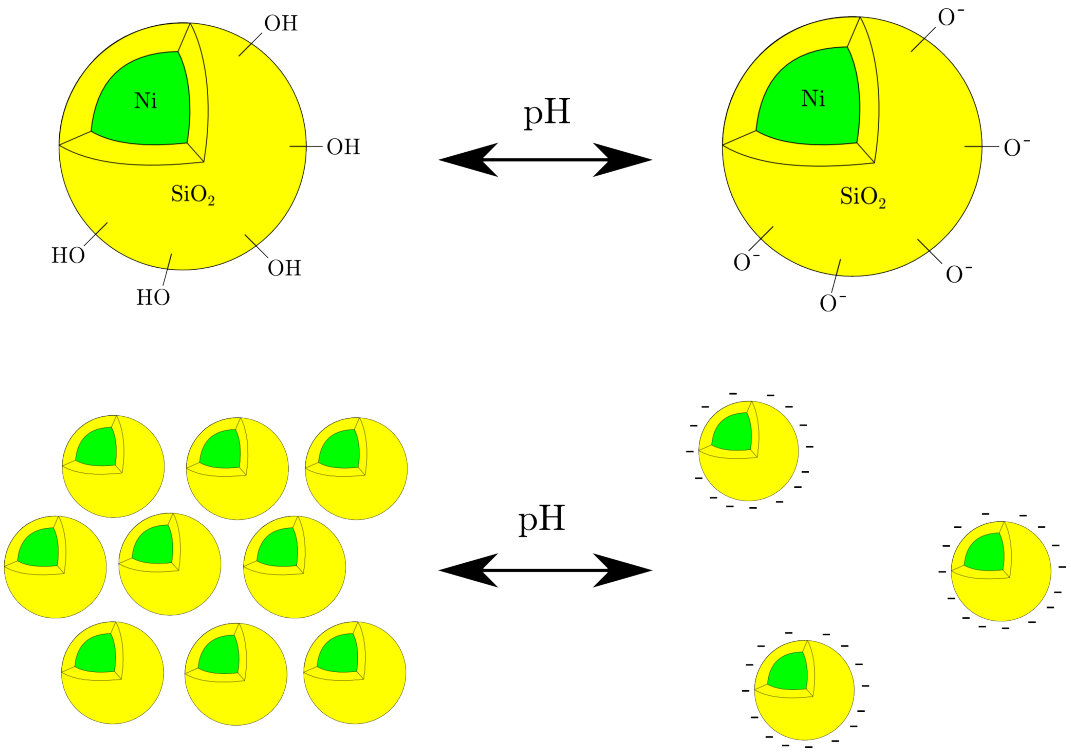


Figure 2.3: Schematic representation of the electrostatic stabilisation of discrete nanoparticles in solution via a silica surface coating. At low pH the surface oxide groups are de-protonated creating a surface charge and hence retarding agglomeration.

oxide species, CoO and $Co_3O_4$, as in the $T$ range of interest (300 to 900 K) the Co is ferromagnetic while the oxides are paramagnetic ($T_{N\ CoO} = 288$ K, $T_{N\ Co_3O_4} = 30$ K, and $T_{C\ Co} = 1400$ K)[27;90;91] and hence possess a reduced magnetic susceptibility. The magnetic reduction technique can also be used in parallel with the standard TPR technique in dilute hydrogen in order to ascertain if the reduction is $Co_3O_4$ to CoO (observed in TPR at $\approx 300$ °C but unobserved magnetically) or the CoO to Co transition (observed in both techniques at $\approx 350$ °C).[92]

The oxidation investigations use the same experimental set-up as the reduction studies with the exception of changing the feed gas from hydrogen to oxygen. While understanding and quantifying the reduction dynamics is key for FT as catalysts will generally be synthesised as an oxide and then reduced, understanding the oxidation dynamics is necessary in order to control deactivation during gas-to-liquid conversion. The oxidation studies have demonstrated a decrease in magnetisation as a function of sample temperature and time, and assume that a decrease in magnetisation reflects a formation of cobalt oxide at the crystallite surface.[27] These studies have shown that, for each temperature, there exists an optimal thickness of oxide, past which the magnetisation will cease to decrease. This optimal thickness increases with oxidation temperature.

The final aspect of catalyst magnetic investigations that have received attention has been the application of the magnetic granulometry techniques. The reversible, super-paramagnetic magnetic response has been modelled via the Langevin function described extensively for isolated nanoparticles, converting the average super-moment into an equivalent volume of metallic cobalt. Several preparations of Co catalysts have been demonstrated to possess the reversible magnetic behaviour indicative of the super-paramagnetic system[89;93;94;95] - focusing on particles in the range 3 - 6 nm. The majority of studies of this form for catalysts have focused primarily on the magnetisation vs applied magnetic field behaviour, avoiding the thermal fluctuations described by Néel. This is purely due to apparatus limitations as the magnetometry systems used for the study of catalytic systems are designed with redox (300 - 900 K) as opposed to cryogenic (2 - 300 K) temperatures in mind. Similarly, the majority of theses studies have been carried out by Chernavskii, using a system with a maximum applied field of $\approx 7$ kOe, significantly lower than the $H_{Max} = 50$ to 70 kOe systems generally available to the equivalent nanoparticle researchers. It is possible there are aspects of the catalyst magnetisation to be explored at these higher fields.

### 2.1.4 Evidence of surface magnetisation effects

Core-shell magnetic behaviour does not necessarily require a change in surface chemistry (e.g. a ferromagnetic core and antiferromagnetic shell). Ferrite nanoparticles have been shown to display a "core-shell" structure consisting of a well ordered magnetic core surrounded by a surface layer of spins randomly frozen in a spin glass-like manner.[96;97]

The presence of the "glassy" surface spin states were identified due to an increase in magnetisation at high applied fields at low temperatures ($H \geq 25$ kOe and $T \leq 50$ K) away from the expected saturated Langevin behaviour. This behaviour was observed in measurements of both magnetisation as a function of field ($M$ vs $H$) and temperature ($M$ vs $T$), however, it is simpler to identify in $M$ vs $T$ data sets at high applied fields as it manifests itself as a deviation from Bloch's law.[98] The core magnetisation at high $T$ still follows the traditional Langevin behaviour, only with a decreased "super"-magnetic moment per particle and magnetic saturation.

Interestingly, it has also been demonstrated that this surface behaviour can be tuned via the variation of the surface chemistry. The addition of a Cu shell to a ferrimagnetic $Fe_2O_3$ nanoparticle has been used to alter the iron oxide surface moments and remove the spin-glass behaviour.[99]

This decoupling of the surface magnetic moments from the core superparamagnetic state is similar to the decrease in magnetisation discussed earlier as the "dead-layer" effect, and a ferrimagnetic behaviour has been previously demonstrated for non-iron metal oxides.[100;101] Analysis of magnetic properties at low $T$ and high $H$ may demonstrate similar magnetic structures that can be used to correct the magnetic granulometry approaches for a "dead-layer" term.

## 2.2 Magnetism in condensed matter

Prior to exploring the possible nano-magnetic models for analysing crystallite size, we need to understand the underlying physical principles of magnetism. The following sections will draw heavily on four main texts by Blundell,[63] Bates,[102] Aharoni,[103] and Stewart.[104]

In classical electromagnetism when a charged species precesses in a circular orbit it generates a magnetic field. The magnitude of the magnetic field produced is dependent on two factors, the charge on the species and the angular momentum it possesses. In condensed matter systems this charged species takes the form of

the electrons, possessing a charge of $-1.602 \times 10^{-19}$ coulomb (C) and total angular momentum, **J**. This total angular momentum, **J**, can be broken down into two components, the orbital angular momentum, **L**, and the spin component, **S**, and the magnitude of **J** is,

$$\mathbf{J} = \mathbf{L} + \mathbf{S}. \tag{2.2}$$

The total angular momentum of the electron gives rise to a magnetic moment, $\mu$, which lies parallel to the orbital angular momentum and the relationship between the two is given by,

$$\mu = g_J \mu_B \sqrt{J(J+1)}, \tag{2.3}$$

where $\mu_B$ is the magnetic moment of the hydrogen $1s^1$ electron ($9.274 \times 10^{-24}$ A m$^2$), $J$ is the magnitude of the total angular momentum vector **J**, and $g_J$ is the Landé g-factor. Each magnetic moment produces a local vector field, the magnetic field, through which it influences other magnetic moments in the surrounding space.

All materials, regardless of their magnetic properties, have a susceptibility, $\chi$, to an applied magnetic field, $H$. When this susceptibility is positive, and the magnetisation, $M$, along the direction of applied field increases with $H$, the material is paramagnetic. In the simplest magnetic system each magnetic moment, $\mu$, has no interactions and $H$ creates a torque, causing the moments to gradually lie in the direction of applied field. As $H$ increases, $M$ increases linearly to begin with before tending to a constant value when all moments lie parallel to $H$ giving a value for the magnetic saturation, $M_S$ ($M_S = \sum \mu$). The $M$ vs $H$ behaviour of a localised paramagnet moment can be derived from either a classical case, giving the Langevin function,

$$\frac{\langle \mu_z \rangle}{\mu} = \coth\left(\frac{\mu B}{k_B T}\right) - \left(\frac{\mu B}{k_B T}\right)^{-1}, \tag{2.4}$$

or for a quantum mechanical system, with quantised values of **J**, giving the Brillouin function,

$$B_J = \frac{2J+1}{2J} \coth\left(\frac{2J+1}{2J} y\right) - \frac{1}{2J} \coth\left(\frac{1}{2J} y\right),$$
$$y = \frac{g_J \mu_B J B}{k_B T}, \tag{2.5}$$

where $J$ is the magnitude of the vector $\mathbf{J}$.

For the case of the quantum mechanical, Brillouin function as $\mathbf{J} \to \infty$, $B_\infty(y) \to L(y)$ and so as the total angular momentum, and hence the magnetic moment, of the system increases a classical model becomes applicable. The Langevin function can be further approximated, in the low applied field case, to a simple linear dependence on $H$,

$$L_{H\to 0}(y) = \frac{M_{H\to 0}(y)}{M_S} \approx \frac{y}{3} = \frac{\mu B}{3k_B T}, \tag{2.6}$$

and from this linear behaviour a magnetic susceptibility, $\chi = \frac{M}{H} \approx \frac{\mu_0 M}{B}$ can be expressed as

$$\chi = \frac{n\mu_0\mu^2}{3k_B T}. \tag{2.7}$$

This behaviour is a statement of the Curie Law - and demonstrates that the magnetic susceptibility is inversely proportional to the temperature.

### 2.2.1 Magnetic ordering

Interesting magnetic phenomena arise from systems in which multiple magnetic moments exist in close proximity, influencing their neighbours preferred orientation, creating magnetic ordering. In the case of the simple atomic paramagnet previously discussed the moments can be considered to exist independently of each other, possess no ordering, and randomly align with no applied magnetic field ($M_{H=0} = 0$). Magnetic moments interact via exchange interactions (e.g. direct exchange or Ruderman-Kittel-Kasuya-Yosida (RKKY) interactions) which express the energetically favourable orientation of neighbouring electrons. A commonly stated model for exchange is the nearest neighbour Heisenberg model, where the spins $\mathbf{S}$ are treated as 3D vectors, with an associated Hamiltonian for the exchange,

$$\hat{\mathcal{H}} = -\sum_{ij} \mathbf{J}_{ij}\mathbf{S}_i.\mathbf{S}_j, \tag{2.8}$$

where $\mathbf{J}_{ij}$ is the exchange constant between the $i^{\text{th}}$ and $j^{\text{th}}$ spins, $\mathbf{S}_i$ and $\mathbf{S}_j$ respectively.

The favoured direction of the exchange is hence based on the sign of $\mathbf{J}$, with a positive exchange constant favouring a parallel alignment of spins and a negative constant an anti-parallel alignment. In general exchange interactions decrease

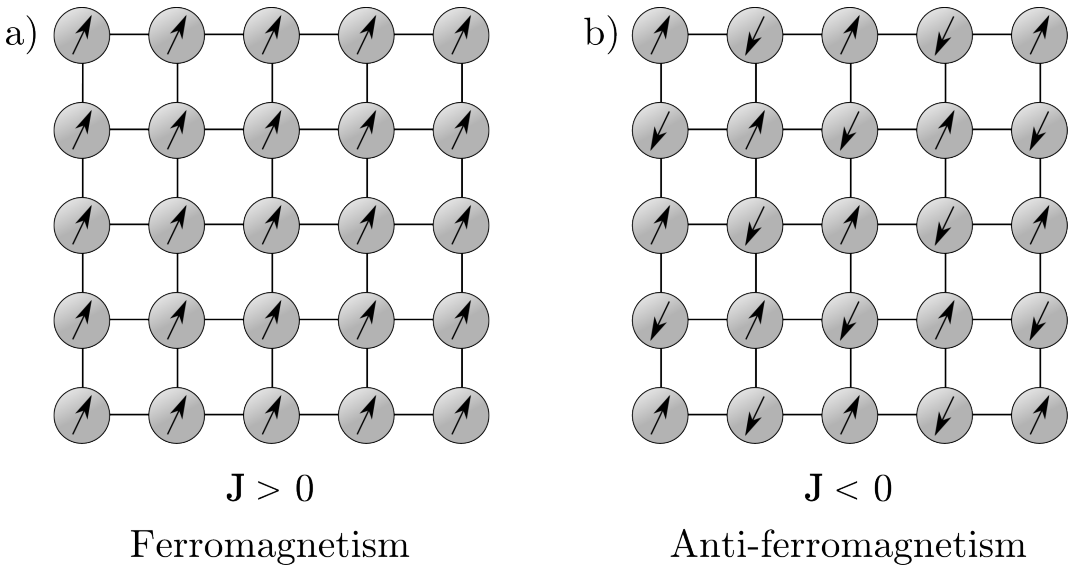


Figure 2.4: Schematic representation of long range magnetic ordering on a 2D square lattice caused by a) strong ferromagnetic ($\mathbf{J} > 0$) and b) antiferromagnetic ($\mathbf{J} < 0$) interactions.

rapidly with increasing distance, ($r^{-3}$ for RKKY and dipole-dipole exchange) so we can assume that nearest neighbour exchanges will dominate, with longer range exchanges ignored for simple systems. When all magnetic moments have the same magnitude these exchanges lead to two forms of magnetic order; $\mathbf{J} > 0$ leads to ferromagnetic ordering with magnetic moments aligned parallel and $\mathbf{J} < 0$ leading to antiferromagnetic ordering with an alternating direction of spins (both of which are illustrated in figure 2.4).

Depending on the mechanism of the exchange interaction the ferromagnetic and antiferromagnetic ordering will be of different strengths; with an associated temperature at which the magnetic moments will possess sufficient thermal energy to overcome the exchange interactions. Above this temperature the moments become disordered; with an associated magnetisation similar to the disordered paramagnetic moments previously discussed. This temperature can be quantified via the Curie-Weiss law,

$$\chi = \frac{C}{T - \theta}, \tag{2.9}$$

in which the Weiss temperature, $\theta$, is positive for a ferromagnet (with $\theta \approx T_C$, the Curie temperature) and negative for a antiferromagnet (with $\theta \approx -T_N$, the Néel

temperature).

The two values, $T_C$ and $T_N$, are the temperature at which the system changes from the ordered to the disordered state and, while $\theta$ is a good indicator of the order of magnitude, it is not necessarily an accurate measurement of the ordering temperature. This is especially true for several antiferromagnetic materials, such as CoO where $T_N$ and $\theta$ are 292 and -330 K respectively. Such a discrepancy is generally explained because the derivation only accounts for interactions which favour anti-parallel alignment of the moments, ignoring longer range ferromagnetic interactions.

### 2.2.2 Itinerant ferromagnetism

The two metals industrially used as the active catalytic metal in Fischer-Tropsch and steam reforming are Co and Ni, respectively, which are well known ferromagnetic materials. However, they posses a non-integer average magnetic moment per atom much smaller than expected from Hund's rules, with experimental values for Co = 1.56 $\mu_B$ atom$^{-1}$ and Ni = 0.61 $\mu_B$ atom$^{-1}$. Clearly, this behaviour is difficult to explain using the localised models previously discussed, and instead is considered to arise from the electron band structure.

To explain the magnetic properties of Ni and Co two features need to be allowed for, the strong crystal field interactions of the 3d system and the band structure of the conduction electrons. Unlike f electron systems, e.g. Gd and Ho, in the 3d system the spin-orbit interactions can be ignored due to the stronger crystal field interactions, leading to a quenching of the orbital angular momentum and reducing equation 2.2 to the simpler expression $\mathbf{J} = \mathbf{S}$. Hence, the magnetisation of the 3d electrons depends purely on the spin character of the electrons, earning these systems the title "spin" magnets.

Having removed the orbital angular momentum term, the band structure arising from the itinerant nature of the 3d elements is simpler to explain. In such systems the band structures can be split between electron states possessing a spin-up and a spin-down character, so that if both bands are occupied equally, see figure 2.5, there is no magnetisation.

An applied magnetic field, $H$, causes the energy of the two spin bands to split - separated by an energy of $\approx 2\mu_B B$. The splitting of the bands then leads to an equivalent depletion in one band and an enrichment in the other of $\frac{1}{2}g(E_F)\mu_B B$ electrons per unit volume. Assuming that each electron adds $1\mu_B$ to the magnetic response we can express this change in density as a magnetisation and hence a

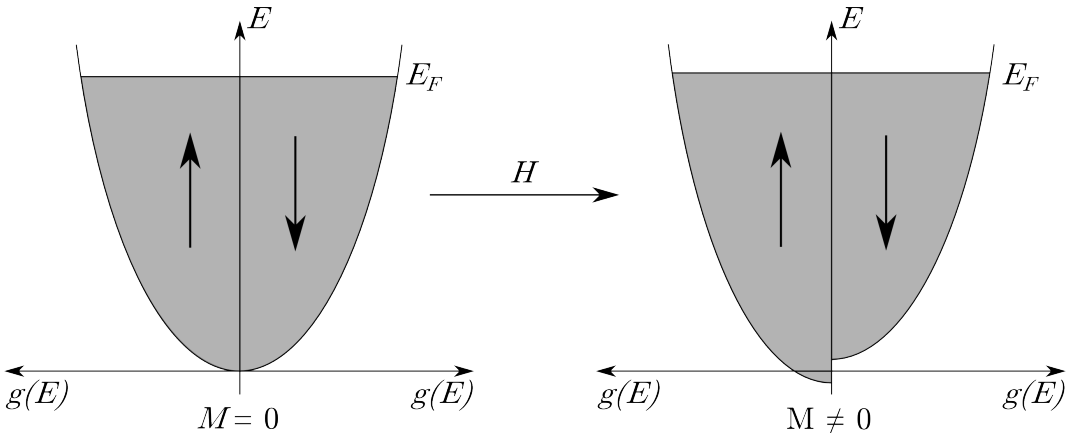


Figure 2.5: Schematic representation of the band splitting arising from an applied magnetic field in a metallic system which leads to the Pauli paramagnetic response. The direction of applied field is parallel with the enriched spin state (spin up for this example).

susceptibility (see equation 2.10).

$$M = \mu_B(n_{spin-up} - n_{spin-down}) = g(E_F)\mu_B^2 B,$$
$$\chi = \frac{M}{H} = \mu_0 \mu_B^2 g(E_F) = \frac{3n\mu_0\mu_B^2}{2E_F}. \tag{2.10}$$

This splitting of the band via an applied magnetic field gives rise to a positive magnetic susceptibility, referred to as Pauli paramagnetism. However, in the case of Co and Ni the nearest neighbour interactions, discussed earlier, also have an effect. To allow for this we can consider an average exchange field, $\lambda M$, which is the result of all the neighbouring interactions. In the case of itinerant systems we have an electron gas which can be magnetised by the local field environment because of the Pauli paramagnetism and in turn the magnetisation of the electron gas creates the exchange field. This effect, referred to on occasion as bootstrapping or a "Pullum vel Ovum" scenario, requires that both the average exchange field, $\lambda$, and the Pauli paramagnetism, $\chi_P$, be large; hence it is not observed for all metals.

A more rigorous derivation of spontaneous band splitting can be achieved by considering the case of a small, spontaneous transfer of electrons from the spin-down band to the spin-up band. We will assume that all electrons in the spin down band with energy higher than $E_F - \delta E$ are transferred to the spin-up band and their spin

flipped. The result of this is moving a number of electrons, $\frac{g(E_F)\delta E}{2}$, and increasing the energy in each case by $\delta E$, giving a cost in kinetic energy as expressed in equation 2.11,

$$\Delta E_{K.E.} = \frac{g(E_F)(\delta E)^2}{2}. \tag{2.11}$$

This transfer of electrons costs kinetic energy, however, the net magnetisation created can interact favourably with the molecular field, $\lambda$, reducing the potential energy. In this hypothetical system we have an electron density in the spin-up band, $n_{up} = \frac{n+g(E)\delta E}{2}$, and an equivalent density in the spin-down band, $n_{down} = \frac{n-g(E)\delta E}{2}$. Assuming that each electron has a magnetic moment $\mu_B$ we now have a magnetisation, $M = \mu_B(n_{up} - n_{down}) = \mu_B g(E)E_F$. The potential energy arising from the molecular field in such a situation is expressed in equation 2.12,

$$\Delta E_{P.E.} = -\frac{\mu_0 \lambda M^2}{2} = -\frac{\mu_0 \mu_B^2 \lambda}{2}(g(E_F)\delta E)^2 = -\frac{U}{2}(g(E_F)\delta E)^2, \tag{2.12}$$

where $U$ is a measure of the Coulomb energy ($U = \mu_0 \mu_B^2 \lambda$).

So, we can now consider the total change in energy, expressed in equation 2.13,

$$\Delta E = \Delta E_{P.E.} + \Delta E_{K.E.} = \frac{g(E_F)(\delta E)^2}{2}(1 - Ug(E_F)). \tag{2.13}$$

The result is that the spontaneous band-splitting is energetically favourable if $\delta E < 0$ which is true when $Ug(E_F) > 1$ (the Stoner criterion). The implications of this are that in order for the electron gas to spontaneously split the Coulomb effects must be strong (a large value of $\lambda$) and the density of states at the Fermi energy is large.

### 2.2.3 Magnetic domains

In the case of ferromagnetic ordering it would be expected that, due to nearest neighbours favouring a parallel alignment, the sample should always possess a net magnetisation - but this is not always the case. If a magnetic moment terminates at a surface state, it creates a demagnetisation field in the surrounding space (at a cost of magnetostatic energy). If instead of existing as a single domain the material is divided into several domains, ferromagnetically ordered locally, but arranged so that no magnetic moment terminates at a surface, the energy of the material can be

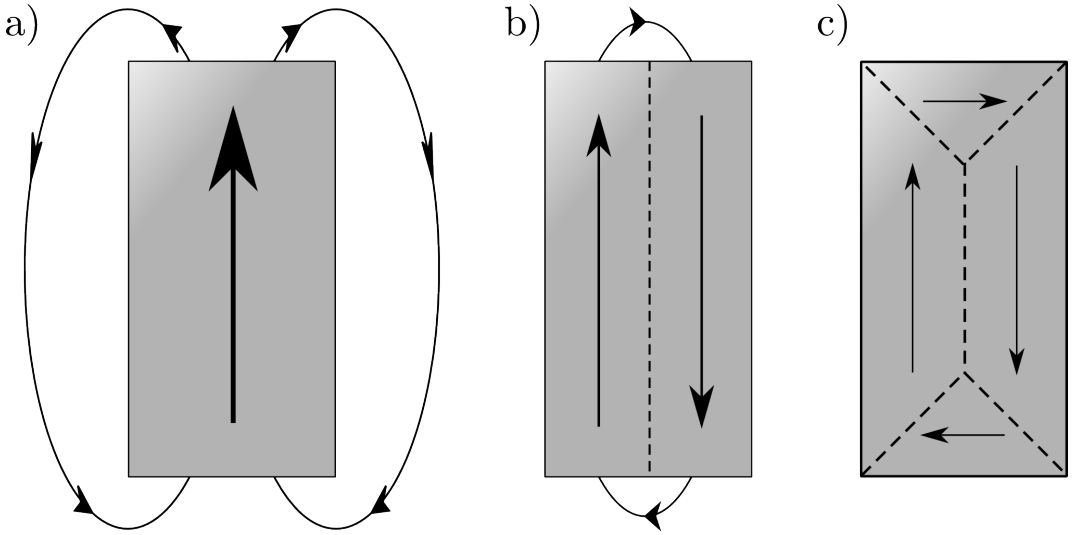


Figure 2.6: Schematic representation of the decrease in demagnetisation field (represented by the length of the line in free space) with the formation of domains. a) The magneto-static energy is maximised in the single domain case; b) magneto-static energy decreases with the formation of a single domain wall; c) the magneto-static energy is minimised in the multi domain case.

minimised.

Figure 2.6 illustrates the difference in demagnetisation field due to the formation of domains. However, the domain walls (the region between ferromagnetically ordered regions) have their own energy cost associated with overcoming the ferromagnetic exchange. It is the balance between the magneto-static and exchange energy costs that determines the domain structure of the ferromagnet.

### 2.2.4 Magnetic anisotropy

The magnetic exchange interactions are not the only factor that affect the preferred orientation of magnetic moments, or else ferromagnetic domains would simply rotate en-mass to an applied field. The underlying crystal structure also has an effect - giving rise to crystallographic axes along which the energy is either minimised (a magnetically easy axis) or maximised (a magnetically hard axis). This behaviour is described as the magneto-crystalline anisotropy, and alongside shape anisotropy (which can be ignored for spherical particles), is the dominant anisotropy for magnetic nanoparticles.

The simplest form of anisotropy is a uni-axial anisotropy, as described by

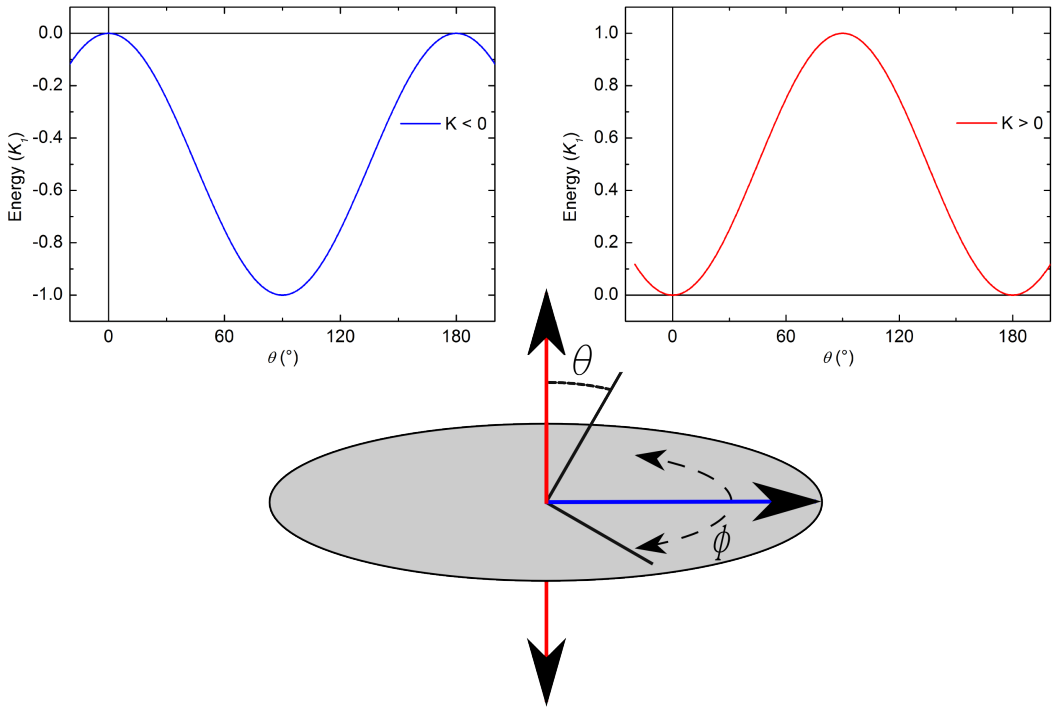


Figure 2.7: Schematic representation of the spatial orientations of the magnetically easy directions for the easy axis (red) and easy plane (blue) situation. The energy profiles describe the energy change with a canting away from the anisotropic axis, $\theta$, and are degenerate with rotation, $\phi$, about this axis.

equation 2.14,

$$E = K_1 \sin^2\theta + K_2 \sin^4\theta, \tag{2.14}$$

where $\theta$ is the angular displacement between the magnetic moment and the magnetic easy axis and $K_1$ and $K_2$ are the first two terms of the anisotropy. For the case of nanoparticles $K_1 >> K_2$, and so this simplifies to two magnetic cases; where $K_1 > 0$ and when $K_1 < 0$, giving rise to a magnetically easy axis and plane, respectively (demonstrated schematically in figure 2.7). In a uni-axial system the magnetic moments are energetically degenerate with rotation about the anisotropic axis, with a variation in energy as the moment cants away from this axis, expressed as the angle $\theta$.

### 2.2.5 Nano-ferromagnetism - the single domain

Bulk ferromagnetic materials split into multiple domains due to competition between the energy cost of the demagnetisation field created by terminating a magnetic moment at a surface state and the energy of a domain wall. Interestingly, the demagnetisation field scales with particle volume ($r^3$ scaling), while the domain wall cost scales with the cross sectional area of the material ($r^2$ scaling). The result of this is that when ferromagnetic samples are reduced to the nano-scale (by either top-down ball milling of bulk material or bottom-up synthesis) the energy cost of terminating a magnetic moment at the surface state decreases faster than the energy cost of the domain wall. The extreme case of this is observed when the particle diameter is of the order 10 nm and all of the magnetic moments within a single particle align ferromagnetically in a single domain.

When the particle is within the "single-domain" limit the direction of magnetisation (at $T = 0$ K) is purely based on the direction of applied field and the preferred magneto-crystalline orientation. If we revisit the earlier description of uniaxial magneto-crystalline anisotropy we can express the energy of the magnetic moment, $\mu$, as a result of the competing interactions with the applied magnetic field, $H$, and the crystallographic easy axis, $K$,

$$\frac{E}{V} = K \sin^2(\theta - \phi) - \mu_0 H M_S \cos\phi, \tag{2.15}$$

where $\theta$ is the angular displacement between the easy axis and applied field and $\phi$ is the angle between the magnetic moment and the direction of applied field. For each set of parameters, $H$, $M_S$, $K$ and $\theta$ we can construct an energy surface in the rotation of the magnetic moment, $\phi$, as shown in figure 2.8. The energy surface at $H = 0$ is comparable to the energy surface for a uniaxial material (with $K$ equivalent to $K_1$, and $\geq 0$) shown earlier in figure 2.7.

For a single particle we can predict the hysteretic magnetic behaviour by calculating the value of $\phi$ which results in an energy minimum for a given value of applied magnetic field, $H$, and repeating this for a range of $H$. Figure 2.9 a) shows the simulated magnetic behaviour for a range of $\theta$ values ($\theta = \frac{\pi}{10}$, $\frac{2\pi}{10}$, $\frac{3\pi}{10}$, $\frac{4\pi}{10}$, and $\frac{5\pi}{10}$), where $\frac{M}{M_S} = \cos\phi$. The "magnetic hardness", the resistance to a rearrangement of the magnetic moment, decreases as the angle between the easy axis and applied field increases - with a soft, reversible magnetisation when the two are perpendicular ($\theta = \frac{5\pi}{10}$).

In the case of a sample of identical nanoparticles the magnetically easy axes

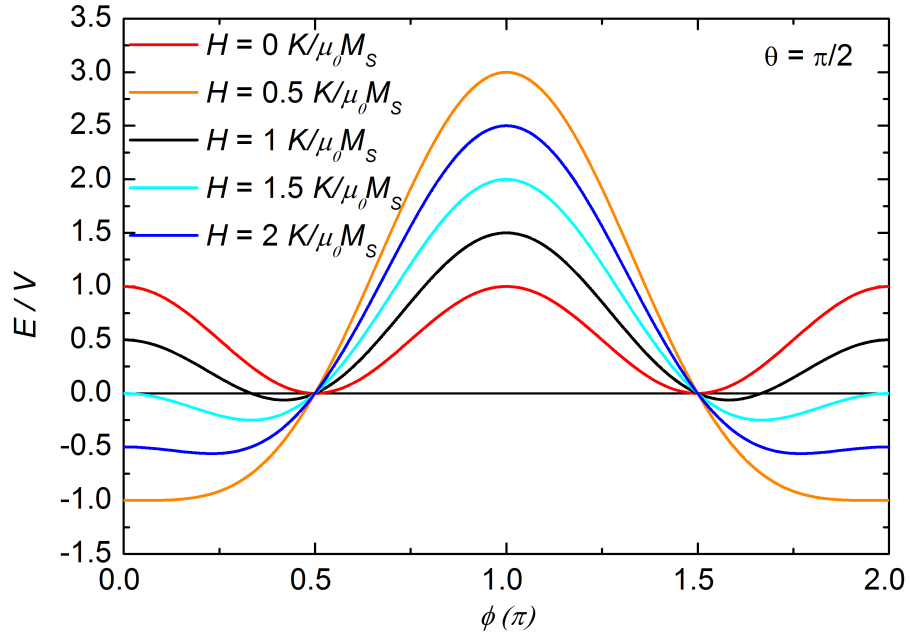


Figure 2.8: Energy profiles arising from the uniaxial anisotropy equation for a range of $\frac{K}{\mu_0 M_S}$ ratios with variation in the angle between the magnetic moment and the direction of applied field, $\phi$. These profiles all assume a 90° offset between the anisotropy axis and the direction of applied field, i.e. $\theta = \frac{\pi}{2}$.

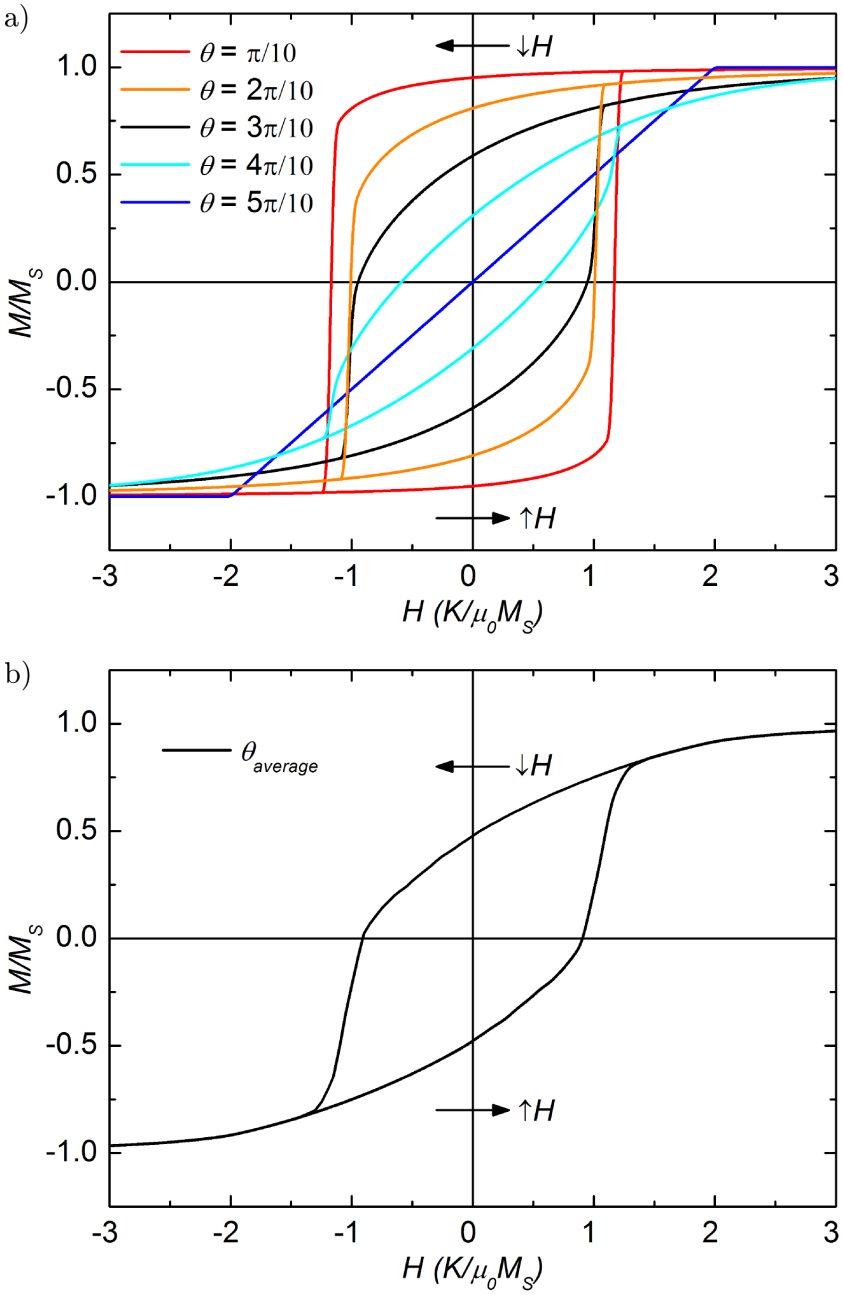


Figure 2.9: a) Simulated $M$ vs $H$ response for a single nanoparticle at $T = 0$ K with an angular offset between the anisotropic axis and the direction of applied field, $\theta$. As $\theta$ approaches 0, the hysteretic loops become magnetically "harder" with $\theta = \frac{\pi}{2}$ representing a reversible magnetisation. b) Simulated $M$ vs $H$ response for a polycrystalline average of randomly orientated in $\theta$ nanoparticles, where the weighting of each mono-$\theta$ simulation is proportional to $\cos\theta$.

will be randomly oriented with respect to each other, distributed evenly over space. Taking the summation over a range of $\theta$, weighting by the probability of the easy axis occurring at that $\theta$ and normalising we can predict the hysteretic behaviour for a polycrystalline average of particles, demonstrated in figure 2.9 b), with the applied field, $H$, relative to the materials magnetic saturation $M_S$ and anisotropy constant, $K$. The result of this is a universal magnetic behaviour for a random distribution of uniaxial magnetic particles, resulting in a predicted remanent magnetisation, $M_R \approx \frac{M_S}{2}$ and a coercive field, $H_C = \frac{K}{\mu_0 M_S}$.

This behaviour assumes $T = 0$ K, and that the magnetic moment remains in a local energy minimum until the energy space has been distorted by the increasing applied magnetic field to such an extent the minimum no longer exists. It is this assumption of a trapped energy minimum that means this prediction only holds on the return from saturation at low $T$. It is this binding to a local minimum that earns the system its nomenclature, the "blocked" state.

### 2.2.6 Superparamagnetism

The energy surfaces from which the Stoner-Wohlfarth model arises demonstrate that, at low $H$, there are two minima, with equivalent energy but split by a rotation of the magnetic moment in $\phi$ by $\pi$. These two minima are the situation when the moment is oriented parallel or anti-parallel to the magnetically easy axis, off axis from the applied field vector by $\theta$. When the applied field is small these minima are split by two, symmetrical, energy barriers directly proportional to the particle volume, $V$, and the anisotropy constant, $K$, i.e. energy barrier to magnetic reversal$_{\mathrm{H}\approx 0} = KV$. As the thermal energy of the system ($k_B T$) increases, the rate of magnetic reversal increases, with the time spent in the minima decreasing. Eventually, all the particle "super" magnetic moments can be approximated as free paramagnetic moments, unbound from the particle crystallography and the magneto-crystalline anisotropy. We can apply the same mathematical approach to the "super" paramagnetic species as to the atomic paramagnet, see section 2.2, and hence describe the magnetisation of the sample as a function of the applied field via a Langevin function,

$$\frac{M}{M_S} = \coth\left(\frac{\mu_{particle} B}{k_B T}\right) - \left(\frac{\mu_{particle} B}{k_B T}\right)^{-1}, \tag{2.16}$$

where $M$ is the magnetisation along the direction of the effective applied field, $B$, relative to the saturated magnetisation, $M_S$, for a "super" paramagnetic moment, $\mu_{particle}$. So, at a volume dependent temperature the magnetic response to an applied

field will convert from a hysteretic, blocked response given by the Stoner-Wohlfarth model to a reversible, super paramagnetic behaviour. This process is referred to as the particle "unblocking" and the temperature at which this crossover behaviour occurs is the "blocking" temperature.

### 2.2.7 Neél relaxation

When discussing the concept of super-paramagnetism we discussed the relationship between the energy barrier to magnetic reversal, $KV$, and the thermal energy of the system, $k_BT$. The time scale of this reversal has been expressed previously as the Neél relaxation (or Neél-Arrhenius after its similarity to the Arrhenius equation of chemical reaction rates),

$$\tau_N = \tau_0 \exp\left(\frac{KV}{k_BT}\right), \tag{2.17}$$

where $\tau_N$ is the Neél relaxation time (the average time between successful moment reversals) and $\frac{1}{\tau_0}$ is the attempt frequency. If the value of $\tau_N$ is less than the time window of the experiment then the magnetic reversal is considered rapid enough to observe the super-paramagnetic case, while if $\tau_N$ is longer we observe the blocked, Stoner-Wohlfarth behaviour. When investigating this thermal behaviour the Neél relaxation is generally simplified,[62] assuming a critical value of $\tau_N = 25$ s and an order of magnitude of $\tau_0 = 10^{-9}$ s (resulting in $\ln\left(\frac{25}{10^{-9}}\right) \approx 25$), giving a linear relationship between the particle volume, $V$, and the blocking temperature $T_B$,

$$KV \approx 25 k_B T_B. \tag{2.18}$$

## 2.3 Experimental approaches

Nanoparticle magnetism for a perfectly mono-disperse sample can be described theoretically using the Stoner-Wohlfarth model at low $T$, the super-paramagnetic model at high $T$ and the Neél relaxation to define the boundary between the two states. However, catalytic materials will possess a degree of poly-dispersity which we must account for when analysing the data. In this section we outline the reasoning, justification and assumptions made for the two analytical approaches applied to the magnetisation data in the rest of this thesis.

### 2.3.1 Blocking temperature distributions

We now have a description of the magnetisation above and below the blocking temperature, $T_B$, as well as a way of relating the value of $T_B$ to the volume of the particle. Importantly, the high $T$, super-paramagnetic response is reversible, and as such has no dependence on the applied magnetic field the sample is cooled in, while the low $T$, blocked magnetisation is hysteretic, and hence depends on the field applied during cooling. It is this behaviour that leads to a difference in magnetisation between zero-field cooled ($M_{ZFC}$) and field cooled ($M_{FC}$) measurements. In the field cooled case, the magnetic moments are biased to one of the two minima discussed earlier (see figure 2.8) - with preference for the minimum closer in $\phi$ to the magnetic saturation orientation ($\phi = 0$ for a positive $H$ saturation cf. $\phi = \pi$ for a negative $H$ saturation) and hence the $M_{FC}$ can be considered to follow one of the hysteretic loops of the Stoner-Wohlfarth model. For the zero-field cooled case, the magnetic moments are evenly distributed between the two minima, and $M_{ZFC}$ has a magnetic behaviour which follows a superposition of the two sides of the blocked response.

The ratio of blocked response to super-paramagnetic response is then dependent on the proportion of the particle size distribution, $P(V)$, on either side of the critical volume, $V_{crit}$ (the particle volume at the boundary between reversible and hysteretic behaviour at the system temperature). Assuming that the magnetisation at low fields is linear we can express the $M_{FC}$ and $M_{ZFC}$ as,

$$M_{FC} = \int_{V_{Crit}}^{\infty} P(V)\,(M_R + \chi_{FC}H)\,dV + \int_{0}^{V_{Crit}} P(V)\,(\chi_{S.P.}H)\,dV, \tag{2.19}$$

$$M_{ZFC} = \int_{V_{Crit}}^{\infty} P(V)\,(\chi_{ZFC}H)\,dV + \int_{0}^{V_{Crit}} P(V)\,(\chi_{S.P.}H)\,dV, \tag{2.20}$$

where $\chi_{FC}$ and $\chi_{ZFC}$ are the low field susceptibility for the field cooled and zero-field cooled cases respectively, $M_R$ is the remanent magnetisation and $\chi_{S.P.}$ is the super-paramagnetic susceptibility at low $H$. It should be clear that the super paramagnetic contribution is identical in the two cases, and so we can take $\Delta M = M_{ZFC} - M_{FC}$ in order to remove it,

$$\Delta M = M_{ZFC} - M_{FC} = \int_{V_{Crit}}^{\infty} P(V)\left(\left(\chi_{ZFC} - \chi_{FC}\right)H - M_R\right)dV. \tag{2.21}$$

The Stoner-Wohlfarth model assumes that the magnetisation is independent of the temperature and that the magnetic moment remains within the local minima, and hence the only $T$ dependent term is the limit of the integral, $V_{Crit}$. If we take the thermal differential of $\Delta M$, i.e. the differential of the difference in $M$ between the FC and ZFC scans as a function of temperature, using this assumption we can reduce $\left(\chi_{ZFC} - \chi_{FC}\right)H - M_R$ to a constant, $\beta$, which can then be integrated (using the general form of Leibniz's rule,

$$\frac{d}{dx}\int_{a(x)}^{b(x)} f(x,t)dt = f(x,b(x))b'(x) - f(x,a(x))a'(x) + \int_{a(x)}^{b(x)} f_x(x,t)dt, \tag{2.22}$$

where $b(T) = \infty$, $a(T) = \frac{25k_BT}{K}$, $f_x(x,t)$ is the partial derivative of $f(x,t)$ with respect to $x$, and $f(T,V) = \beta P(V)$. The result of the differential is

$$\frac{d\Delta M}{dT} = \frac{25k_B}{K}\beta P(V_{Crit}), \tag{2.23}$$

where $\frac{25k_B}{K}\beta$ is treated as a constant. The result of this is that, upon normalisation, $\frac{d\Delta M}{dT} = PV_{Crit}$, i.e. the thermal differential, maps the distribution of critical volumes or blocking temperatures (depending on whether or not the conversion $\frac{25k_B}{K}$ has been applied).

### 2.3.2 Super-paramagnetism of polydisperse sample

In contrast to atomic paramagnets, super-paramagnetic materials can have a broad distribution of effective magnetic moments. As a result, the Langevin function for the material takes the form,

$$\frac{M}{M_S} = \int_0^{\infty} P(x)\left(\coth\left(\frac{xB}{k_BT}\right) - \left(\frac{xB}{k_BT}\right)^{-1}\right)dx, \tag{2.24}$$

where $x$ is the size of the super paramagnetic moment and $P(x)$ is the associated probability distribution function (PDF). This distribution is generally assumed to be either a normal (Gaussian) distribution,

$$P(x) = \frac{1}{\sigma\sqrt{2\pi}} \exp^{-\frac{(x-\mu)^2}{2\sigma^2}}, \tag{2.25}$$

where $\mu$ and $\sigma$ are the mean and standard deviation, respectively, of the variable, $x$, or a log-normal distribution,

$$P(x) = \frac{1}{x\sigma\sqrt{2\pi}} \exp^{-\frac{(\ln x-\mu)^2}{2\sigma^2}}, \tag{2.26}$$

where $\mu$ and $\sigma$ are the mean and standard deviation, respectively, of the natural logarithm of the variable, $x$. The first fact to note is that in both cases as $x \to \infty$, $P(x) \to 0$ resulting in a convergent integral for all practical cases which can be analysed. However, it can be computationally expensive to integrate over the full range of particle sizes. Here we will explore the effect of increasing polydispersity on the magnetic behaviour to determine if simpler, non-integral analytical equations can be used as an approximation during the later experimental studies.

To investigate the effect of a normal distribution of magnetic moments on the measured behaviour, three distributions were constructed with an average size, $\mu = 100$, and standard deviations, $\sigma = 5$, 15, and 30 respectively (shown in figure 2.10 a)). For each distribution the equivalent magnetisations were calculated (as shown in figure 2.11) assuming each particle follows the Langevin magnetisation, taking the integral within the central 98% of the distribution ($\mu \pm 2.32\sigma$), system temperature, $T = 10$ K, and magnetic saturation, $M_S = 1$. The resulting magnetisations were fit with a non-disperse Langevin function, with two free parameters ($\mu$ and $M_S$), with the resulting fits represented as the lines on figure 2.11 and the parameters of best fit summarised in table 2.1. The single Langevin function appears to closely reflect the simulated magnetisation from the three samples, with values of $M_S$ in agreement with the simulated value. The predicted value of $\mu$ from this method do slightly underestimate the simulated value, with an increasing disagreement and parameter error as $\sigma$ increases. The source of this disagreement appears to be the growth of $H$ required to obtain magnetic saturation, however, the samples we will investigate are unlikely to have a polydispersity as large as $\sigma = 30\%\mu$ the error introduced at larger polydispersity can be ignored.

The same methodology has been repeated using the log normal function, constructing three distributions with associated parameters $\mu = \ln(100)$ and $\sigma = \ln(5)$, $\ln(15)$, and $\ln(30)$, respectively (shown in figure 2.10 b)).

The three simulated magnetic behaviours, shown in figures 2.12, were cal-

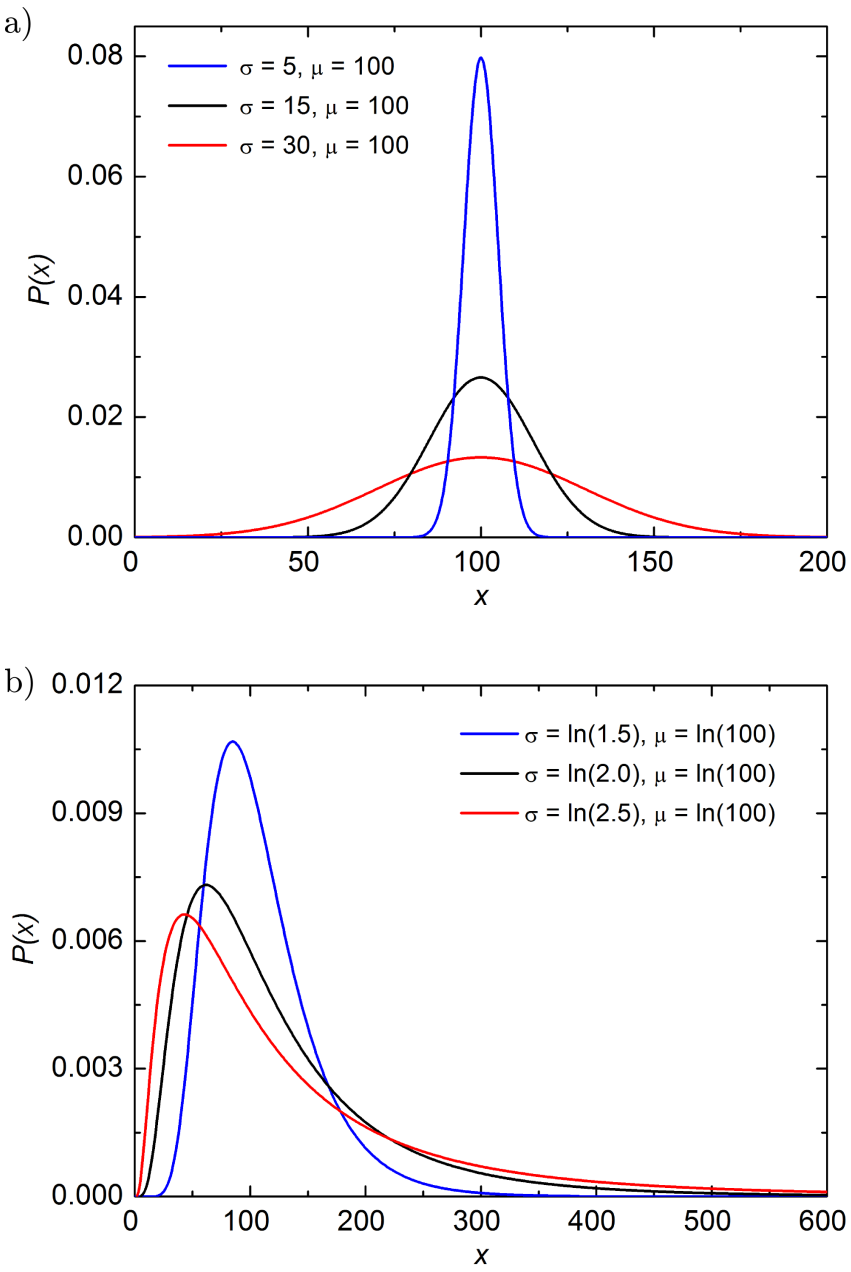


Figure 2.10: a) Probability distribution functions (P(x)) for the 3 constructed normal distributions used in the Langevin simulations. b) PDFs for the 3 constructed log-normal distributions used in the Langevin simulations.

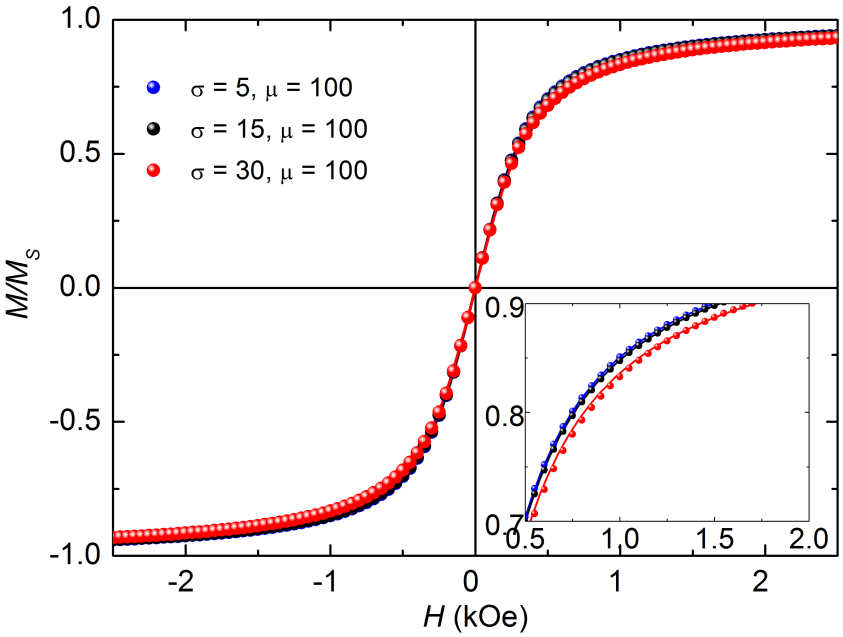


Figure 2.11: Simulated magnetic response for the three normal P.D.F. shown in figure 2.10 a), assuming the magnetic species follow a Langevin magnetisation, $T = 10$ K and normalised with respect to $M_S$. The magnetisations have been fit with a single Langevin function model (shown as the solid lines) giving a close reproduction of the data. The best fit parameters are given in table 2.1

| Sample | $\mu$ | $M_S$ |
|---|---|---|
| $\sigma = 5$ | 99.9(2) | 1.00(1) |
| $\sigma = 15$ | 98.9(4) | 1.00(1) |
| $\sigma = 30$ | 96(1) | 0.99(1) |

Table 2.1: Best fit parameters for the single Langevin model fit to the simulated normal P.D.F. data sets shown in figure 2.11.

culated assuming each particle follows the Langevin response, taking the integral within the central 98% of the distribution ($\mu\sigma^{-2.32}$ to $\mu\sigma^{2.32}$), system temperature, $T = 10$ K, and magnetic saturation, $M_S = 1$. The resulting magnetisation were fit with a non-disperse Langevin function as previously described and the resultant fits represented as the lines on figure 2.12 a). Unlike for the previous normal distribution simulations the single Langevin approach fails to reproduce the simulated magnetic behaviour, suggesting a more complex model is required.

The Single Langevin model appears to fit the normal PDF simulation well, but not the log-normal PDF simulation. As the normal distribution is symmetrical, the terms with $x > \mu$ are balanced by the equivalent term with $x < \mu$ leading to an average behaviour consistent with a mono-disperse sample. The log-normal distribution, however, does not possess this symmetry - and hence the Single Langevin model is insufficient to reflect the behaviour. A second model is suggested, comprising a super-position of two Langevin behaviours,

$$M = \sum_{i=1}^{2} M_{Si} \left[ \coth\left(\frac{x_i H}{k_B T}\right) - \left(\frac{x_i H}{k_B T}\right)^{-1} \right]. \tag{2.27}$$

where $M$ is the magnetisation, $x_i$ is the effective magnetic moment of the individual Langevin term with associated magnetic saturation, $M_{Si}$.

Figure 2.12 b) shows the result from fitting the log normal simulations with a pair of Langevin functions, with the resulting fits shown as the solid lines. The addition of a second Langevin function clearly improves the quality of the fit, with a close reproduction of the simulated magnetic behaviour. The parameters of this fit are given in table 2.2.

| Sample | $x_1$ | $x_2$ | $M_{S\ 1}$ | $M_{S\ 2}$ |
|---|---|---|---|---|
| $\sigma = \ln(1.5)$ | 68.4(4) | 142.9(7) | 0.475(6) | 0.507(6) |
| $\sigma = \ln(2.0)$ | 54.2(6) | 180(2) | 0.471(8) | 0.507(8) |
| $\sigma = \ln(2.5)$ | 47.2(8) | 213(4) | 0.471(9) | 0.500(9) |

Table 2.2: Best fit parameters for the dual Langevin model to the log-normal data sets shown in figure 2.12.

The values found for fitting a log normal distribution with the dual Langevin function is consistent in all three cases with an equal contribution from both functions (near 50:50 ratio) with the difference between values of $\mu$ increasing with $\sigma$. Using the cumulative distribution (C.D.) of each log normal distribution these values of $x$ can be converted to intensity on the distribution (as done in table 2.3). The

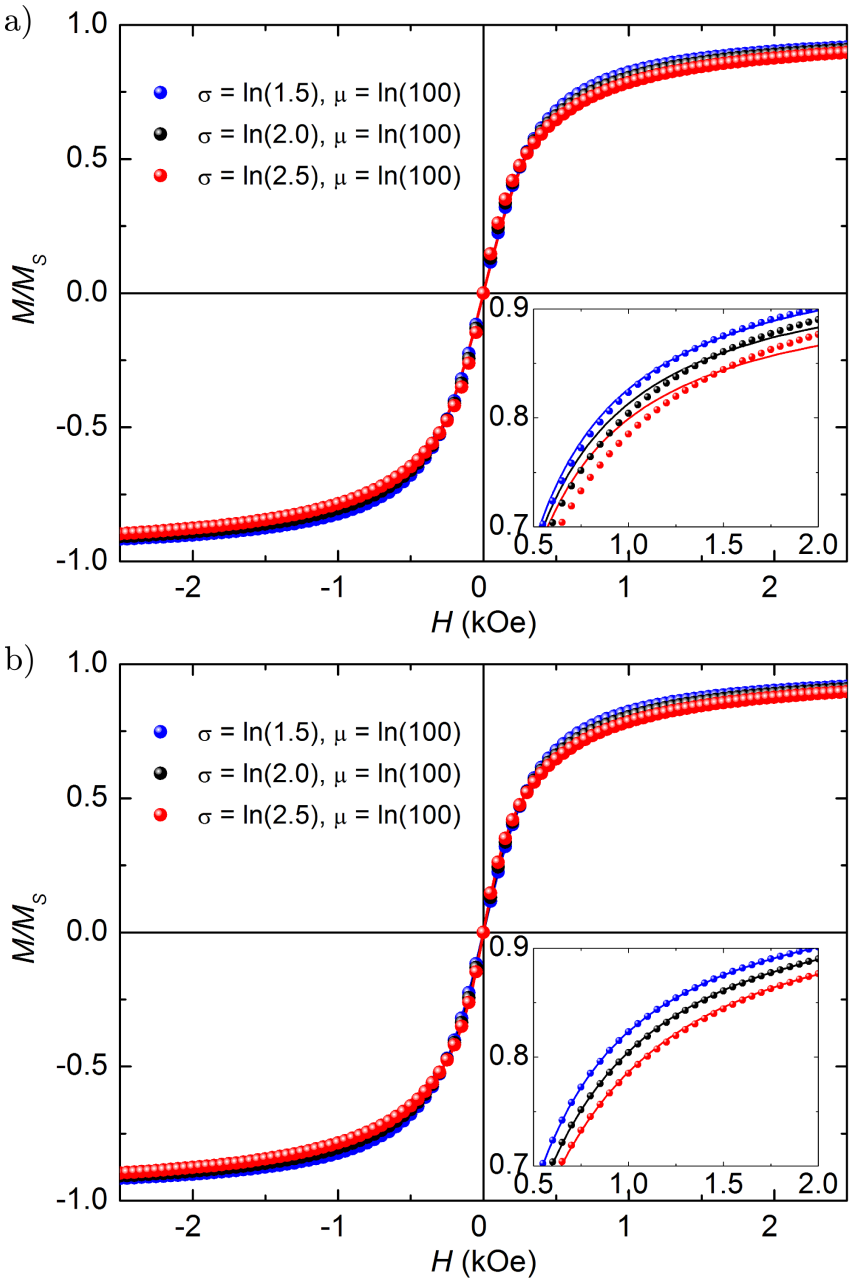


Figure 2.12: Simulated magnetic response for the three log-normal P.D.F. shown in figure 2.10 b), assuming the magnetic species follow a Langevin magnetisation, $T = 10$ K and normalised with respect to $M_S$. The magnetisations have been fit with a single Langevin function model (a) and with a superposition of two Langevin functions (b). The dual Langevin model gives the superior fit in all three cases. The best fit parameters for the dual Lagnevin fits (b) are given in table 2.2

two values of $x$ appear to be clustered around $\approx 20\%$ and $80\%$ with decreasing $\sigma$ values being further from the centre of the distribution. Averaging the three values it appears that $x_1 = 19.0(3)$ % and $x_2 = 80.3(3)$ %.

| Sample | $x_1$ | CDF % | $x_2$ | CDF % |
|---|---|---|---|---|
| $\sigma = \ln(1.5)$ | 68.4(4) | 17.5(4) | 142.9(7) | 81.1(3) |
| $\sigma = \ln(2.0)$ | 54.2(6) | 18.8(4) | 180(2) | 80.2(4) |
| $\sigma = \ln(2.5)$ | 47.2(8) | 20.6(5) | 213(4) | 79.5(6) |

Table 2.3: Summary of the values of $x$ found from the dual Langevin fit to the simulated log-normal P.D.F. magnetisations, alongside the % position on the associated cumulative distribution function (CDF).

These predictions are based on perfect simulations, and as a result have likely underestimated the errors to be expected from experimental results. Hence, when these models are applied later in this thesis we will generalise the results to give values of $x$ at $\approx 20$ and $80$ % of the associated log normal cumulative distribution.

# Chapter 3

# Experimental details

## 3.1 Characterisation techniques

### 3.1.1 SQUID magnetometry

Magnetisation data were taken using a Quantum Design (QD) Magnetic Property Measurement System (MPMS) utilising a Superconducting QUantum Interference Device (SQUID) to function as a highly sensitive current-voltage converter.[105] The magnetometer comprises three key components for measuring the magnetisation - a superconducting magnet to generate large magnetic fields, a superconducting detection coil (wound in a second-order gradiometer configuration), and the rf-SQUID (comprising a Josephson junction in a superconducting ring).[106]

Measurement of the magnetisation requires the material to be mounted in a non-magnetic sample holder and inserted between the detection coils and moved through the gradiometer in the direction along which the magnetisation is to be measured (in this case along the direction of applied magnetic field). As the sample is moved the magnetic flux passing through the gradiometer changes, inducing a current within the superconducting wire via electromagnetic induction. This superconducting wire leads to the SQUID, which has been configured to produce an output voltage strictly proportional to the current, outputting the change in magnetic flux measured by the pick up coils as a function of sample position. The geometry of the pick up coils and SQUID are shown in figure 3.1.

The voltage-position response produced by attenuating the sample is then fit by an ideal dipole response given in equation 3.1,

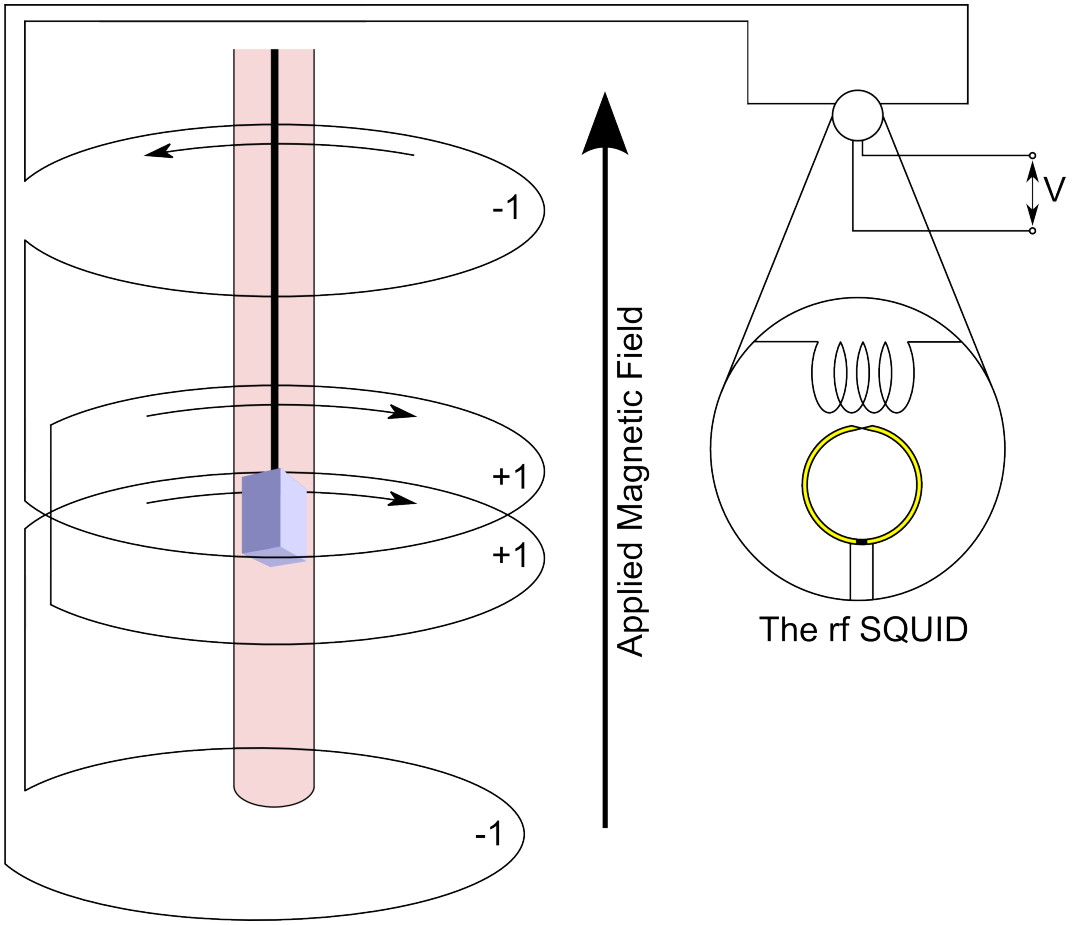


Figure 3.1: Schematic representation of the QD MPMS SQUID electronics, representing the sample space (pink), surrounded by the detection coils which feed into the rf-SQUID electronics.

$$f(Z) = \alpha + \beta Z + \gamma(2[R^2 + (Z+\delta)^2]^{-\frac{3}{2}} - [R^2 + (\Omega + Z + \delta)^2]^{-\frac{3}{2}} - [R^2 + (-\Omega + Z + \delta)^2]^{-\frac{3}{2}}), \quad (3.1)$$

in which $Z$ is the vertical sample position (centred at $Z = 2$ cm), $R$ and $\Omega$ are constants representing the longitudinal radius (0.97 cm) and the longitudinal coil separation (1.519 cm), respectively, and the free parameters are $\alpha$ (a constant voltage offset), $\beta$ (a linear background), $\delta$ (a vertical sample offset) and $\gamma$ (the magnitude of the dipole moment).

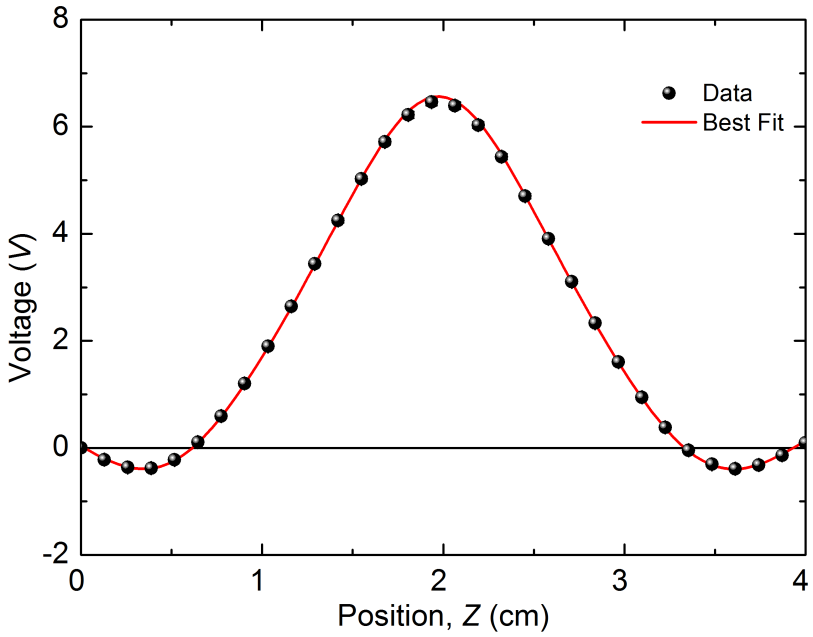


Figure 3.2: Typical example of a voltage-position response for sample, with the associated fit to equation 3.1.

The QD MPMS SQUID is calibrated against a sample of Pd of known mass and magnetic susceptibility allowing for the magnitude of the voltage dipole to be converted to a magnetic dipole expressed in electromagnetic units (emu). A typical voltage-position response is shown in figure 3.2 alongside a fit to equation 3.1. The best fit parameters are listed in table 3.1.

The QD MPMS SQUID system used in the studies detailed is limited to a maximum applied magnetic field, $H_{Max}$ = 50 kOe and a temperature range, 2 to 400 K. A temperature window of 5 to 300 K has been used for most $M$ vs $T$ studies

| Parameter | Value | Units |
|---|---|---|
| $\alpha$ | 1.726(8) | V |
| $\beta$ | $-1(2) \times 10^{-3}$ | V cm$^{-1}$ |
| $\gamma$ | 2.62(1) | V |
| $\delta$ | -1.97(1) | cm |

Table 3.1: Best fit parameters for the dipole response fit to the data in figure 3.2.

as it is impractical to carry out reproducible $T$ sweeps through the boiling point of the cryogen ($^4$He, $T_{B.P.} \approx 4.2$ K).[107]

### 3.1.2 Diffraction

The magnetic properties of a material - both in bulk and nanostructures - are dependent on structural parameters such as the lattice parameter and crystal phase.[108] Diffraction (be it of x-rays, neutrons, or electrons) is a popular technique for the characterisation of long-range ordered structures - with various techniques developed to be sensitive to both atomic and magnetic order.[109;110] The key difference between the three prevalent forms of diffraction is the scattering mechanism, and as such the elements that will dominate the diffraction pattern.

In the case of x-ray diffraction (XRD) it is the interaction between the incoming x-ray and the materials electrons that causes the x-ray to "scatter" and as such heavier elements have a higher probability to cause a scattering event. This higher probability means a higher sensitivity to heavier elements. In the case of elastic scattering (in which no energy transfer occurs between the incident beam and the scattering medium) each scattered x-ray has the same wavelength and amplitude. However, when x-rays scatter from different atomic planes this introduces a difference in the length traveled by the x-ray causing a shift in the relative phase of the x-ray. It is only when this difference in path length is a multiple of the wavelength of the x-rays that the x-rays remain in phase, creating detectable Bragg peaks.[111]

The relationship between the incident beam angle ($\theta$), wavelength ($\lambda$), and inter atomic planar spacing ($d$) is given by Bragg's Law,

$$\lambda = 2d \sin\theta, \tag{3.2}$$

The relationship between atom position and path-length difference is highlighted in figure 3.3 which describes the real space diffraction of an incident beam.

In the studies presented within this thesis, the XRD patterns have been taken using a lab source, with the incident beam comprising both Cu K$\alpha_1$ and K$\alpha_2$ wavelengths i.e. the wavelength of the light emitted during the decay of an electron into the 1s level from the $2p_{\frac{3}{2}}$ and $2p_{\frac{1}{2}}$ levels, respectively. The presence of both wavelengths means that data analysis will need to take both scattering wavelengths into account.

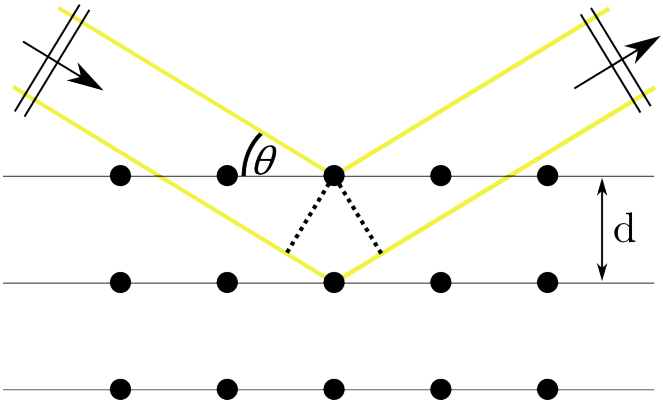


Figure 3.3: Real space representation of the scattering of radiation from a periodic array. The path length difference between the first and second scattering needs to be an integer multiple of the radiation wavelength to create constructive interference.

### Scherrer analysis

Aside from being able to measure variations in the crystallography of nano-particles, diffraction experiments are also useful for analysing the average particle size for a system of nanoparticles via the Scherrer equation,[112]

$$\tau = \frac{\kappa\lambda}{B\cos\theta}, \tag{3.3}$$

in which $\tau$ is the particle size, $\lambda$ is the wavelength of the X-rays, $\theta$ is the peak position in radians, $B$ is the full width half maximum (FWHM) of the peak (in radians) and $\kappa$ is a shape constant generally in the range 0.8 - 1.

The Scherrer equation is based on the observed broadening of the XRD peaks as crystallite size is decreased and can be derived from Bragg's Law. For a particle of given thickness, $t$, and planar spacing, $d$, there will be an integer number of planes, $m$, such that $d = t/m$. Substituting this into Bragg's law and taking the differential assuming that $\lambda$ is a constant we can show equation 3.4,

$$0 = 2\Delta t \sin\theta + 2t\cos\theta\Delta\theta, \tag{3.4}$$

in which $\Delta t$ is the smallest available change in $t$ i.e. $d$, and $\Delta\theta$ is the uncertainty in $\theta$ i.e. the line broadening.

A simple rearrangement of equation 3.4 gives the magnitude of the broadening in $\theta$,

$$|\Delta\theta| = \frac{d \sin\theta}{t \cos\theta}, \tag{3.5}$$

showing the inverse relationship between line broadening, $\Delta\theta$ and particle thickness, $t$. It is a trivial step[113] to use Bragg's law to show that $d \sin\theta = \lambda/2$ which on substitution gives the Scherrer relationship without the shape constant, $\kappa$. This final proportionality constant, $\kappa$, arises as the derivation assumes the particle thickness relative to the atomic planes are constant, as opposed to the gradual decrease cause by a spherical morphology.

Analysis of particle size via the Scherrer equation is popular due to the low detection resolution needed to probe small particle sizes and the relatively simple data analysis required. However, it should be remembered that the Scherrer analysis values should be treated as a lower boundary to the particle size as the analysis assumes all material based line broadening arises from the particle size, ignoring broadening arising from non-uniform strain within the crystal lattice or concentration gradients.

### 3.1.3 Temperature programmed reduction (TPR)

Heterogeneous catalysts are usually exposed to relatively harsh chemical environments, both during synthesis and use, leading to the formation of metal oxides, nitrides and carbides.[114] The quantity of the catalytic material that exists as the reduced species is a key variable for the catalytic activity and magnetic behaviour, and can be followed via temperature programmed reduction (TPR).[115]

During a TPR experiment the sample is exposed to a constant flow of a high-purity $H_2$/Ar gas mixture while the sample is gradually heated. Each oxidised species has an associated energy required for the reduction, following a typical reaction scheme,

$$NiO + H_2 \rightarrow Ni + H_2O \tag{3.6}$$

and hence a temperature at which the given reduction will occur. The TPR experiment follows the rate of these processes as a function of sample temperature by measuring the composition of the post sample gas flow utilising a thermal conductivity detector (TCD).

The TCD is sensitive to changes in the gas phase, using a Wheatstone bridge to follow the uptake in $H_2$. The pre and post sample gas flows pass over a pair of resistive filaments acting as Pirani gauges, where the filament loses heat to the flow

gas at a rate proportional to the pressure. This reduction in filament temperature leads to an increase in resistance, and hence a variation in the output signal across the Wheatstone bridge, quantifying the gas uptake.

The TPR equipment follows the kinetics of the gas phase reaction as a function of temperature. In the context of this work, the TPR results are primarily used to determine the degree of reduction of the catalysts, measuring the uptake of $H_2$ gas at the NiO/Ni reduction[116] (occurring at $T \approx 640$ K) in comparison to the known loading of catalyst.

### 3.1.4 Transmission electron microscopy (TEM)

Due to the wavelength of visible light (390 - 700 nm) traditional microscopes have a diffraction limit of $\approx 0.2$ $\mu$m. In order to image smaller objects - such as nanoparticles, a smaller wavelength is required. This has been achieved by using electrons, in which the wavelength is equal to $\frac{h}{p}$ where $h$ is Planck's constant and $p$ is the relativistic momentum of the electron, with high kinetic energy. For the transmission electron microscopy (TEM) presented in this thesis the electrons have an acceleration energy of $\approx 200$ keV, giving them a wavelength of 2.5 pm, lowering the diffraction limit to well below the smallest sample we hope to image.[117]

The TEM uses a field emission gun as the electron source, giving a higher flux of focused electrons than can be achieved with a traditional $LaB_6$ filament. The electrons are then focussed onto the sample area. The TEM sample has be to be thin ($\leq 200$ nm) in order for enough electrons to be transmitted to produce an image, often requiring time consuming sample preparation procedures for bulk materials in which the sample thickness needs to be gradually reduced. For colloidal nanoparticles, this procedure is simplified as a dilute solution can be evaporated onto a TEM grid, depositing the particles ready for imaging. The TEM images shown in this thesis have used a TEM sample holder comprising a Cu grid supporting a lacey carbon support on which the nanoparticle rest.

The TEM operates in two modes, imaging and diffraction, depending on the focusing optics used after the sample space. When the incident electron beam strikes the sample, the beam can either be transmitted or scattered (caused by the incident electron interacting with the samples electron cloud, leading to a higher contrast for heavier elements). The post-sample electron beams can then be focused onto the detector via the objective and intermediate lenses. The objective lense re-focuses the beams after being scattered by the sample, creating an initial back focal plane (the

point at which beams with the same scattering angle meet) and a mirrored image. The intermediate lense acts on these focused beams, producing a second back focal plane and a non-mirrored image, either of which can be projected onto the CCD detector by moving the lenses position. In diffraction mode the back focal plane is selected, focusing electron beams with the same scattering angle at the sample onto the same position, generating a diffraction pattern of bright spots, arranged around the transmitted beam. In imaging mode, a single scatterign angle can be selected, by introducing an apparture, that can then be projected onto the detector as an image. When producing images in this way we can either work in bright-field mode, where the image is formed from the transmitted beam and the scattering bodies appear as black objects on a white background, or dark-field mode, using one of the scattered electron beams and inverting the contrast.

### 3.1.5 Gas adsorption

Gas absorption isotherms are used to determine the surface area of catalytic species through the uptake of a reactive gas following the reduction of the sample in a $H_2$ environment.[118] Following the reduction the sample space is dosed with a known volume of reactive gas at a set partial pressure and the loss in feed gas measured via a TCD system, as described in 3.1.3, to quantify the extent of absorption. This process is repeated at a range of increasing pressures until the sample is saturated, with the cumulative gas absorption as a function of partial pressure producing the gas isotherm. This first isotherm reflects the total gas absorption of the sample.

Following the first isotherm the sample space is placed under vacuum and the gas doping process repeated. The second isotherm will measure a reduction in absorption compared to the first, as the vacuum step only removes the weakly absorbed gas, and this second dosing is a quantification of the reversible gas absorption. Hence the difference between the first and second isotherm reflects the strong absorption isotherm, reflecting purely the irreversible processes.

When analysing the gas absorption data, the structure of the isotherm can be used to follow the processes by which the absorption occurs, however, for determination of the crystallite size it is purely the cumulative gas uptake when the material is saturated that is of importance. Two values can be deduced from the saturated isotherms, the total absorption ($Abs_{Total}$) and the strong absorption ($Abs_{Strong}$). It is generally assumed that $Abs_{Strong}$ reflects the chemisorption processes while $Abs_{Total}$ reflects both chemi- and physisorption processes.[1]

Gas absorption is related to particle size via the dispersion of the catalyst (the ratio between the number of atoms per particle found at the surface, $N_S$, and total, $N_T$). For a spherical particle, the dispersion can be expressed as the atomic ratio of these two,

$$\frac{N_S}{N_T} = \frac{S_{Particle}}{S_{atom}} \left( \frac{V_{Particle} \rho N_A}{A_r} \right)^{-1} = \frac{A_r}{\rho N_A S_{atom}} \frac{6}{r}, \tag{3.7}$$

where $S_{Particle}$ and $V_{Particle}$ are the surface area and volume of a particle, $S_{atom}$ is the increase in surface area per particle, $\rho$ is the material density, $A_r$ is the atomic mass of the material, $N_A$ is Avogadro's number and $r$ is the particle radius.

The value for the dispersion can then be scaled with the number of particles, and related to the sample surface area,

$$\frac{N_S}{N_T} = \frac{S_{Total}}{S_{atom} N_T}, \tag{3.8}$$

where $S_{Total}$ is the measured gas absorption, assuming a single monolayer of gas absorption onto a non-fractal surface. Using these two equations for the dispersion we can deduce an equation for the average particle radius, r,

$$r = \frac{6 A_r}{\rho N_A S_{atom}} \left( \frac{S_{Total}}{S_{atom} N_T} \right)^{-1} = \frac{6 A_r N_T}{\rho N_A S_{Total}}. \tag{3.9}$$

Using this equation alongside the saturated gas absorption values from the isotherms the average particle size can be calculated, however, as has been stated earlier we have to assume a single monolayer absorption onto a smooth, spherical structure. In practice gas absorption isotherms will generally give an overestimate of the average particle size, and has been shown to overestimate with respect to XRD analysis.[24]

### 3.1.6 Small Angle Neutron Scattering

Small Angle Neutron Scattering (SANS) is a diffraction technique tailored to probing ordered system with a relatively large $d$ spacing - in the range 10 to 1000 Å. The use of neutrons instead of x-rays as the scattered species allows for a different scattering mechanism (scattering from the nuclei via the strong nuclear force cf. from the electron density) imparting a different resolution mechanism and a sensitivity to lighter elements.[119] A key property of the neutron, however, is that each particle possess a magnetic moment; which may couple to the magnetisation of the sample and probe the magnetic structure in reciprocal space.

When a neutron interacts with matter two possible processes occur, absorption or scattering, and for each process we can define a neutron cross section for each process (akin to the probability of occurrence).[120] In a neutron scattering experiment we measure the quantity of neutrons that scatter as a function of $\theta$ (the scattering angle) or $\mathbf{q}$ (the scattering vector). The summation across all $\mathbf{q}$ gives the total scattering cross section, $\sigma$, given in equation 3.10,

$$\sigma = \frac{\text{no. of scattered neutrons s}^{-1}}{\Phi}, \tag{3.10}$$

where $\Phi$ is the incident neutron flux.

This total scattering cross section $\sigma$ accounts for both coherent (where scattered neutrons remain in phase) and incoherent scattering. In general we are most interested in the angular dependence of the coherent scattering and define a differential cross section,

$$\frac{d\sigma}{d\Omega} = \frac{\text{no. neutrons scattered to } \Delta\Omega \text{s}^{-1}}{\Phi\ \Delta\Omega}, \tag{3.11}$$

describing the quantity of $\sigma$ within a solid angle, $\Delta\Omega$, at a given angular direction from the sample.

When analysing the directional dependence of the scattering there are two key terms; the structure factor (which describes the scattering from an array of neighbouring scattering objects e.g. a crystal lattice) and the form factor (which describes the scattering from a single ion).[108] The structure factor imparts the classic wide angle diffraction patterns associated with crystalline materials (e.g. f.c.c. nickel or h.c.p. cobalt). The form factor, alternatively, is of little interest for bulk materials as the dominant lengths, the size of the bulk crystal and of an individual atom, are beyond the range of detection. However, for nano-particulate systems the form factor dominates the SANS analysis.[121]

### Form factor

The form factor describes the amplitude of scattering that occurs at a given momentum transfer vector, $\mathbf{q}$, and arises from the Fourier transform of the real space density, $\rho(r)$, distribution about the centre of mass,

$$f(q) = \int \rho(r) e^{-i\mathbf{q}.\mathbf{r}} dV. \tag{3.12}$$

In the case of nano-particulate systems we will generally assume a near-spherical

shape and so to simplify we can convert the Fourier transform to polar co-ordinates and, for a sphere of radius $R$, $\rho$ simplifies to 1 if $r \leq R$ and 0 if $r \geq R$ resulting in equation 3.13,

$$f(q) = 4\pi \int_0^R \frac{\sin(qr)}{qr} r^2 dr. \tag{3.13}$$

Carrying out the integration furnishes the form factor for a sphere, [54]

$$f(q) = V \frac{3\left[\sin(qR) - qR\cos(qR)\right]}{(qR)^3}, \tag{3.14}$$

where the measured scattering is proportional to $\frac{f(q)^2}{V^2}$. So, for any size monodisperse spherical scatterer we now have a universal description, when expressed in terms of $qR$, of the pattern arising from a single body, consisting of a mixed sine wave oscillation and an $qR^{-6}$ dependence. From the sine wave term we can predict the first minima of the oscillation will be at $qR \approx 4.49$ (i.e. the first point where $\sin(qR) = qR\cos(qR)$) while the higher $qR$ scattering will rapidly decrease due to the high power term. [122]

If we assume that scattering useful to analysis occurs at $q \geq \frac{1.44}{R}$ and a neutron wavelength of 6 Å, a sample-detector distance of $\approx 10$ m, a beam stop of $\approx 0.1$ m height and a detector radius of $\approx 1$ m the first minima would be measurable for spherical scatterers with radius between $\approx 20$ and 200 Å. This range is greater than an individual atoms, however, if a nanoparticle is approximated to a continuous scattering media as opposed to a collection of atoms they will produce features within this range (with larger sizes explored by moving the detector further from the sample).

### Magnetic neutron scattering

As previously mentioned, neutrons are of particular interest due to their inherent magnetic moment, allowing for both nuclear and magnetic scattering to be analysed. The neutron is a spin $\frac{1}{2}$ particle but possess a greatly reduced magnetic moment compared to the electron. [123] The result of this is the neutron will couple with the magnetisation of sample with only a weak perturbation of the system. The neutron interacts with the samples magnetisation via the dipole dipole interaction creating a torque, given in equation 3.15 where $\mathbf{m}$ is the magnetic moment of the neutron and $\mathbf{B}$ is the magnetic field created by the samples magnetisation. Unlike structural scattering, the magnetic scattering occurs between a vector and a vector field, and

hence has an anisotropy, meaning that scattering is strongest perpendicular to the direction of the sample magnetisation.

$$\tau = \mathbf{m} \times \mathbf{B} \tag{3.15}$$

**Experimental neutron diffraction**

The neutron diffraction studies presented within this thesis were all carried out at the Institut Laue Langevin (ILL), Grenoble using the D33 instrument (see figure 3.4).[124] The ILL uses a fission reactor source (as opposed to the spallation source utilised at other facilities, e.g. ISIS and the Paul Scherrer Institut) producing a continuous flux of neutrons. The neutrons are moderated to supply an incident beam of thermal neutrons with energy $\approx 0.025$ eV, from which a wavelength is selected via a "chopper" ($\lambda = 6$ Å, $\frac{\Delta\lambda}{\lambda} \approx 10\%$).

A small guide magnetic field is applied to the incident neutrons in order to limit the polarisation to two orientations, parallel and anti-parallel to the field. The D33 instrument is then fitted with a neutron super mirror allowing one polarisation of neutron to be transmitted, with the other polarisation excluded by reflection. This beam of polarised neutrons then passes through a spin flipper which, when switched on, reverses the neutron polarisation, prior to the sample. Following scattering the neutron is captured using a bank of $^3$He detectors, following the process,

$$^1\mathrm{n} + {}^3\mathrm{He} \rightarrow {}^3\mathrm{H}^+ + {}^1\mathrm{H}^+ + 0.764 \text{ MeV} \tag{3.16}$$

where the excess energy ionises the carrier gas ($CF_4$) and the resulting charged species detected at an electrode. This method of neutron capture only measures the position of the scattered neutrons, not the energy, and hence cannot discern between elastic and inelastic scattering.

## 3.2 Nano-nickel synthesis

### 3.2.1 Nano-particle synthesis

In order to develop a crystallite sizing method for Johnson-Matthey (JM) catalysts it is important to have a well understood system against which measurements and analysis can be compared and used to corroborate a new technique. The problem with catalytic materials is that the current sizing techniques have limited accuracy

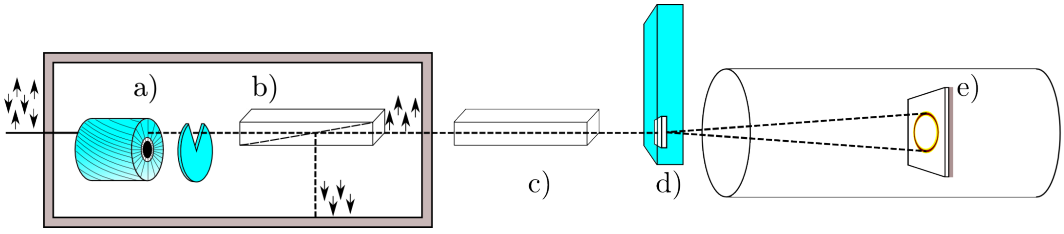


Figure 3.4: Schematic representation of the D33 instrument at the ILL. The incident neutrons begin un-polarised and with a wide energy band prior to the "chopper" (a) at which point the wavelength is selected. Following this the neutrons are polarised via a supermirror (b) before a series of neutron guides (c) directing the neutrons to the sample space (d). The neutron scattering is then mapped using a 2D bank of $^3$He detectors (e).

and precision. Hence, nanoparticle - which can be synthesised with a high degree of reduction, a tight poly-dispersity, and are simple to image via TEM [125] - will serve as a "gold standard" by which we can confirm the accuracy and precision of our magnetic granulometry analysis.

Nanoparticle materials have been synthesised via a colloidal stabilisation method in which surfactants are used to produce a micellar system. [52] Each of these micelles then function as a nano-reaction chamber - ensuring the particles produced have a spherical morphology, a tight poly-dispersity and preventing agglomeration of the particles post-synthesis.

In a typical synthesis an organometallic precursor, nickel acetylacetonate ($Ni(acac)_2$, 1 mmol, 58.7 mg), was added to a surfactant system comprising oleyl amine (OA, 21 mmol,7 ml) and trioctylphosphine (TOP, 3 mmol, 1.34 ml) and the mixture degassed via three alternating treatments with nitrogen gas and vacuum. This mixture was then heated to 130 °C while under a continuous flow of nitrogen to remove the final vestiges of trapped gas. The mixture was held at 130 °C for 20 minutes before rapidly heating the solution to 250 °C and holding at this temperature for 30 minutes. After this time the solution was allowed to cool to room temperature and the nanoparticles dispersed via the addition of ethanol.

The nanoparticles were isolated via centrifugation of the ethanol solution and decanting of the excess ethanol/ surfactant system. The isolated nanoparticles are stored under hexane to prevent agglomeration and to minimise the safety issues associated with fine nickel powder.

Fine particulate nickel has been linked to multiple medical conditions, especially when delivered via aerosol, [126] with suggested carcinogenic properties. [127]

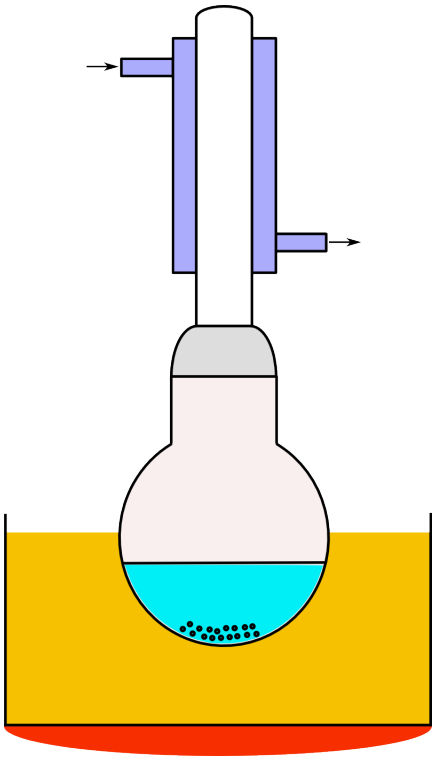

Figure 3.5: Schematic of the solution based reaction for the synthesis of nanoparticles. The oil bath (orange) allows for the reaction to be heated homogeneously

However, these risks can be minimised by avoiding working with the material in the dry state, while in solution or dispersed in a gel, the particulates are relatively safe to handle. To minimise associated health risks, the nano-particulate systems in this thesis were always stored in solution, deposited into a grease or used with excess surfactant to avoid aerosol formation.

### 3.2.2 Catalyst synthesis

The nickel catalysts used within industry are generally prepared via one of two methods, the precipitation or impregnation processes. Our studies have focused on precipitation catalysts as the process will generally give a larger catalysts surface area and a higher loading of metal on the catalyst support.[128] The higher surface area means a higher catalyst activity and is a result of having a smaller average crystallite diameter ($\approx 5-15$ nm). The smaller precipitation catalysts, however, have also been linked to a rapid decrease in catalyst activity during the steam reforming reaction (as a result of sintering, oxidation or poisoning of the catalyst). The ability to follow changes in the crystallite size distribution on a short time scale would allow for this catalytic deactivation to be followed, and possibly prevented, on an industrial scale.

When synthesising a precipitation catalyst the aim is to produce a low solubility Ni species from a high solubility precursor. The result of this is the Ni species rapidly crashes out of solution, favouring multiple nucleations over sample growth and hence giving a plethora of small crystallites. These reaction kinetics have been achieved by reacting nickel nitrate with a mixture of sodium hydroxide and carbonate (all of which have a high solubility) to produce a mixed nickel hydroxide-carbonate (with a low solubility) which will readily decompose on heating to a nickel oxide catalyst, with a typical reaction given in equation 3.17.

$$2Ni(NO_3)_2 + 2NaOH + 2Na_2CO_3 \rightarrow Ni_2(OH)_2CO_3 + 4NaNO_3 \tag{3.17}$$

Following synthesis, the nickel hydroxide-carbonate precipitate is filtered from the remaining solution before being dried and calcined prior to being mixed with a support material. For our studies, a calcium carbonate cement has been chosen as the support media in order to increase the dispersity and rigidity of the catalysts. The resulting catalyst/ support system is compressed into cylindrical extrudites of $\approx$ 3 mm length and diameter. If these catalytic extrudites were to be used in industrial plants they would be thermally treated prior to use to decompose the

mixed hydroxide-carbonate species to an oxide and then reduced under a flow of hydrogen gas.

In our studies, Johnson-Matthey (JM) have supplied three samples synthesised from the same chemical reaction conditions but with a final reduction treatment carried out at different temperatures for different lengths of time. This final thermal treatment step aims to give a range of crystallite sizes and degrees of reduction while keeping all other synthesis related parameters constant. The parameters for the thermal treatment are given alongside the catalyst characterisation work in section 5.1.

# Chapter 4

# Magnetic properties of nickel nanoparticles

In order to assess the usefulness of magnetometry as a characterization technique for catalytic systems it is important to first determine the limitations from the study of an ideal system. The catalysts used industrially for the Fischer-Tropsch and steam reforming processes are complex, both physically and chemically, with variations in degree of reduction, surface area and metal-support interaction having all been linked to the catalytic profile.[129;130] As these factors can be reflected in magnetisation studies (e.g. a decreased degree of reduction will lead to a change in magnetic saturation[131]) a system in which only particle volume varies will first be investigated in order to devise and test the data analysis and magnetisation models that will later be applied to catalytic materials. To this end, the magnetic studies of a series of colloid stabilized nickel nano-particles are presented.

Nanoparticles have the advantage over catalysts that they can to be prepared with different average particle sizes via experimentally simple methods - variations in reduction temperature and surfactant system - while giving consistent degrees of reduction, particle morphology (spherical, ellipsoid, hemispherical etc.) and similar surface chemistry.[132] As a result variations in the magnetic responses between different synthesis will be dominated by volume dependent effects. This study will also look for evidence of the surface effects previously reported[46] and hence correct the particle sizes predicted from the super-paramagnetic models for the surface contributions.

## 4.1 Synthesis of samples A & B; variation of particle size via thermal treatment.

### 4.1.1 Colloidal nanoparticle synthesis

Two samples of nickel nanoparticles (Ni NP) were synthesised via the procedure described in section 3.2.1. The samples were stored in a hexane solution to prevent oxidation over time, preserving the magnetic structure, and to prevent agglomeration.[133] In order to vary the particle size between the two preparations the temperature of the $Ni(acac)_2$ reduction step was varied (210 and 250 °C respectively). By increasing the reduction temperature the rate of precursor decomposition is increased generating more of the metallic species and hence larger particles.[134] A longer reduction dwell period may provide similar results but in both cases the risk of secondary nucleation, and the creation of a bimodal distribution, is increased.[125]

### 4.1.2 TEM analysis

TEM images of the NP samples, prepared by evaporation of the hexane solution onto a carbon coated Cu TEM grid, were taken with a Tecnai F20 Transmission Electron Microscope operating at 200 kV. Figure 4.1 shows a typical TEM image of the two samples. Note that the nanoparticles readily self assemble into periodic arrays on evaporation. This templating is typical of NP systems with a narrow polydispersity,[135] leading to the formation of a "colloidal crystal" structure.

EDX (Energy Dispersive X-ray) spectroscopy carried out during dark field imaging showed that the particles are composed primarily of nickel with small signals present for phosphorous, nitrogen, silicon and copper. The initial synthesis is responsible for the Ni, P and N peaks and the TEM grid is Cu rich. The Si signal is likely contamination from silicon-rich vacuum grease, either from the TEM or used during synthesis to ensure an inert atmosphere.

Figure 4.2 shows images of the two samples at a higher magnification. Sample A has been deposited from a lower concentration solution, giving a single monolayer of NPs (suggested by the lack of shadowing and continuous contrast) forming a 2D hexagonal array for the majority of the image. The top left of the image shows the effect of multiple layer formation, with a slight shift of the particles horizontally with a similar 2D layer structure.

Sample B was deposited from a higher concentration hexane solution, giving rise to a multi-layer packing structure. Due to this multi-layer view it is difficult

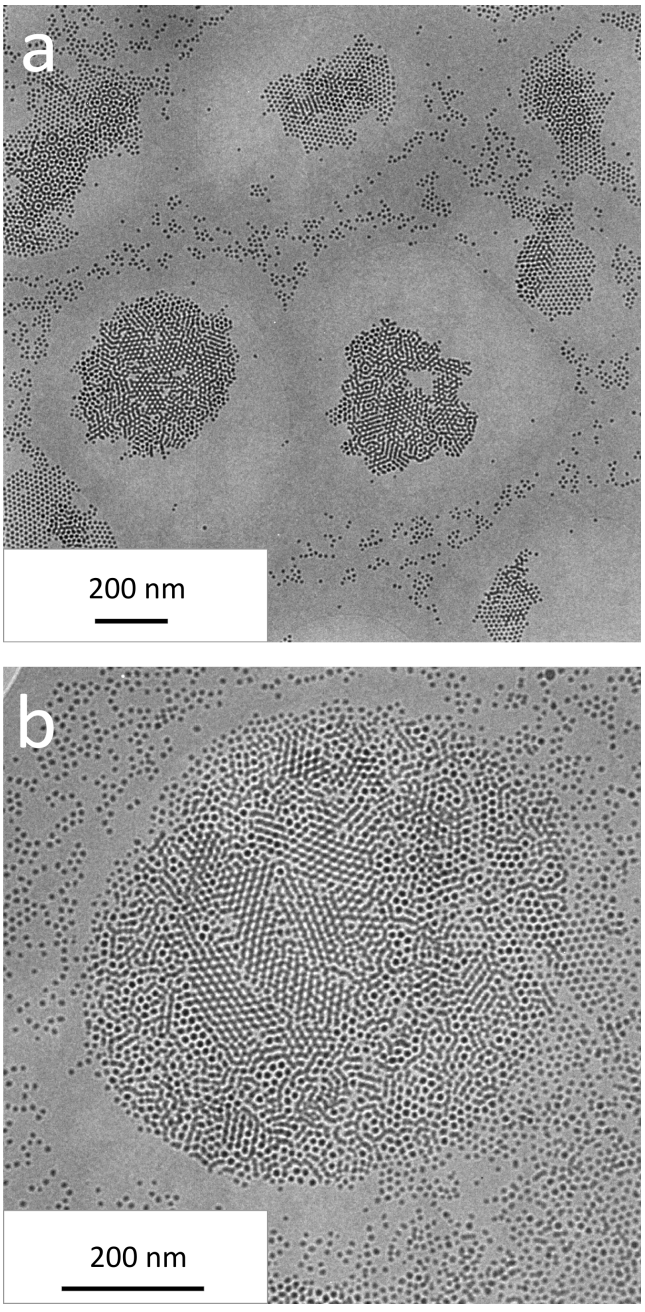


Figure 4.1: TEM images of nickel NP samples made via colloidal reduction methodology for a) (sample A, $T_{Red.} = 210$ °C) and b) (sample B, $T_{Red.} = 250$ °C).

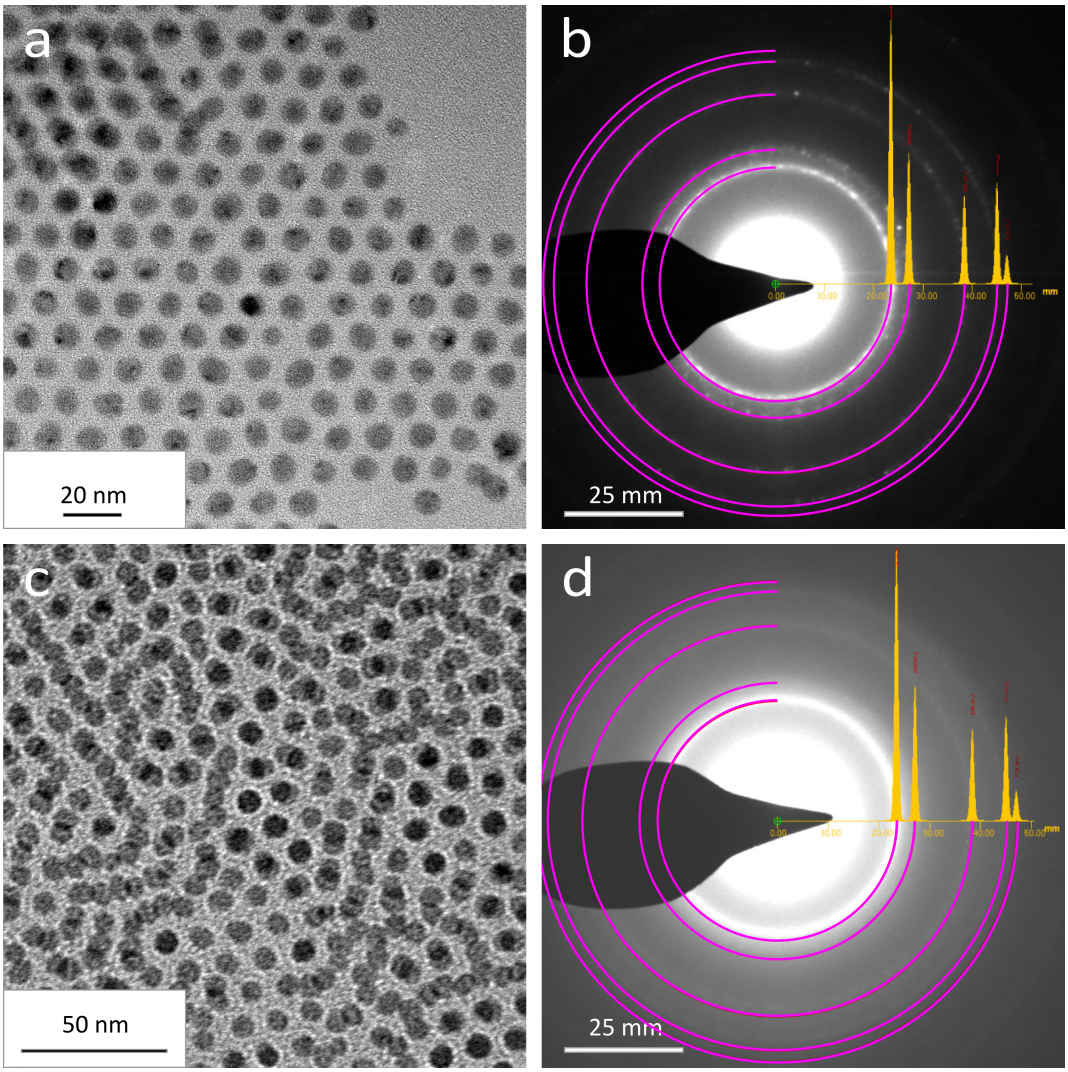


Figure 4.2: High magnification TEM images for sample A (a) and sample B (c) alongside their respective electron diffraction patterns (b & d). Electron diffraction was carried out at 200 kV with a camera-object distance of 2000 mm.

to distinguish a single layer structure for comparison to sample A. Some order is, however, discernible - with repeating triangular units consistent with either an f.c.c or h.c.p. colloidal crystal array. The image for sample B also demonstrates a slight "halo" effect around the Ni NPs of $\approx$ 2 nm - this is evidence that the surfactant system has remained attached to the NP structure during synthesis and deposition. This is less obvious in sample A due to the tight packing of the NP spheres but can be seen in lower magnification images.

Sample A and B both appear to have quite narrow polydispersity, both from the similarity in the images and their structured packing, and have a near spherical morphology. From observation it appears both samples have a similar average particle diameter, $\approx$ 8 nm.

Figure 4.2 also shows the electron diffraction patterns obtained during TEM. Both diffraction patterns are consistent with a powder average, due to the ring features at each diffraction index, implying a random distribution of crystallographic directions. It is necessary to confirm a random orientation as the presence of the colloidal crystal structure implies some form of self assembly mechanism which may have affected the NP orientations and the theoretical models describing NP magnetism, e.g. the Stoner-Wohlfarth criteria,[41] assume a random orientation of crystallographic axes.

Assuming the electrons have a wavelength of 2.5 pm, based on an acceleration energy of 200 kV, the observed diffraction pattern has scattering vectors $Q = 2.95, 3.40, 4.77, 5.59$ and $5.90$ Å$^{-1}$. This pattern is consistent with an f.c.c. crystal structure[136] with the peaks arising from the (111), (200), (220), (113) and (222) reflections respectively, giving a lattice constant, $a_{Nano} = 3.70(1)$ Å compared to the bulk value, $a_{Bulk} = 3.5238$ Å,[137] possibly arising as a result of the increased surface states and the possibility of intercalation of surfactant materials. A similar sized increase in $a$ has previously been observed in cerium oxide nanoparticle[138] over the diameter range 1 - 100 nm.

A shift in $\alpha_{Nano}$ is to be expected due to the change in crystal stress and strain associated with a greater surface contribution and leads to an increase in the unit cell volume, $V_{Nano} = 50.6(4)$ Å$^3$ cf. $V_{Bulk} = 43.6$ Å$^3$, and hence a decrease in density, $\rho_{Nano} = 7.68(6)$ g cm$^{-3}$ cf. $\rho_{Bulk} = 8.908$ g cm$^{-3}$. It should be noted that the error in $\rho_{Nano}$ only reflects the random error, discounting systematic errors such as an inaccurate camera-object distance or a gradient in lattice constants from bulk to core, and hence may be an under-estimate of the true uncertainty.

Figure 4.3 shows the distribution of particle diameters for samples A and B

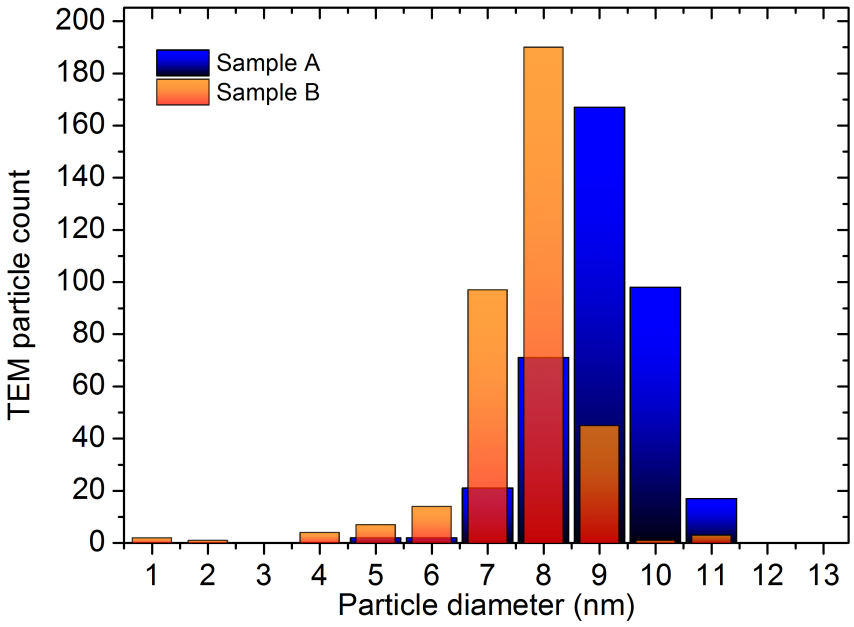


Figure 4.3: Particle diameter histograms for sample A (blue) and B (orange) determined from TEM analysis. The particle size distributions for sample A and B have average size $\mu_A = 8.88(7)$ nm and $\mu_B = 7.69(6)$ nm and standard deviations $\sigma_A = 1.38$ nm and $\sigma_B = 1.13$ nm respectively.

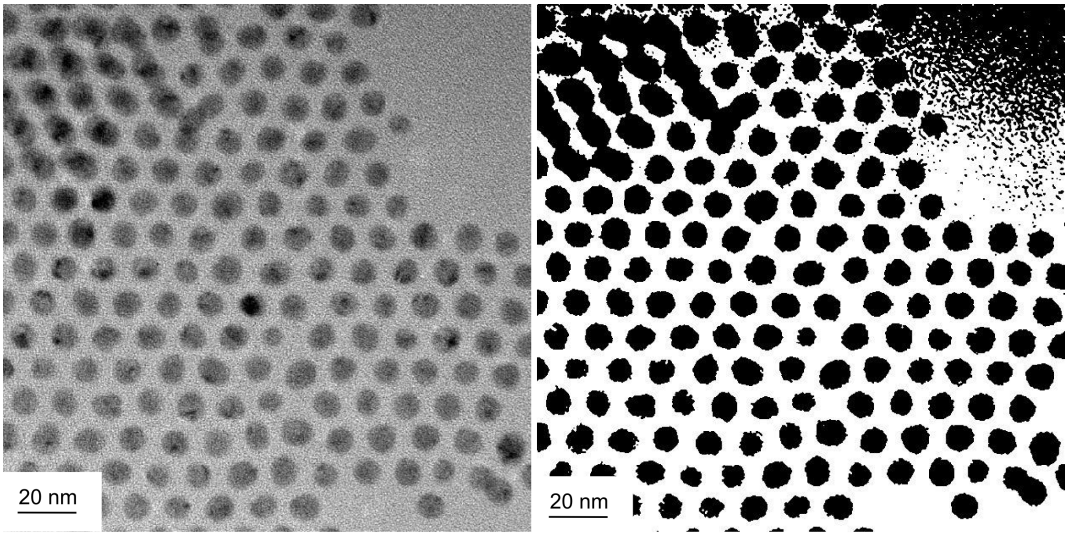


Figure 4.4: A typical example of the image processing, showing the TEM image for sample A before and after the binary threshold.

determined from the TEM images. The particle sizing method assumes that each nanoparticle is a spherical body, with the equatorial cross section of each particle projecting a circular image. The sizing was carried out using the ImageJ software [139] - using the image sale bar as a pixel-nm conversion factor, and the preprogrammed algorithms to carry out a binary threshold, with an example conversion shown in figure 4.4.

The contrast threshold method results in parts of the image background, arising from the lacey carbon grid used for sample mounting, becoming small features and hence the sizing method needs to be limited to particles with a cross-sectional area $\geq 1$ nm$^2$. In addition to excluding particles below a minimum cross-sectional area, points at which two particles overlap can be defined based on the "circularity" - done within imageJ using the ratio between the area, $A$, and perimeter, $P$, of each particle via the equation

$$\text{Circ.} = 4\pi\frac{\text{A}}{\text{P}^2}. \tag{4.1}$$

The circularity then depends on the surface roughness of the cross section and if the particles are elongated along an axis, ranging from 1 for a circle to 0. On converting the TEM images to a black and white image, the grainy features of the image result in a roughening at the edges, meaning the circularity is less than 1 in each case, and on sizing was limited to a range of 0.6 - 1. This process results in $\approx$ 20% of the

particles being rejected, due to non-circularity arising from particle overlap. The rejected particles are generally in the area of images where multi-layers of particle stacking have formed, and so most TEM images for analysis have been taken from regions of low particle density.

Th approach to particle sizing would struggle to differentiate between morphologies that would have the same 2D projection (e.g. nanospheres vs nanorods stacked vertically) however, with no evidence of non-spherical structures under lower amplifications alongside a random crystallographic orientation it appears to be a fair assumption for this system. The particle size histograms serve to reinforce the conclusions drawn from figures 4.1 and 4.2. Sample A and B have relatively similar average particle diameters, $\mu_{diameter}$ = 8.88(7) and 7.69(6) nm respectively, and standard deviations, $\sigma$ = 1.38 and 1.13 nm. Sample B, however, appears to have undergone some secondary nucleation, leading to the formation of a limited number of much smaller NPs ($\approx$ 1 - 2 nm). These are likely to be the reason for the disruption in the particle packing in sample B.

## 4.2 Magnetization studies of sample A

DC magnetization measurements were carried out using a Quantum Design MPMS SQUID magnetometer with samples mounted via dispersal of the Ni NP solution into a commercially available fluorinated grease, Fomblin, and allowing the hexane to evaporate at room temperature. This dispersal method was used due to safety concerns associated with fine powder Ni (carcinogenic, toxicity etc.)[140] and in order to reduce the inter-nanoparticle magnetic effects - previously demonstrated to arise from long range RKKY interactions[141] and dipole-dipole interactions.[142] Previous studies[143] have suggested such effects become prominent at loadings above $\approx$ 4%, hence only a low loading of NP was used, $\approx$ 1 - 2%. Unfortunately due to the low loadings and hazards associated with the thermal decomposition of fluorinated greases (HF formation) the loading of Ni cannot be consistently determined.

### 4.2.1 Evidence of single domain ferromagnet behaviour.

The first step to studying the magnetism of these materials is to determine if the particles are still within the single domain ferromagnetic limit, $d \approx 50$ nm for Ni.[103] Figure 4.5 demonstrates the magnetic response as a function of applied field for sample A across a range of temperatures. As the temperature is increased there

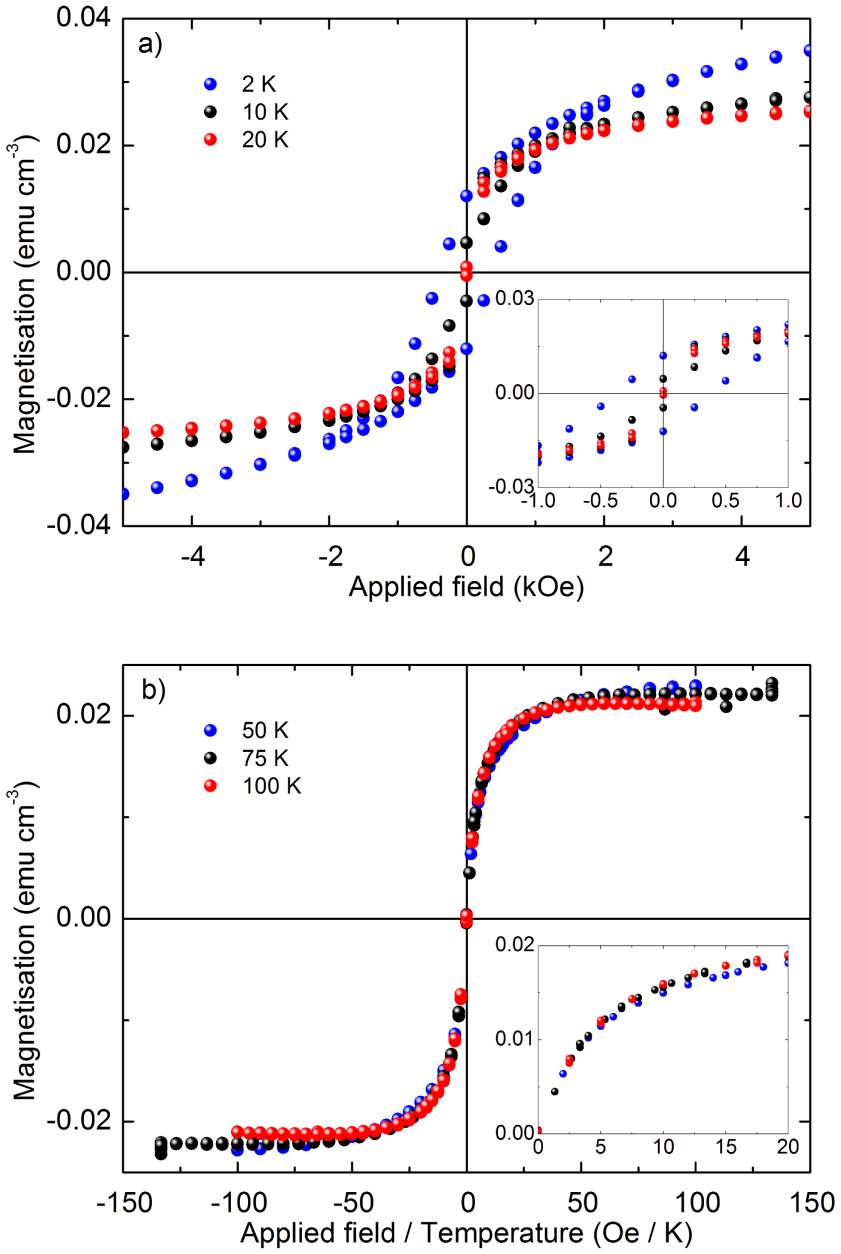


Figure 4.5: Magnetisation ($M$) as a function of applied field ($H$) for Sample A. Figure a; the low temperature ($T$) ferromagnetic response, consistent with the "blocked" magnetic behaviour, at 2, 10 and 20 K (blue, black and red respectively). Figure b; high temperature paramagnetic response at 50, 75 and 100 K (blue, black and red respectively). For a super-paramagnetic response $M$ vs $\frac{H}{T}$ is temperature independent.

is a gradual transition from a hysteretic to a reversible behaviour. This is typical of magnetic NP materials,[42] as previously described in sections 2.2.5 and 2.2.6, and represents the transition from the "blocked" regime, in which the moment is strongly coupled to the underlying crystallography, to the super-paramagnetic regime.

The low temperature magnetisations (figure 4.5a; 2, 10 and 20 K) show a gradual decrease in coercive fields ($H_C$) and remanent magnetisation ($M_R$) as the temperature increases, as previously reported for Ni nanoparticles.[144] The gradual decrease in $M_R$ (12.0, 4.6 and 0.8 $\times 10^{-3}$ emu cm$^{-3}$ at 2, 10 and 20 K) is evidence that, despite a tight radial distribution of particles sizes, the volume distribution is relatively broad - unsurprising given the cubic scaling from a radial to a volume distribution. Interestingly the $M$ vs $H$ data at 2 K has a much higher susceptibility at higher applied fields (2 - 5 kOe) than the 10 and 20 K measurements. This growth of $M_S$ is not described by super-paramagnetic theory, suggesting there is an additional component to the magnetisation. This behaviour looks similar to the growth in magnetisation reported previously for ferrite materials,[96] arising from the surface states. This behaviour is most consistent with a small moment paramagnetic system located in the outer-layer of the nanoparticle structure.

The high temperature $M$ vs $H$ curves (figure 4.5 b); 50, 75 and 100 K) all show a reversible magnetisation, as is to be expected above the blocking temperature, with no $H_C$ or $M_R$. All three curves appear to be approaching magnetic saturation, $M_S \approx 0.02$ emu cm$^{-3}$, though the gradual decrease in magnetisation at magnetic saturation ($\frac{H}{T} = 100$ Oe / K) with increasing temperature over a tight temperature range suggests a diamagnetic contribution to the signal is also present, and has lead to the decrease in agreement between $M$ vs $\frac{H}{T}$ as a function of temperatures at higher fields. This is likely due to the dispersal material used and is a relatively weak susceptibility, $\chi = -0.3(1) \times 10^{-6}$ emu cm$^{-3}$ Oe$^{-1}$. The inset to figure 4.5b shows the low field magnetic behaviour, with $H$ in the range 0 to 1000, 1500 and 2000 Oe respectively. The data has been plotted as a function of applied field / temperature (i.e. $\frac{H}{T}$) as the curve $M$ vs $\frac{H}{T}$ should be $T$ independent for a super-paramagnetic system. The two higher temperatures appear to follow a similar behaviour, however, the 50 K response differs slightly - suggesting a thermal correction term may be required.

The magnetic behaviour of these materials appears at high $T$ to follow the behaviour previously reported for single domain ferromagnetic nanoparticles,[145] however, the divergence of magnetisation at 50 K suggests the presence of inter-particle interactions, similar to the modified super-paramagnetic case discussed earlier in

section 2.1.1.[42] Similarly, the magnetisation at the lowest temperatures (2, 10 and 20 K) demonstrate a growth in magnetisation past the expected Langevin magnetism (saturating at $\approx 0.025$ emu cm$^{-3}$ for $T = 50$ K), as has previously been reported for ferrite systems,[97;96;87] which was assigned to a "glassy" surface magnetisation decoupled from the core, super-paramagnetic moment. These two behaviours need to be investigated before before attempting to determine the particle size via conversion of the average super-paramagnetic moment from the Langevin fitting.[29]

### 4.2.2 Curie-tail behaviour at high $H$.

The high $H$, low $T$ magnetic behaviour appears similar to the magnetic response previously reported for ferrite materials.[96;97] In the previous works a single applied field was used to identify the presence of a Curie tail behaviour. In contrast, we will use multiple $M$ vs $T$ data sets at a range of high applied fields. This has the advantage that the diamagnetic component will manifest as a linear offset, scaling with applied field, allowing the core and shell terms to be separated and quantified. $M$ vs $T$ scans also have the advantage of being less time demanding (as changing $T$ is quicker than changing $H$ on the QD MPMS SQUID).

Figure 4.6 a) shows the magnetisation as a function of temperature in a range of high applied magnetic fields (10, 20, 30 and 40 kOe). These scans illustrate the extent of the small moment paramagnetic term noted in figure 4.5 with a Curie tail like behaviour dominating the magnetic signal at low $T$.

As the temperature increases the magnetic responses cross, with the highest applied field having the smallest magnetisation. This is because the super-paramagnetic term is saturated by $\approx 10$ kOe (as seen in figure 4.5) so an increase in $H$ has no effect, but the diamagnetic signal arising from the Fomblin grease, which is temperature independent, continues to increase with $H$. This serves as both evidence for the diamagnetic properties of the support grease and for saturation of the super-paramagnetic moment.

The Curie-tail behaviour can also be represented as a $\frac{1}{\chi}$ behaviour, as shown in figure 4.6 b). The low $T$ range ($\approx$ 5 to 25 K) shows a near linear response, as would be expected of a Curie behaviour, however the projected $T$ intersect is non-zero, extending into the negative region of the temperature range. Quantifying the magnetic correlations in this way will be misleading, due to the extra magnetic contributions from the Fomblin and saturated Langevin behaviour, so instead a Weiss temperature term will be included in the analysis to follow.

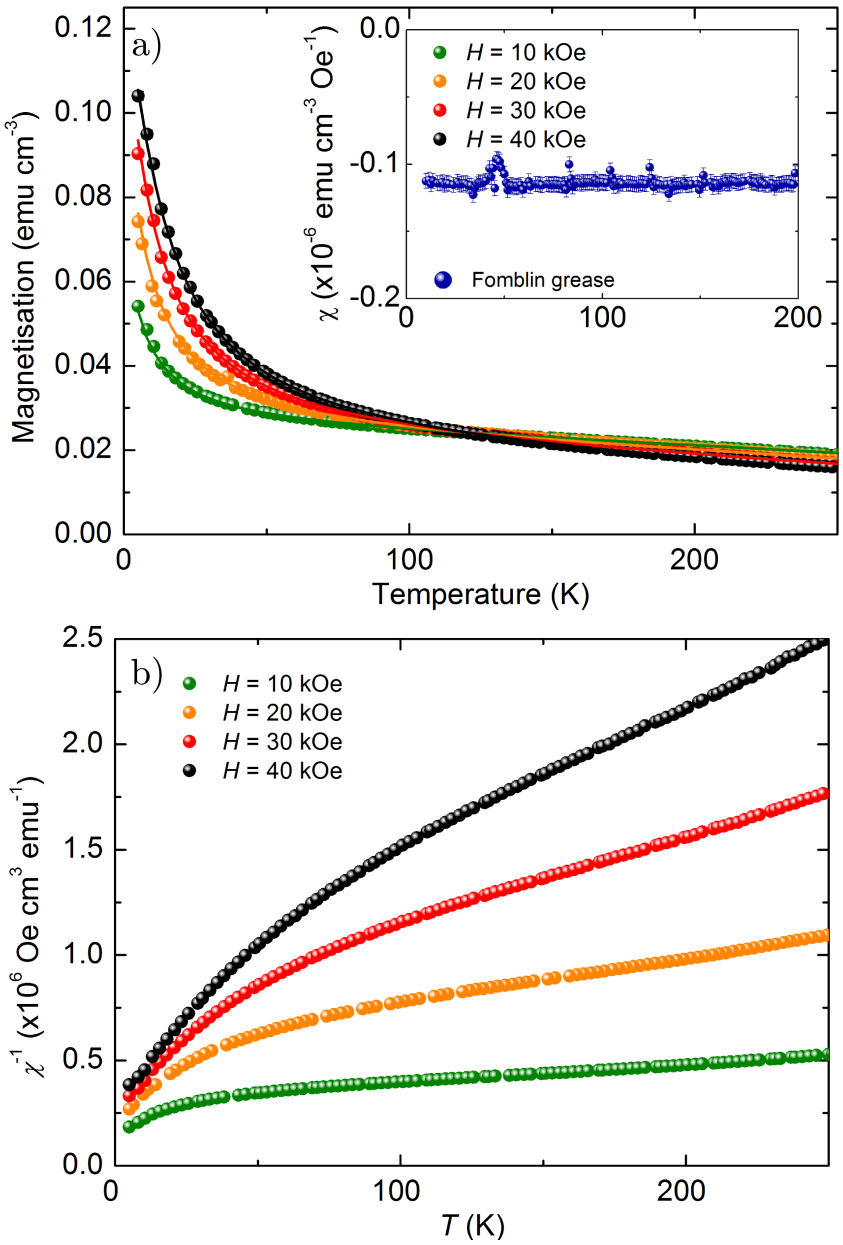


Figure 4.6: a) $M$ vs $T$ curves taken for sample A taken with applied field, $H$, of 10, 20, 30 and 40 kOe (green, orange, red and black receptively) with associated fits to equation 1.3. A clear paramagnetic magnetisation can be seen for $T < 50$ K increasing steadily with applied field. Inset - the $M$ vs $T$ behaviour of Fomblin grease taken at $H = 100$ Oe, with an average susceptibility $\chi = -1.14(3) \times 10^{-7}$ emu cm$^{-3}$ Oe$^{-1}$. The feature at $\approx 40$ K is due to a magnetic transition associated with oxygen trapped within the grease. b) The high $H$ magnetic susceptibility as a function of $T$.

Theoretically, if the super-paramagnetic moments are saturated the magnetisation should still have a small ($H$ independent) temperature dependence as spin waves are created within the array of nano-particles. In the previous studies of ferrite nanoparticles, the saturated core at low $T$ was modelled using a modified Bloch's law,[97]

$$\frac{M(T)}{M(0)} = 1 - \alpha T^p \tag{4.2}$$

where $M(T)$ is the spontaneous magnetisation of a single domain at a temperature $T$ scaled with respect to $M(0)$ (the magnetisation at $T = 0$ K), $p$ is the power dependence ($\frac{3}{2}$ for a bulk ferromagnetic material) and $\alpha$ is a scale factor ($\alpha^p = \frac{1}{T_C}$ for the ferromagnetic case). In the previous studies the power term, $p$, was allowed to vary in order to allow for finite size effects of small particles (2 nm) and the change from ferro- to ferrimagnetic ordering.[146] For the systems studied here the particles are significantly larger (diameter ≈8 nm cf. 2 nm) and are ferromagnetic so we will assume $p = 1.5$ for simplicity.

Based on the previous applications of Bloch's law, a model is suggested for the magnetic response, see equation 4.3, comprising a superposition of three terms - a thermally corrected Langevin function (see equation 4.4) for the unsaturated moments at low $T$, in which $\mu$ is the magnitude of the effective moment, $M_S$ is the magnetic saturation and $\theta$ is a Weiss temperature correction term,[147] a spin-wave term for the saturated moments, in which $\alpha$ is the thermal coefficient and $\beta$ is a scaling factor,[148] and a diamagnetic background, $b$. The fit was carried out on the data collected in the 4 applied fields simultaneously, with shared values for all free parameters, and using the $\chi^2_{red.}$ as a measure of the fit quality. The best fit parameters are listed in table 4.1.

$$M(H,T) = L(\mu, H, M_S, T-\theta) + \beta(1 - \alpha T^{1.5}) + bH. \tag{4.3}$$

$$L(\mu, H, M_S, T-\theta) = Ms\left[\coth\left(\frac{\mu H}{k_B\,(T-\theta)}\right) - \left(\frac{\mu H}{k_B\,(T-\theta)}\right)^{-1}\right]. \tag{4.4}$$

This proposed model appears to give an accurate representation of the magnetisation, with universal values of the super-paramagnetic saturation term, $\beta$, and diamagnetic background, $b$, comparable to those observed at 50, 75 and 100 K. The

| Parameter | Value | Units |
|---|---|---|
| $\mu$ | 9.8(2) | $\mu_B$ |
| $M_S$ | 0.147(3) | emu cm$^{-3}$ |
| $\theta$ | -5.7(1) | K |
| $\alpha$ | $5.2(1) \times 10^{-5}$ | K$^{-1.5}$ |
| $\beta$ | $25.98(5) \times 10^{-3}$ | emu cm$^{-3}$ |
| $b$ | $-2.50(2) \times 10^{-7}$ | emu cm$^{-3}$ Oe$^{-1}$ |
| $\chi^2_{red}$ | 0.72 | n/a |

Table 4.1: Best fit parameters of the model described in equation 4.3 to the high $H$, $M$ vs $T$ data sets reported in figure 4.6. The field independent nature of the spin-wave coefficients $\alpha$ and $\beta$ imply that the core ferromagnetic moments fitted at high $T$ are saturated in all cases. The diamagnetic term, $b$, is consistent with the measured susceptibility of Fomblin grease.

low $T$ Curie tail feature is well described by a Langevin function once this is corrected by a small Weiss temperature term. The universal nature of the spin-wave magnetisation suggests that the super-paramagnetic response is saturated at fields greater than 10 kOe within this temperature range and serves to quantify the diamagnetic response. The requirement for the addition of a negative Weiss temperature term to the Langevin function suggests that there is a weak antiferromagnetic correlation, likely between nearest neighbour single domain particles, as was also suggested from the difference between $M$ vs $\frac{H}{T}$ scans seen in figure 4.5. It should be noted that without the $\theta$ term the quality of fit is lower, $\chi^2_{red} = 6.94$.

This Weiss temperature term implies that the magnetic species which give rise to the Curie behaviour at high $H$ are experiencing an antiferromagnetic correlation. However, the effective size of the magnetic moment of these species are much larger than expected from Ni ($\approx$ 10 nm cf. $0.61\mu_B$ atom$^{-1}$) suggesting that the single domain structure has been repeated on a much smaller scale of $\approx$ 5 to 10 atoms. These micro-domains would be ordered ferromagnetically within each domain, but possess an antiferromagnetic correlation with respect to their neighbouring groups. If these surface moments exist as a spin glass structure then the magnitude and inter micro-domain correlation (antiferromagnetic or ferromagnetic) could change from sample to sample due to the random nature of the structure and interactions.

With an understanding of the growth in magnetisation at low $T$ it may be possible to correct the Langevin analysis of the super-paramagnetic magnetisation curve for any inter- or intra-particle correlations as has been done in the case of the modified super-paramagnetic system.[147] However, in order to do this analysis we

need to know two factors - the temperature range above which the magnetisation is reversible and the scale of the Weiss constant needed to give a universal $M$ vs $\frac{H}{(T-\theta)}$ behaviour. To identify these two terms we will now examine the low $H$ (100 Oe), $M$ vs $T$ behaviour.

### 4.2.3 Corrected Langevin function analysis.

Figure 4.7 shows the magnetic behaviour of sample A as a function of temperature, after both zero-field cooling (cooled from 100 K to 2 K with $H_{cool} = 0$ Oe and $H_{measure} = 100$ Oe) and field cooling (cooled from 100 K to 2 K with $H_{cool} = 10$ kOe and $H_{measure} = 100$ Oe). At low temperatures the two magnetisations ($M_{ZFC}$ and $M_{FC}$) differ but above $T \approx 40$ K they follow the same temperature dependence. This field cooling dependence emphasises the low $T$ hysteretic behaviour - with $M_{FC}$ reflecting the remanent magnetic behaviour and $M_{ZFC}$ the initial magnetisation, taken when the moments are randomly orientated. The loss of this difference between $M_{FC}$ and $M_{ZFC}$ is evidence that the moments have entered the super-paramagnetic regime.[56]

The $T$ range over which $M_{ZFC}$ and $M_{FC}$ have the same behaviour can be used to determine the thermal correction to the Langevin behaviour. The simplest approach would be to fit to a Curie-Weiss law[63] (see equation 4.5) making the assumption that at $H = 100$ Oe the low field approximation holds. However (as the inset to figure 4.7 shows) the background corrected $\frac{1}{\chi}$ is non-linear within this regime - suggesting the low field approximation no longer holds and instead a Weiss-corrected Langevin function (see equation 4.4) is required. The fit is carried out using the same diamagnetic background term, $b = -2.50(2) \times 10^{-7}$ emu cm$^{-3}$ Oe$^{-1}$, and magnetic saturation, $M_S = 25.98(5) \times 10^{-3}$ emu cm$^{-3}$, found during the high $H$ analysis. Within this temperature range and at a low applied field, $H = 100$ Oe, the small moment paramagnetic term will be ignored as the magnetisation will be small compared to the diamagnetic background. The resulting best fit to the high temperature response is displayed on figure 4.7 as the black line and the best fit parameters to this model are given in table 4.2. This model can be compared to the equivalent fit to the simpler Curie law, resulting in a $\chi^2_{red} = 6.61$, demonstrating the necessity of the Weiss temperature term.

$$\chi = \frac{C}{T - \theta}. \tag{4.5}$$

A negative value for the Weiss temperature, $\theta$, supports the earlier evidence

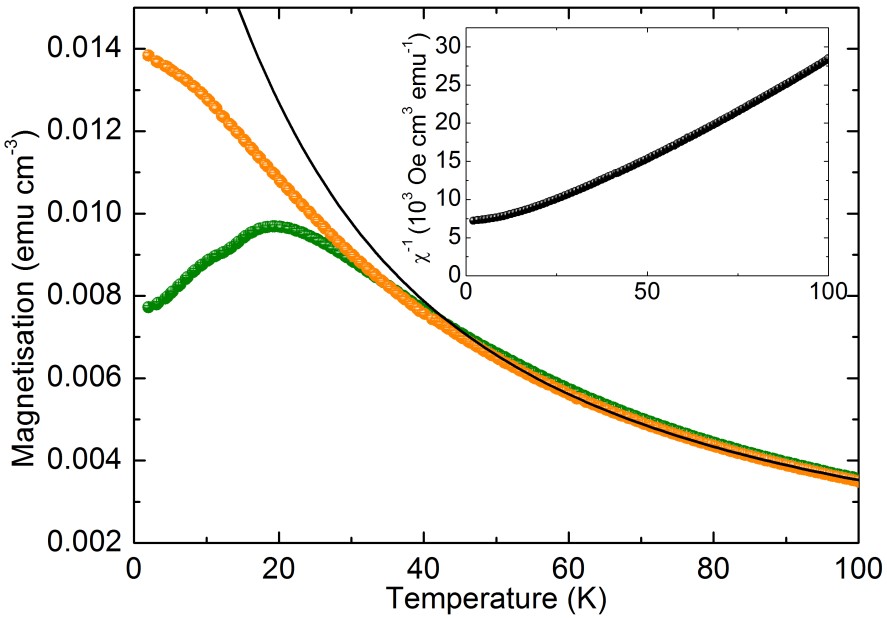


Figure 4.7: $M$ vs $T$ behaviour of sample A taken at $H = 100$ Oe in both ZFC (green) and FC (orange) conditions. Below $T \approx 40$ K the $M_{ZFC}$ / $M_{FC}$ difference is obvious. The higher temperature magnetisation has no hysteretic behaviour, in agreement with figure 4.5. The black dashed line is a fit of the Curie-Weiss law to the data - corrected for a small $T$ independent diamagnetic term. Inset -the $\chi^{-1}$ behaviour of the FC data set. Above 50 K the data is non-linear, suggesting the low field approximation of the Langevin function does not apply at $H = 100$ Oe.

| Parameter | Weiss-corrected Langevin | Units |
|---|---|---|
| $\mu$ | $6.59(2) \times 10^3$ | k$\mu_B$ |
| $\theta$ | -4.6(2) | K |
| $\chi^2_{red}$ | 1.01 | n/a |

Table 4.2: Best fit parameters for the Curie-Weiss model to the high $T$, $M$ vs $T$ response of sample A at $H = 100$ Oe.

for some form of antiferromagnetic correlation between single domain nanoparticles. Such a Weiss temperature correction has previously been reported,[149] arising due to inter-particle dipole-dipole or RKKY interactions. The RKKY interactions would require a conductive media, which a fluorinated hydrocarbon grease will not supply, suggesting it is the dipole-dipole interaction that is responsible for the correlations. For atomic systems, dipole-dipole interactions are relatively weak, however, the increased moment of the super-paramagnetic system can lead to an increased interaction strength. The energy of a dipole-dipole exchange is given by,

$$E = \frac{\mu_0}{4\pi r^3}\left[\boldsymbol{\mu}_1.\boldsymbol{\mu}_2 - \frac{3}{r^2}(\boldsymbol{\mu}_1.\boldsymbol{r})(\boldsymbol{\mu}_2.\boldsymbol{r})\right] \tag{4.6}$$

where $\mu_0$ is the vacuum permeability constant and $\boldsymbol{\mu}_1$ and $\boldsymbol{\mu}_2$ are the vectors for the two interacting magnetic dipoles separated by the distance $r$.[63] Based on a magnetic moment of $\mu \approx 6{,}600\ \mu_B$ and an average inter-particle distance $r \approx 20$ nm (expected average inter-particle distance at a loading of 4%) this would give an interaction of $\frac{E}{k_B} \approx 6$ K, with the dipole-dipole interaction linked to either ferromagnetic or antiferromagnetic correlations.[142] So, the dipole-dipole interaction is strong enough at this low loading to give a slight modification to the paramagnetic behaviour.

Now that a thermal correction has been identified, it can be used to correct the Langevin function (allowing for any magnetic correlations[150]) and the average moment per particle can be determined via analysis of the reversible magnetic behaviour. From inspection of the $M$ vs $T$ behaviour (see figure 4.7) it is clear that the magnetisation above $\approx 50$ K is independent of $H_{cool}$ so the analysis will be carried out using data sets at $T = 75$ and 100 K with a shared diamagnetic correction - note that this background term will have a slightly decreased magnitude compared to the "three term" model as the magnetic component arising from the "high $H$ Curie-tail", paramagnetic moments can be approximated to a positive linear $\chi$ at high $T$.

Figure 4.8a shows the fit to the expected Langevin behaviour, corrected by the Weiss temperature (see equation 4.4) where $M$ is the magnetisation, $M_S$ is the saturation magnetisation, $\mu$ is the magnitude of the magnetic moment, $H$ is the applied magnetic field, $T$ is the system temperature and $k_B$ is the Boltzmann constant. The fit was carried out simultaneously on the $M_{75\ \mathrm{K}}$ and $M_{100\ \mathrm{K}}$ data sets fixing $\theta = -4.6$ K and sharing values for $\mu$, the average magnetic moment per particle, and $b$, the diamagnetic correction term, between both data sets. The best fit parameters are listed in table 4.3 for the single Langevin model. The single Langevin

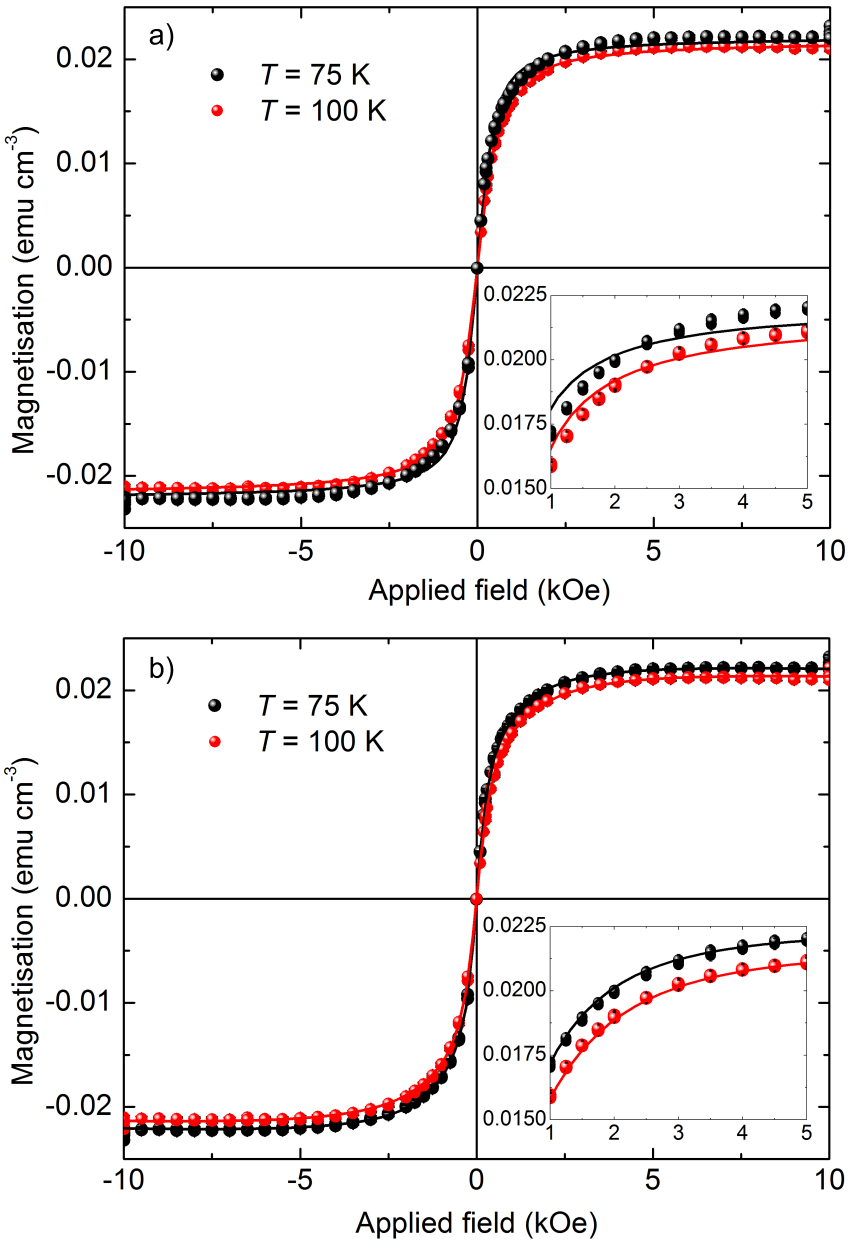


Figure 4.8: $M$ vs $H$ response for sample A at 75 and 100 K (black and red) fitted with a single Langevin function (a) $\chi^2_{Red} = 8.27$) or a dual Langevin function (b) $\chi^2_{Red} = 0.97$) corrected in both cases by a diamagnetic background. Inset - re-plotted at higher magnification.

| Parameter | Single Langevin model | Dual Langevin model | Units |
|---|---|---|---|
| $\mu_1$ | 6.50(6) | 9.9(1) | k$\mu_B$ |
| $\mu_2$ | n/a | 2.00(6) | k$\mu_B$ |
| $M_{S1(75\ \mathrm{K})}$ | $22.2(1) \times 10^{-3}$ | $14.4(2) \times 10^{-3}$ | emu cm$^{-3}$ |
| $M_{S2(75\ \mathrm{K})}$ | n/a | $9.6(2) \times 10^{-3}$ | emu cm$^{-3}$ |
| $M_{S1(100\ \mathrm{K})}$ | $21.8(1) \times 10^{-3}$ | $15.0(2) \times 10^{-3}$ | emu cm$^{-3}$ |
| $M_{S2(100\ \mathrm{K})}$ | n/a | $8.5(2) \times 10^{-3}$ | emu cm$^{-3}$ |
| $b$ | 0(2) | $-1.3(1) \times 10^{-7}$ | emu cm$^{-3}$ Oe$^{-1}$ |
| $\chi^2_{red}$ | 10.8 | 0.97 | n/a |

Table 4.3: Best fit parameters for the Single and Dual Langevin $M$ vs $H$ response for sample A (see figure 4.8).

model is the simplest approach to modelling the magnetic response of these materials,[36;52] however, the relatively large value of $\chi^2_{red}$ suggests it is unsuitable. A close inspection of the data (figure 4.8 Inset) reveals that the model both overestimates $\frac{M}{Ms}$ at low $H$ and underestimates $\frac{M}{Ms}$ at high $H$.

An improved model is suggested in which the magnetic response consists of a super-position of two Langevin functions, again corrected by a diamagnetic magnetisation and the experimentally derived Weiss temperature. Each Langevin function is individually weighted by its $M_S$ value. The fit was carried out following the same procedure, fitting both $M_{75\ \mathrm{K}}$ and $M_{100\ \mathrm{K}}$ data sets simultaneously, sharing values of $\mu_1$ and $\mu_2$, the magnitudes of the magnetic moments, $b$, the diamagnetic correction term, and $\theta = -4.6$ K (from the earlier $M$ vs $T$ analysis). The best fit parameters are displayed in table 4.3 for the dual Langevin model - with a $\chi^2_{red} \approx 1$. Figure 4.8b displays the dual Langevin model, both across the full data range and in the region the single Langevin model diverged.

The dual Langevin model appears to accurately reproduce the magnetisation of this nano-particle system - however, the physical meaning of this model needs to be considered. In the literature, it is generally assumed that a nano-particle system of this type will have a log normal distribution of particle sizes[29;151;152] - due to the nucleation/ growth kinetics of the synthesis. As demonstrated in section 2.3.2, a log normal distribution of magnetic particles can be modelled by a pair of Langevin functions - occurring at $\approx 20\%$ and $80\%$ of the cumulative distribution. If we assume that this system follows a similar behaviour we can expect a mean moment per particle, $\mu_{average} = 4.45(7)$ k$\mu_B$.

### 4.2.4 Magnetic moment to volume conversions.

These values of $\mu$ deduced from the corrected Langevin method can then be converted into particle sizes, assuming the bulk magnetisation of Ni,[153] 0.61 $\mu_B$ atom$^{-1}$, and the density calculated from electron diffraction, $\rho = 7.68(6)$ g cm$^{-3}$. These calculations result in an average particle size $d_{mean} = 5.6(1)$ nm with $20 - 80\%$ limits at $d_{20\%} = 4.2(1)$ nm and $d_{80\%} = 7.3(1)$ nm. Comparing these values to the particle sizes observed under TEM, $d_{TEM} = 8.88(7)$ nm with a range over 7 to 10 nm, this appears to underestimate the actual particle size by $\approx 3$ nm. This is consistent with previous work,[52] which suggests the outer-layer exists as a magnetic "dead layer".

It is possible that this outer structure consists of the species that give rise to the high $H$ Curie-tail as suggested for the ferrite materials.[97;154] The evidence so far suggests a core-shell model in which the core consists of a traditional single domain moment surrounded by a shell of micro domains ($\approx 10$ $\mu_B$ per site) with a weak antiferromagnetic correlation to the core. If this is true then the size of the "dead-layer" and the saturated magnetisation of the smaller magnetic species should be linked.

The magnetic volume calculated at this point represents the high $T$ saturation, while our earlier analysis of the high magnetic field $M$ vs $T$ curves show a significant growth in magnetisation at lower temperatures. If the earlier hypothesis that the magnetic species causing the high $H$ Curie-tail contribution arises from the surface of the particle then it may serve as a volume correction term when analysing catalyst crystallite sizes.

Assuming that the super-paramagnetic saturation magnetisation, $\beta$, arises purely from the core structure and the projected saturation of the Curie-tail arises purely from the shell - we can use the previously calculated average moment to determine the average magnetic moment in the outer-layer, $\mu_{shell} = 25.18(6)$ k$\mu_B$. If we assume that the average particle size from TEM is the "true" particle size and the Langevin fit to the high $T$, $M$ vs $H$ data accurately reflects the size of the core, we can determine the average volume of the outer shell structure, $V_{shell} = 270(10)$ nm$^3$. If we assume the density in the shell is equivalent to the value found from electron microscopy we can use these two values to deduce the average moment per atom, $\mu = 1.17(6)$ $\mu_B$ atom$^{-1}$.

An increase in magnetic moment for nano-sized Ni has previously been reported[155;156;157] for smaller Ni clusters (7 to 30 atoms). The magnetic moment was found to increase to $\mu = 1.80$ $\mu_B$ atom$^{-1}$,[155] suggesting a value of 1.17 is experi-

mentally feasible. The reason for this increase from $\mu_{bulk}$ has been suggested to arise from a variety of parameters including most notably the surface chemistry.[157] The addition of carbon monoxide has been shown to lead to a decrease in the average magnetic moment in Nickel[157] due to a donation of electron density from the Ni surface states to the carbon monoxide $\pi^*$ orbitals.[158] In the systems reported here the ligands have amine and phosphine head groups, strong $\sigma$ donating groups.[159] This character would have the opposite effect to the electron withdrawing carbon monoxide - increasing the electron density in the surface states and hence increasing the value of $\mu$ per atom compared to the non-functionalised material.

If this value of $\mu$ is accurate it would suggest that the outer-shell structure is composed of clusters, consisting of several atoms of ferromagnetically ordered Ni within each cluster but with the clusters experiencing an antiferromagnetic correlation between nearest neighbours. Such a structure would be difficult to observe experimentally due to the atomic resolution, low temperatures and high applied magnetic fields required. However, the analysis of particle size only requires a method for projecting the relative magnetisations from the core and shell structures - not a complete understanding of the physical mechanisms that lead to the structures.

Sample A is consistent with a poly-disperse system of nanoparticles with a magnetic core-shell structure. The core comprises a single ferromagnetic domain with an average magnetic moment 4.45(9) k$\mu_B$ and 20-80% limits to a log-normal distribution at 2.00(2) k$\mu_B$ and 9.9(1) k$\mu_B$ respectively with an associated magnetisation consistent with a super-paramagnetic species experiencing a weak antiferromagnetic correlation between either the core and shell structure or between nearest neighbour particles. The shell comprises micro-clusters of ferromagnetically order Ni, with a weak antiferromagnetic correlation between individual clusters.

An antiferromagnetic correlation between nanoparticles is surprising given the low loading of Ni used ($\approx 1\%$). It is possible that due to the narrow polydispersity of the nanoparticles some colloidal crystal structure has developed with the Fomblin - giving rise to localised clusters of nanoparticles.

### 4.2.5 Blocking temperature analysis.

The method for particle sizing discussed up to this point of the thesis has limited industrial application due to the heavy time demand, requiring data sets taken across a range of the $H-T$ parameter space and several self-consistent correction factors. If these techniques are to be employed in an industrial setting a quicker measurement

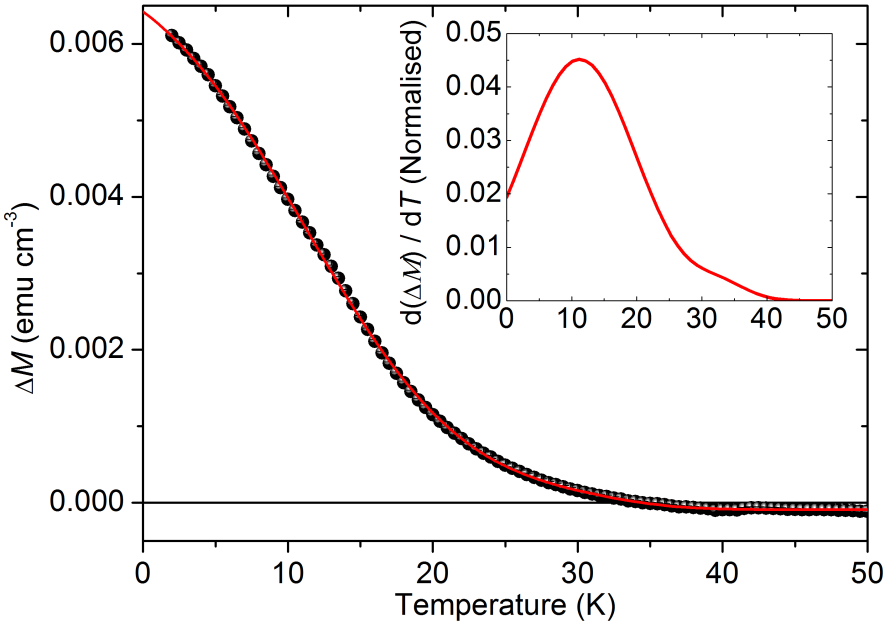


Figure 4.9: Temperature dependence of the difference in magnetisation between the ZFC and FC $M$ vs $T$ data sets for sample A. The rate of change in $\Delta M$ is proportional to the volume of material that "unblocks" within the temperature window. The distribution of $\Delta M$ has been fit by a pair of cumulative Gaussian distributions. These functions have no inherent meaning within the data and serve purely to smooth the data prior to differentiation. Inset - the probabilistic Gaussian distributions used to fit the $\Delta M$ vs $T$ data sets. the relationship between a cumulative and probability distribution is the differential function.

protocol is desirable. As described in section 2.3.1 the difference between the zero-field cooled (ZFC) and field cooled (FC) data sets can be used to determine the distribution in unblocking temperatures[62] - and hence the distribution of particle sizes.

Figure 4.9 demonstrates the variation in the difference between the ZFC and FC data, $\Delta M$, as a function of temperature for sample A using the data previously presented in figure 4.7. As $T$ increases the $\Delta M$ decreases at an increasing rate up-to $\approx 10 - 15\ K$, after which the curve becomes shallower and approaches a constant value (near zero) at $T > 40\ K$. The calculated $\Delta M$ above this point is slightly displaced from zero due to the minor difference in trapped field within

the superconducting magnet after a zero-field cool ($H_{cool}$ = 0 Oe) and a field cool ($H_{cool}$ = 10 kOe). The red line in figure 4.9 is a fit to an arbitrary function, comprising two cumulative Gaussian distributions, in order to smooth the data prior to differentiation.

The inset to figure 4.9 is the associated Gaussian distributions, re-normalized to unity. This function represents the distribution of blocking temperatures, arising when the particles undergo the dynamic transition from the "blocked" hysteretic behaviour to the reversible, paramagnetic behaviour. It is normally assumed that the material has a uni-axial anisotropy,[41] e.g. h.c.p. cobalt, and the dynamic transition follows a Néel relaxation.[160] As a result if we assume an order of magnitude for the time scale per measurement, this relationship can be simplified to a linear conversion between particle volume and blocking temperature, $T_B$, via the materials anisotropy constant, $K$.[161]

Bulk Ni has a relatively small magneto-crystalline anisotropy constant in comparison to other itinerant ferromagnetic materials,[162] $K_{Bulk} = 5,500$ J m$^{-3}$, giving the widest range of particle volumes in the temperature window easily accessible (2 to 400 K). The experimental $T_B$ distribution reaches a maxima at $T \approx 11$ K, and has mean value, $T_B = 14.1(5)$ K. This average ignores any particles with a $T_B$ below 2 K due to the thermal limitations of the $M$ vs $T$ scan.

This mean value of $T_B$ would be consistent with a mean particle volume, $V_{average} = 880(30)$ nm$^3$, and a diameter $d_{average} = 11.9(1)$ nm (assuming $K_{Bulk}$), a sizeable overestimation compared to the TEM and Langevin magnetism analysis.

A discrepancy between the particle size given via this method and TEM is likely due to an increase in particle anisotropy on reduction to the nano-regime.[162] Previous studies have suggested that, due to the increase in surface states, nanoparticles can develop several novel anisotropic structures.[60] The simplest method to study anisotropy is via torque magnetometry of a single crystal[163] - but as we are studying a random ensemble of particles this method is of limited use. Instead, a comparison of nuclear particle volume (via TEM) and the magnetic core volume (from the Langevin method) and the experimental blocking temperature will quantify for the anisotropy constant under different assumptions.

For sample A, using the average particle sizes from TEM, $d_{TEM} = 8.88(7)$ nm, and the Langevin magnetism, $d_{Langevin} = 5.6(1)$ nm, a pair of experimental anisotropy constants can be found, $K_{NanoNuclear} = 13.3(6) \times 10^3$ J m$^{-3}$ when converting from the TEM determined diameter and $K_{NanoMagnetic} = 30(2) \times 10^3$ J m$^{-3}$ from the Langevin determined diameter. These two values reflect the magnitude of the

anisotropy if the core magnetic moment has to overcome the magneto-crystalline energy arising from the particle, as imaged under TEM, or purely the magnetic core structure. It is unclear yet which of these two terms correctly describes the system, however, from a practical view if either a universal value, or the temperature dependence of, $K$ can be determined this $T_B$ method could serve as a rapid particle sizing technique.

Having carried out a full analysis of sample A we need to check for consistency over a small change in volume first before exploring a wider range.

## 4.3 Sample B

An analysis of sample B will demonstrate how consistent the values produced by the Langevin approach are for sizing particles. As sample B was synthesised using the same surfactant system there will be no change in surface chemistry compared to sample A. As such any changes in behaviour will be due to the small change in particle diameter ($\approx 1$ nm).

### 4.3.1 Evidence of single domain ferromagnet behaviour

To begin with it is important to show a similar behaviour to sample A with respect to changes in the $M$ vs $H$ loops as a function of sample temperature. Due to the change in particle volume, super-paramagnetic behaviour will be observed at a lower temperature for sample B; however we should still observe a gradual decrease in coercivity and an increase in the low $T$, high $H$ magnetisation.

Figure 4.10 shows the variation in $M$ vs $H$ behaviour for sample B across the same temperature range as investigated for sample A (figure 4.5). Sample B shows the same super-paramagnetic behaviour as described for sample A, with a decrease in both $M_R$ and $H_C$ with increasing temperature. Comparing the data sets taken at 2 K, sample B appears to have a larger magnetic response than sample A at equivalent applied fields, $M_{B,H=5\text{ kOe}} \approx 0.05$ emu cm$^{-3}$ cf. $M_{A,H=5\text{ kOe}} \approx 0.035$ emu cm$^{-3}$, despite a similar value at high $T$ (at 100 K, $M_{B,H=10\text{ kOe}} \approx 0.025$ emu cm$^{-3}$ cf. $M_{A,H=10\text{ kOe}} \approx 0.022$ emu cm$^{-3}$). The growth in magnetisation at low temperatures for sample A was suggested to be due to the "dead-layer", and a relative increase in the magnetic term arising from the surface would indicate either an increase in the surface state thickness or in the magnetic moment arising from the surface atoms.

The temperature range over which sample B transitions from the blocked

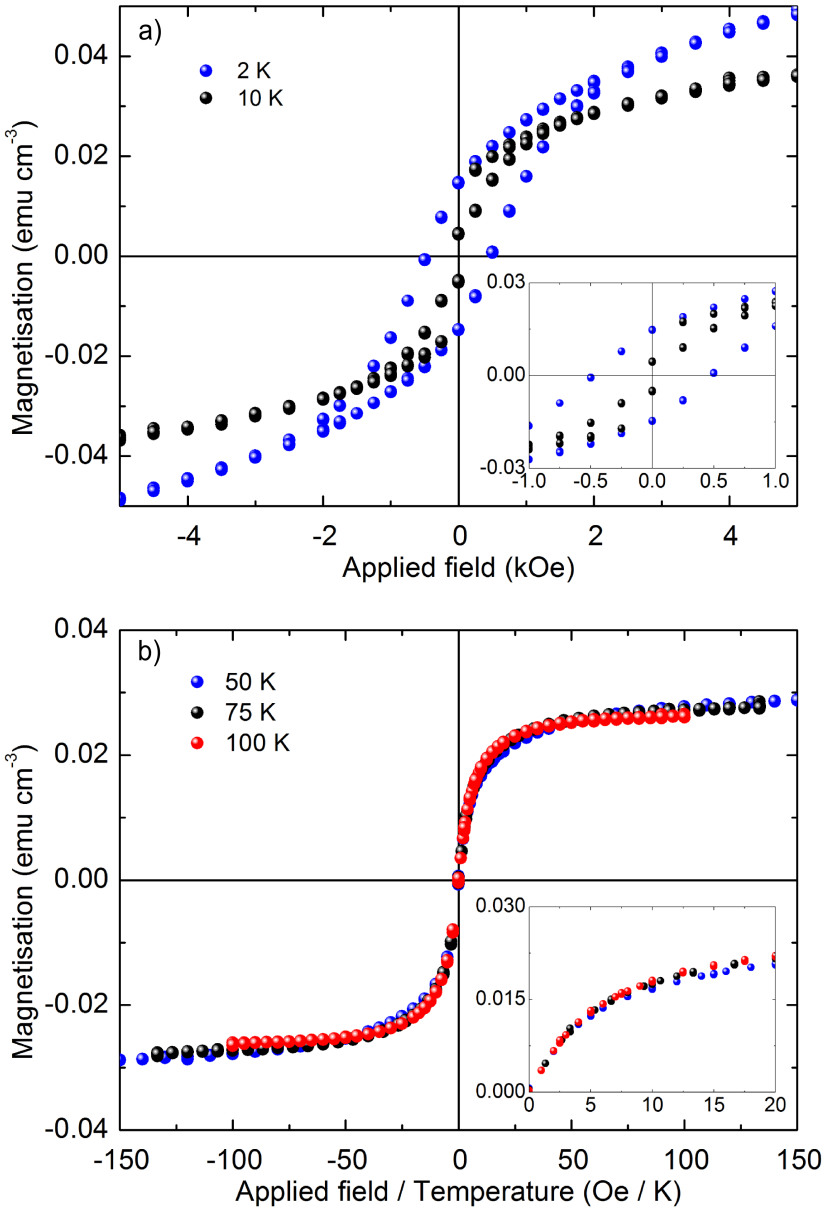


Figure 4.10: $M$ vs $H$ responses for sample B taken at low $T$ (a) and high $T$ (b).

to the super-paramagnetic state appears to occur within a similar range to sample A, with a reversible behaviour observed at $T > 50$ K. The three magnetic curves taken in the high temperature range ($T = 50,\ 75$ and 100 K) all show a reversible magnetisation consistent with a Langevin behaviour but, as with the low $T$ data, $M_S$ is increased ($\approx 0.03$ emu cm$^{-3}$) in comparison to sample A. The three high $T$ curves show a similar diamagnetic term at high $H$ as reported for sample A, $\chi = -3(1) \times 10^{-7}$ emu cm$^{-3}$ Oe$^{-1}$, with the Fomblin grease the dominant source of this term.

The inset to figure 4.10 demonstrates the possibility of a universal magnetic behaviour across multiple temperatures for sample B. As was observed for sample A, the higher $T$ curves at 75 and 100 K appear to have a shared behaviour but the data taken at 50 K differs from a universal $\frac{M}{M_S}$ vs $\frac{H}{T}$ behaviour. Hence the $M$ vs $T$ analysis needs to be repeated in order to determine the Weiss temperature correction factor.

The $M$ vs $H$ analysis again shows a marked increase in the magnetisation as low $T$ and high $H$ so the analysis will again begin with an attempt to understand the magnitude of this contribution compared to the "super-paramagnetic" material and quantify any correlations.

### 4.3.2 Curie-tail behaviour at high $H$

Figure 4.11 a) shows the $M$ vs $T$ behaviour of sample B at high applied fields, (10 and 50 kOe). As seen for sample A in figure 4.6 the core of the nano-particle appears to have reached near saturation by 10 kOe, with the low $T$ region difference caused by the smaller paramagnetic moments previously assigned to the outer-shell structure. The high $H$, $\frac{1}{\chi}$ behaviour has also been plotted in figure 4.11 b). As was the case for sample A, the low $T$ data shows a linear behaviour for the highest applied field ($H = 50$ kOe) with a projected $T$ intersect below zero, again requiring a Weiss temperature term to be included in the analysis.

Once again the data has been fit with equation 4.3 in order to check the low $T$ Curie-Weiss behaviour. The fit was carried out the data collected at both applied fields simultaneously with shared values for all free parameters. The best fit parameters to this model are given in table 4.4.

The model once again appears to accurately reproduce the magnetisation, with a value of $\beta$ close to the saturation magnetisation observed in figure 4.10, and a $\chi^2_{red} \approx 1$. Interestingly the values of $\theta$, $\mu$ and $\alpha$ are close to those found for sample

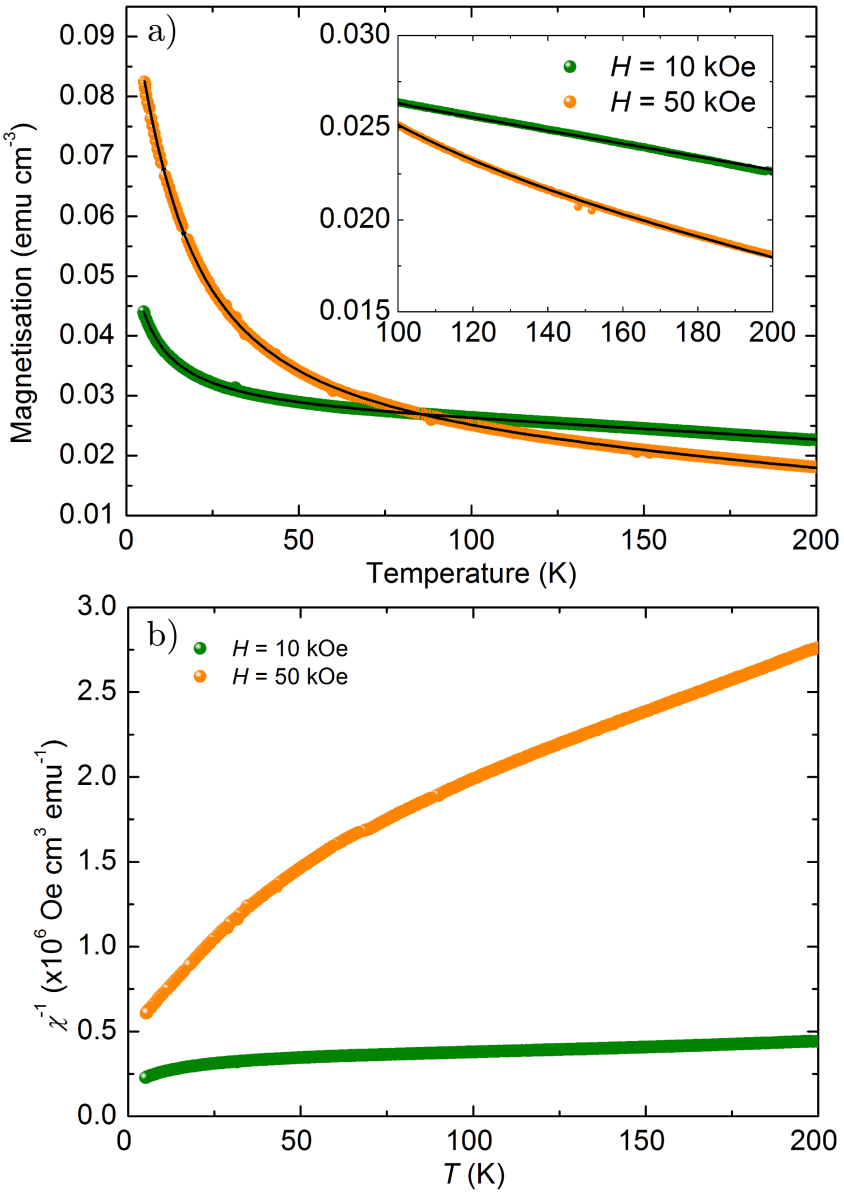


Figure 4.11: $M$ vs $T$ curves for sample B taken at $H$ = 10 (green), and 50 (orange) kOe with associated fits to equation 4.3. The curves show a clear paramagnetic response at low $T$ on top of a weakly $H$ dependent magnetic term at higher $T$. b) The high $H$ magnetic susceptibility as a function of $T$.

| Parameter | Value | Units |
|---|---|---|
| $\mu$ | 8.44(3) | $\mu_B$ |
| $M_S$ | 0.1037(3) | emu cm$^{-3}$ |
| $\theta$ | -5.65(2) | K |
| $\alpha$ | $5.27(2) \times 10^{-5}$ | K$^{-1.5}$ |
| $\beta$ | $28.09(1) \times 10^{-3}$ | emu cm$^{-3}$ |
| $b$ | $-2.137(3) \times 10^{-7}$ | emu cm$^{-3}$ Oe$^{-1}$ |
| $\chi^2_{red}$ | 1.16 | n/a |

Table 4.4: Best fit parameters of the model described in equation 4.3 to the high $H$, $M$ vs $T$ data sets reported in figure 4.11. The field independent nature of the spin-wave coefficients $\alpha$ and $\beta$ imply that the core ferromagnetic moments fitted at high $T$ are saturated in all cases. The diamagnetic term, $b$, is consistent with the measured susceptibility of Fomblin grease.

A - suggesting that any volume dependence is small. The Weiss temperature term, $\theta$, is again negative suggesting the core, super-paramagnetic domains experience an antiferromagnetic correlation between neighbouring nano-particles.

### 4.3.3 Corrected Langevin function analysis

With the high $H$ data analysed the next stage is to identify the temperature region in which the magnetic response is reversible and if the core $\theta$ value is comparable to the value found for sample A.

Figure 4.12 shows the magnetic behaviour of sample B as a function of temperature, after both zero-field cooling and field cooling (following the same protocol as outlined for sample A, $H_{Measure}$ = 100 Oe, $H_{FC}$ = 10 kOe). As with sample A, sample B demonstrates a marked difference between the ZFC and FC magnetic response at low temperatures, with $M_{ZFC}$ gradually increasing and $M_{FC}$ decreasing as temperature increases until the two share a magnetic response. Sample B has a slight offset between $M_{ZFC}$ and $M_{FC}$ in the high temperature regime, $T > 40$ K, due to a difference in trapped field from the application of $H_{FC}$. Apart from this the behaviour is qualitatively the same as observed for sample A (see figure 4.7).

The best fit to the high $T$ response is displayed on figure 4.12 as the dashed black line and represents a fit to a Langevin function with average magnetic moment, $\mu$, with an added Weiss temperature term, $\theta$. For the fit the magnetic saturation and diamagnetic background were set as the values found in the high $H$ Curie-tail analysis and the best fit parameters to this model are given in table 4.5. This model is in comparison to the simpler Curie law, $\chi_{red}$ = 13.81, again demonstrating the

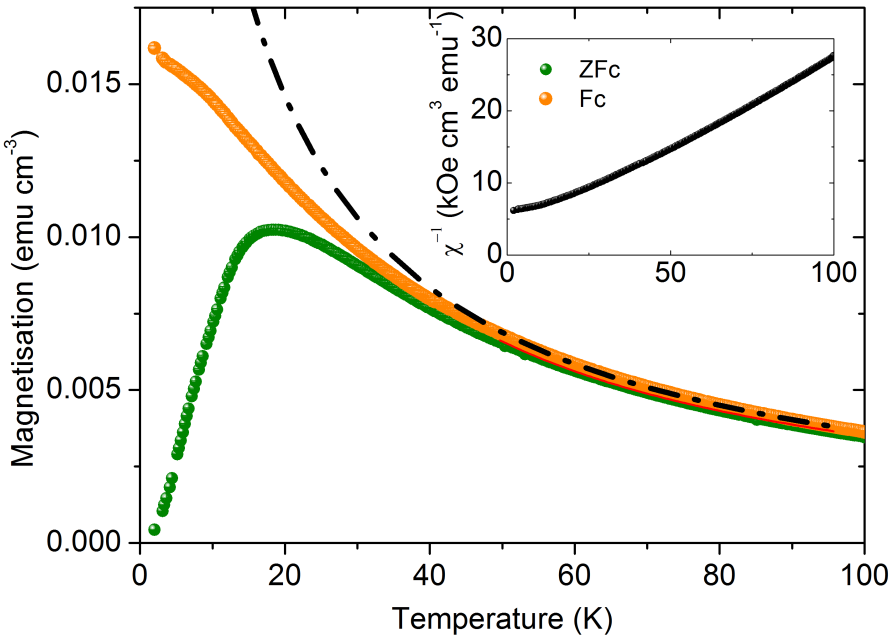


Figure 4.12: $M$ vs $T$ behaviour of sample B taken at $H = 100$ Oe in both ZFC (green, $H_{cool} = 0$ Oe) and FC (orange, $H_{cool} = 10$ kOe) conditions. At $T$ greater than $\approx 40$ K the cooling field has little effect on the $M$ vs $T$ response. The black dashed line is the fit to the high $T$ data, $T > 50$ K, of the Curie-Weiss law with a diamagnetic background. Inset - the $\frac{1}{\chi}$ behaviour of the FC data set corrected for the Fomblin background.

| Parameter | Weiss-corrected Langevin | Units |
|---|---|---|
| $\mu$ | 5.81(2) | k$\mu_B$ |
| $\theta$ | -3.8(2)(1) | K |
| $\chi^2_{red}$ | 0.86 | n/a |

Table 4.5: Best fit parameters for the Langevin model corrected by a Weiss constant to the high $T$, $M$ vs $T$ response of sample B at $H = 100$ Oe.

necessity of the Weiss temperature term.

The parameters of best fit for sample B are very similar to those for sample A, with a comparable value for the Weiss temperature and a decrease in the average magnetic moment, $\mu$, as expected for a decrease in average particle size. As with sample A, the value of $\theta$ suggests that these magnetic species experience an antiferromagnetic correlation between neighbouring nanoparticles - previously suggested to arise from either inter-particle dipole-dipole or RKKY interactions. With the lack of a conducting media an RKKY interaction is highly unlikely, suggesting the dipole-dipole interaction is more likely. Due to the low loading of Ni used in the magnetisation study samples, dipole-dipole interactions should be weak, suggesting that some extent of colloidal crystal templating has occurred. The self-assembly would decrease inter-particle distance, hence increasing the strength of the dipole-dipole interaction.

Now that the thermal correction term has been determined the moment per particle can again be deduced using the corrected Langevin method. Figure 4.13 is the $M$ vs $H$ behaviour of sample B at 75 and 100 K and the fit of the Langevin function corrected by the Weiss temperature term found during the $M$ vs $T$ analysis. As with sample A, both a single and dual Langevin model were fit to the data sets. In both cases the fits were carried out on the 75 and 100 K data sets simultaneously with shared values of $\mu$ and temperature dependent values of $M_S$. The Langevin function is corrected by a Weiss temperature, $\theta = -3.8$ K and, as with the $M$ vs $T$ analysis, the diamagnetic correction, $b$, found during the high $H$, $M$ vs $T$ analysis. The best fit parameters are listed in table 4.6.

The dual Langevin model gives a superior fit to the $M$ vs $H$ data, with a $\chi^2_{red}$ closer to unity and a closer reproduction of the magnetisation in the range 1 to 5 kOe (the same region the single Langevin model struggled to reproduce for sample A). Making the same assumption of a log normal particle size distribution and hence that $\mu_1$ and $\mu_2$ represent the continuous probability distribution at 80 and 20% of the maxima (respectively) a mean moment per particle can be deduced,

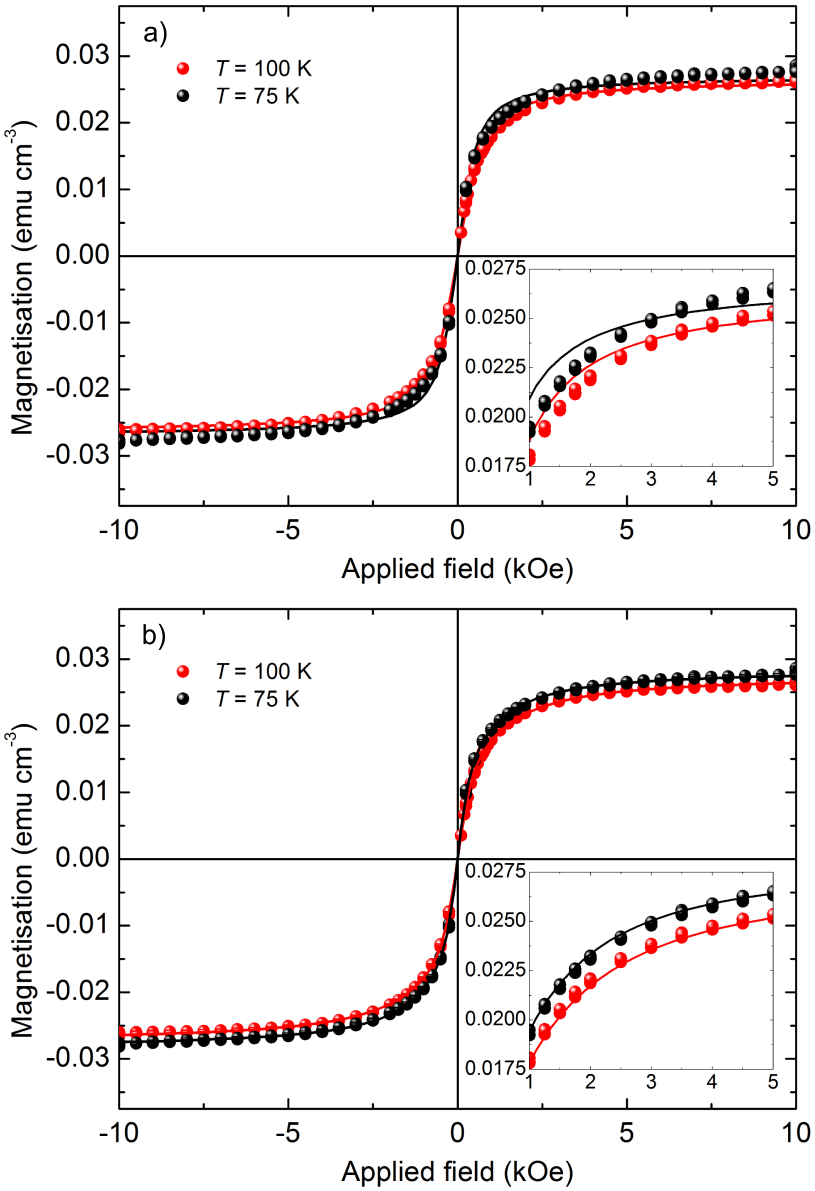


Figure 4.13: $M$ vs $H$ response of sample B taken at 75 (black) and 100 (red) K and the associated fits to a single Langevin model (figure a) and the proposed dual Langevin model (figure b). Inset - a closer examination of the 10 to 50 kOe region of the $M$ vs $H$ response in which the single Langevin model fails to accurately describe the magnetisation cf. the dual Langevin model.

| Parameter | Single Langevin model | Dual Langevin model | Units |
|---|---|---|---|
| $\mu_1$ | 5.48(5) | 8.7(1) | k$\mu_B$ |
| $\mu_2$ | n/a | 1.73(4) | k$\mu_B$ |
| $M_{S1(75\ \mathrm{K})}$ | $26.49(9) \times 10^{-3}$ | $17.7(2) \times 10^{-3}$ | emu cm$^{-3}$ |
| $M_{S2(75\ \mathrm{K})}$ | n/a | $9.9(2) \times 10^{-3}$ | emu cm$^{-3}$ |
| $M_{S1(100\ \mathrm{K})}$ | $26.97(9) \times 10^{-3}$ | $17.0(3) \times 10^{-3}$ | emu cm$^{-3}$ |
| $M_{S2(100\ \mathrm{K})}$ | n/a | $11.6(2) \times 10^{-3}$ | emu cm$^{-3}$ |
| $\chi^2_{red}$ | 17.75 | 1.05 | |

Table 4.6: Best fit parameters for the Single and Dual Langevin $M$ vs $H$ response for sample B (see figure 4.13).

$\mu_{average} = 3.88(9)$ k$\mu_B$.

### 4.3.4 Magnetic moment to volume conversions

Following the same procedure for sample A (using the bulk value of $\mu_B$ atom$^{-1}$ and the electron diffraction value of $\rho$) these magnetic moment terms can be converted into particle sizes, resulting in a mean particle size $d_{mean} = 5.3(1)$ nm with 20 - 80% limits at $d_{20\%} = 4.2(1)$ nm and $d_{80\%} = 7.2(1)$ nm. Comparing these values to those observed in TEM, $d_{TEM} = 7.69(6)$ nm with a range over 6 to 9 nm, there is a clear underestimation of the particle size by $\approx 2$ nm.

The surface contribution is analysed as for sample A, assuming that at high $H$ the core acts as a saturated single domain and the shell has a Curie-corrected Langevin behaviour. Using the values obtained from modelling the high $H$ Curie-tail earlier ($\beta$ and $M_S$) each nanoparticle shell would have an average total magnetisation of 14(3) k$\mu_B$. Comparing the TEM and Langevin average particle sizes the average volume of the outer shell can be calculated, $V_{Shell} = 160(10)$ nm, giving an estimate for the moment per atom within the shell, $\mu = 1.16(6)$ $\mu_B$ atom$^{-1}$.

Analysis of sample B in this way serves to reinforce the conclusions drawn from sample A - with a value of the average moment per atom in the surface state consistent between the similar sized samples. The increased value from bulk is again likely due to the $\sigma$-donating character of the ligands but the particle size has not effected the value, which is promising for a universal conversion value.

### 4.3.5 Blocking temperature analysis

Aside from an average particle size, the particle size distribution may also be mapped via the ZFC/ FC analysis (as demonstrated for sample A in figure 4.9). Figure 4.14 is

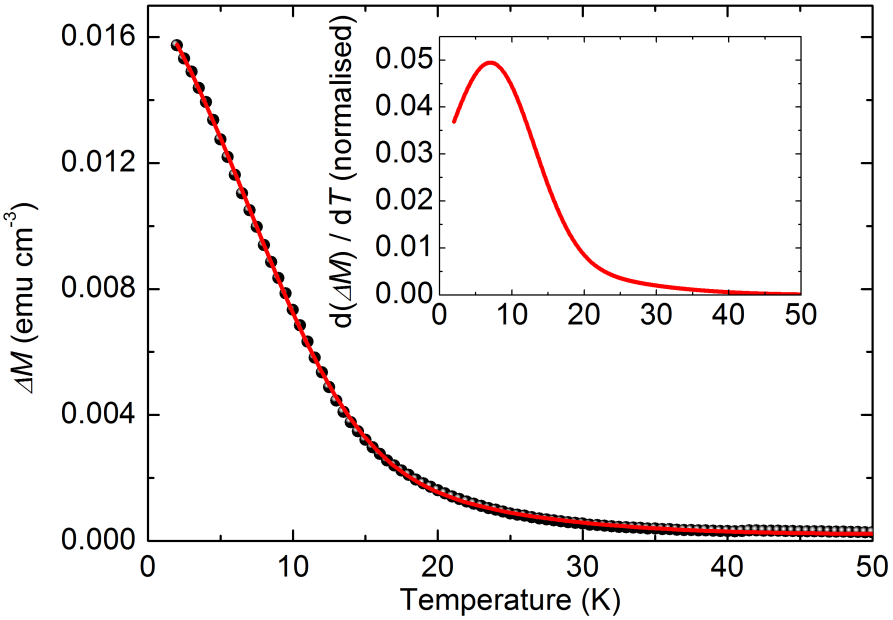


Figure 4.14: The temperature dependence of the difference in magnetisation between $M_{ZFC}$ and $M_{FC}$ as a function of $T$ for sample B. The distribution of $\Delta M$ has been fit by a pair of cumulative Gaussian distributions. Inset - the Gaussian distributions used to fit $\Delta M$ vs $T$ data sets.

the difference between the ZFC and FC data sets, $\Delta M$, as a function of temperature for sample B (using the data sets presented in figure 4.12). As is to be expected, increasing the temperature causes a gradual decrease in $\Delta M$, before tending to a constant value at $T$ greater than $\approx 40$ K. The distribution of $\Delta M$ was fitted with an arbitrary function in order to smooth the data prior to differentiation, in this case using a pair of cumulative Gaussian functions, shown as the red line in the main figure.

The inset to figure 4.14 is the differential of the cumulative distribution fit to the data and represent the distribution of the temperature derivative of $\Delta M$ as a function of temperature - or put simply the blocking temperature distribution. Using this distribution, the mean value of $T_B$ (excluding data below 2 K) is 9.8(4) K. A mean value was taken in order to make direct comparisons to the TEM and Langevin particle sizes but has required the assumption that data below 2 K is irrelevant - leading to a possible overestimation of the average $T_B$ and hence in $K$ during the

| Sample | $n_{Ni}$ (mmol) | $n_{Oleyl\ amine}$ (mmol) | $n_{Trioctyl\ phosphine}$ (mmol) |
|---|---|---|---|
| C | 1 | 21 | 0 |
| D | 2 | 21 | 3 |

Table 4.7: Synthesis parameters for the two nanoparticle preparations, C and D.

next step of the analysis.

For sample B, using the average particle sizes from TEM, $d_{TEM} = 7.69(6)$ nm, and the Langevin magnetism, $d_{Langevin} = 5.3(1)$ nm, a pair of experimental anisotropy constants can be found, $K_{NanoNuclear} = 14.2(7) \times 10^3$ J m$^{-3}$ and $K_{NanoMagnetic} = 28(2) \times 10^3$ J m$^{-3}$. These two values reflect the magnitude of the anisotropy if the core magnetic moment has to overcome the magneto-crystalline energy arising from the total nano-particle, including the outer-shell, and purely the core structure. Interestingly both of these values are in close agreement with those found from sample A ($K_{NanoNuclear} = 13.3(6) \times 10^3$ J m$^{-3}$ and $K_{NanoMagnetic} = 30(2) \times 10^3$ J m$^{-3}$) suggesting that this thermal magneto approach may provide a new reliable technique if the catalytic ferromagnetic deposits are not strongly affected by the change in surface chemistry caused by adding a support material.[164]

The limitation to this work at present is that only 2 samples of similar particle size have been investigated. In order to broaden the scope, this analysis will be repeated (for a set of larger particles) focusing on the highest $T_B$ accessible within our experimental limits with a slight change in measurement protocol aimed at decreasing the time required for data collection.

## 4.4 Synthesis of sample C & D; variation of particle size via reagent control

### 4.4.1 Synthesis

Having already demonstrated that a variation in the synthesis temperature gives a small change in average particle size ($\approx 1$ nm) an alternative variable is required to give a wider range of particle sizes. Changes to the Ni($acac_2$)/ surfactant mixture will alter the micellar system - creating a change in average particle size. With this in mind, the synthesis described in section 3.2.1 was repeated, but the number of moles, $n$, altered as described in table 4.7. This change in reaction conditions led to the synthesis of two further samples, C and D, with larger average particle sizes.

### 4.4.2 TEM analysis

TEM images of the two sets of NP samples were taken via the same method as detailed in section 4.1.2 using the Technai F20 TEM operating at 200 kV. Figure 4.15 shows typical TEM images for the two samples and the associated particle size histograms acquired following the same method as outlined in section 4.1.2.

TEM analysis demonstrates that both changes to the reaction conditions have led to a larger average particle size, with average particle diameters of 23.0(4) and 12.19(7) nm, for samples C and D respectively. Interestingly sample C appears to have lost the tight particle size distribution observed for samples A, B and now D - this is evident both in the particle size histogram and in the loss of the well ordered colloidal crystal packing in the TEM image. These samples give a much broader range of particle sizes to calibrate the magnetic granulometry technique prior to applying the method to catalysts - with sample C being of particular interest as it pushes the limits of the single domain assumption (theoretically applicable up to $\approx 40$ nm)[38;39] and demonstrate the effect of a large polydispersity on the magnetic properties.

## 4.5 Magnetization studies of Sample C

DC magnetisation measurements were carried out following the same procedure as outlined for samples A and B in section 4.2 using a Quantum Design MPMS SQUID magnetometer working in DC mode with the NP materials suspended in the fluorinated grease. For both sample $M$ vs $H$ loops were taken at 200 K with $H_{Max} = 50$ kOe for the Langevin method, and $M$ vs $T$ loops were taken at both high and low applied fields with the data analysed via the "three-term" model and blocking temperature approaches, respectively.

### 4.5.1 Langevin analysis

Based on the analysis carried out on samples A and B the analysis will be simplified for sample C. This is achieved by assuming from the outset that the nanoparticles are single domain systems and by carrying out the Langevin $M$ vs $H$ analysis at a higher temperature ($T = 200$ K). An increase in the temperature for the Langevin analysis means that the necessity of the $\theta$ correction is reduced (as $T + \theta$ tends to $T$ at high temperatures) so the low $H$, $M$ vs $T$ analysis can be excluded. This serves the purpose of both decreasing the quantity of data required and means that for

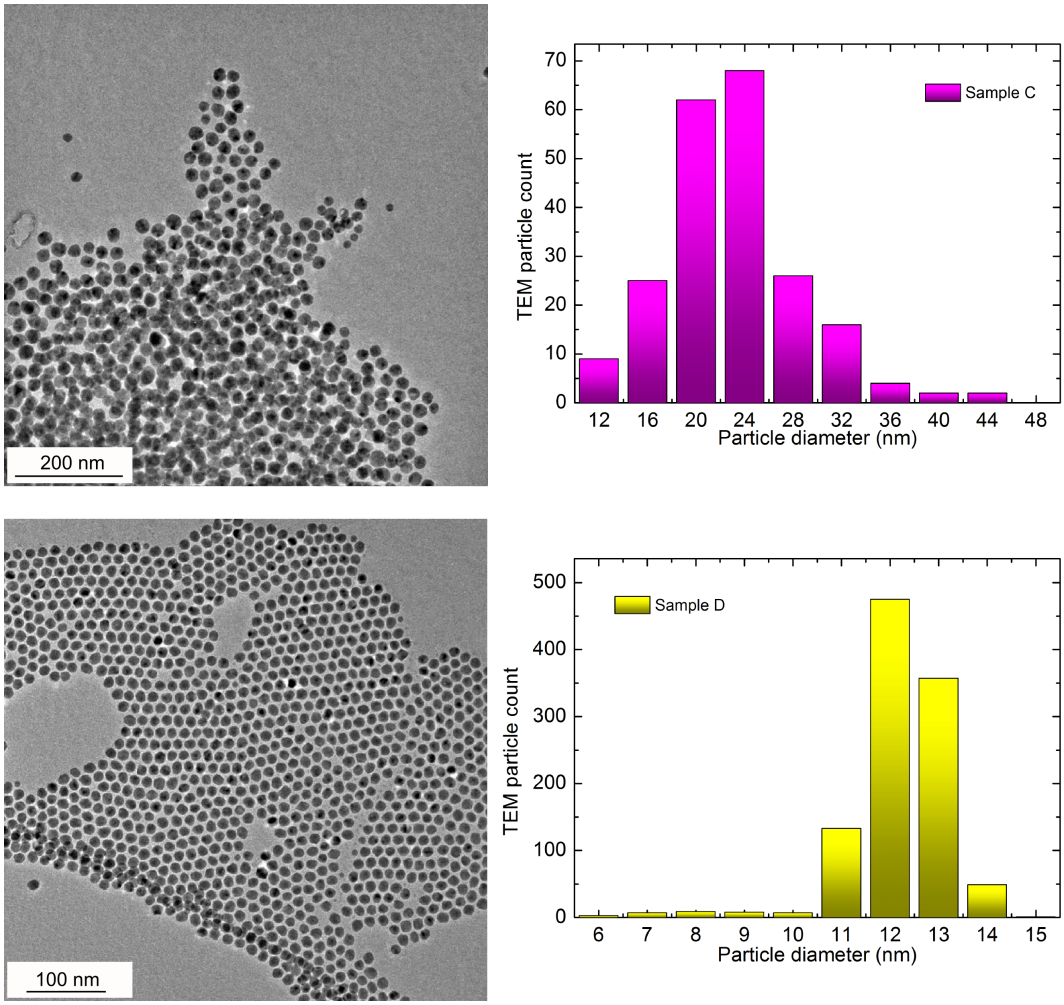


Figure 4.15: A typical TEM image and associated particle size histogram for sample C (images a and b) and D (images c and d).

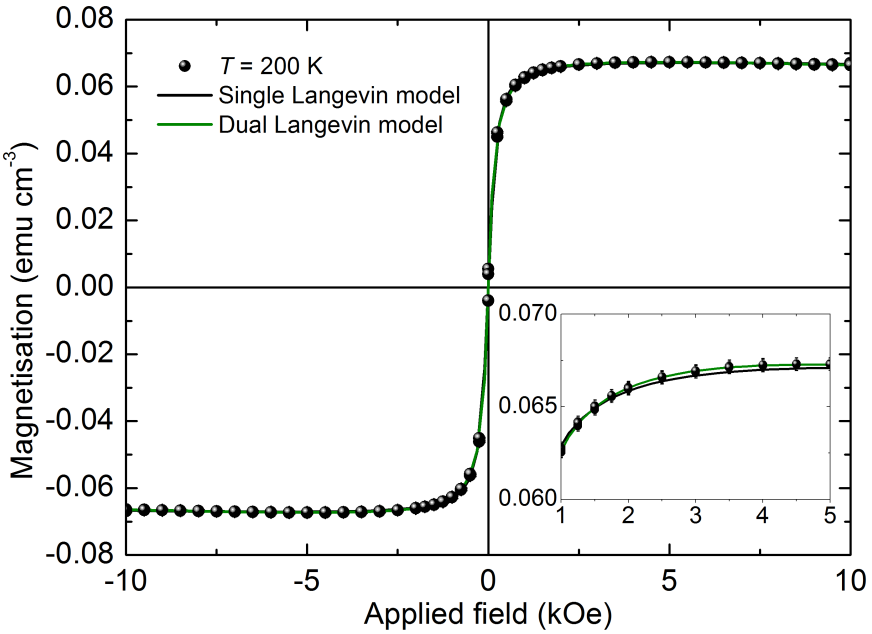


Figure 4.16: $M$ vs $H$ data set for sample C taken at $T = 200$ K. The data has been fit by both a Single and Dual Langevin function model (black and green lines respectively) and the parameters of these fits are listed in table 4.8. Inset - the $H$ region 0.5 to 5 kOe for sample C.

samples that have high blocking temperatures only a small temperature range in which the magnetisation is reversible is required.

Figure 4.16 shows the $M$ vs $H$ data taken for sample C at 200 K. The measured magnetisation was reversible at applied fields greater than 500 Oe with a small residual magnetisation, $M_R$, (magnetisation at $H = 0$ Oe, post saturation). The low field hysteretic behaviour and small $M_R$ indicate that some of the particles are still within the "blocked" state - the temperature is too low for them to behave as paramagnetic material. This may cause a systematic error in the application of the Langevin approach - as it assumes the material acts as a simple paramagnet with increased magnetic moment.

The $M$ vs $H$ data taken at $T = 200$ K, shown in figure 4.16, was fit with both the Single and dual Langevin models for comparison (shown as the black and green lines, respectively) and the best fit parameters are summarised in table 4.8.

| Parameter | Single Langevin | Dual Langevin | Units |
|---|---|---|---|
| $\mu_1$ | 33.4(2) | 98(3) | k$\mu_B$ |
| $\mu_2$ | n/a | 17.0(2) | k$\mu_B$ |
| $M_{S1}$ | $69.36(7) \times 10^{-3}$ | $35.12(2) \times 10^{-3}$ | emu cm$^{-3}$ |
| $M_{S2}$ | n/a | $35.12(2) \times 10^{-3}$ | emu cm$^{-3}$ |
| $b$ | $-2.0(1) \times 10^{-7}$ | $-3.05(6) \times 10^{-7}$ | emu cm$^{-3}$ Oe$^{-1}$ |
| $\chi^2_{red}$ | 1.32 | 0.31 | n/a |

Table 4.8: Best fit parameters for the Single and dual Langevin models to the $T =$ 200 K data sets shown in figure 4.16.

Interestingly, both the Single Langevin and dual Langevin models give a reasonable reproduction of the data, with the inset to figure 4.16 demonstrating a close agreement between model and data in the $H$ region normally poorly described by the single Langevin model. Similarly, the values of $\chi^2_{red}$ for the single Langevin model is greatly reduced for sample C compared to samples A and B. The dual Langevin model does give a better reproduction of the data, however, the improvement in the fit is too small to demand an increase from 3 to 5 free parameters. As a result in this case we will use the value of $\mu$ from the single Langevin model as the average moment per particle.

The value of $\mu_{average}$ has increased significantly when compared to samples A and B, 33.4(2) k$\mu_B$ cf. 4.45(7) and 3.88(9) k$\mu_B$, respectively, suggesting that the super-paramagnetic signal is scaling with increasing particle size - as expected. However, using the value of $\rho$ found earlier and assuming 0.61 $\mu_B$ atom$^{-1}$ a particle with 33.4(2) k$\mu_B$ would have a diameter of 11.0(2) nm - which compared to the average particle size found in TEM, $d_{TEM} = 23.0(4)$, is a larger reduction then for earlier samples, both in absolute values (12 nm cf. $\approx$ 2 nm) and in relative terms ($\approx 50\%$ of $d_{TEM}$ for sample C cf. $\approx 30\%$).

As the particle diameter has increased there appears to be an increasing discrepancy between the $d_{TEM}$ and $d_{Langevin}$ values. This increasing discrepancy suggests a growing contribution from the magnetic "shell", as a result of both an increased surface area per particle and a decrease in the energy preference for a single domain particle.

### 4.5.2 Curie behaviour at high $H$

Figure 4.17 is the $M$ vs $T$ data taken at high applied fields, $H = 50$ (orange), and 20 (green) kOe, in the temperature range 5 to 200 K. As with the previous high $H$

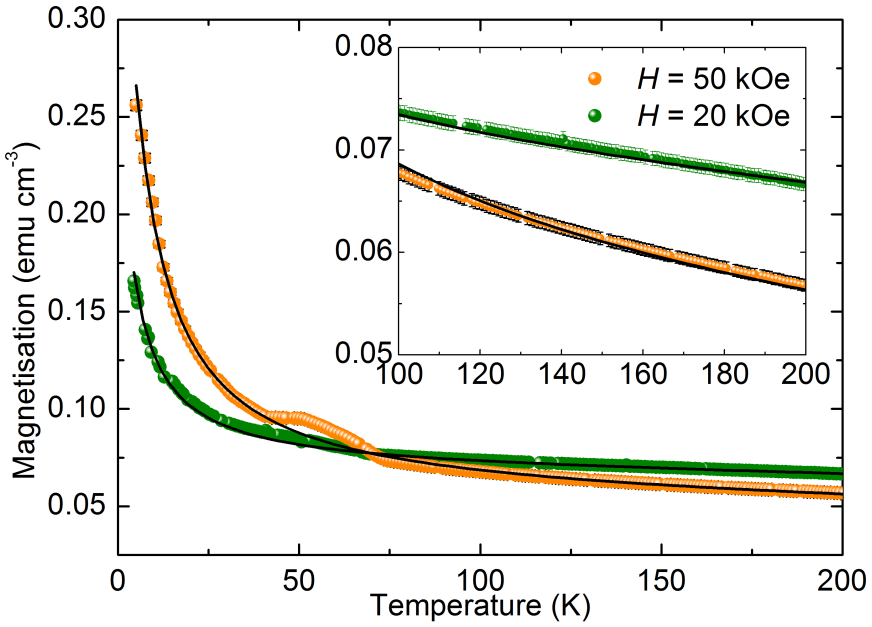


Figure 4.17: The $M$ vs $T$ behaviour of sample C taken at $H = 20$ (green) and 50 kOe (orange). At 40 to 70 K there is a clear feature in the 50 kOe magnetisation which arises from trapped $O_2$ as it passes from antiferromagnetic to paramagnetic.[165] The lines represent the best fit to the data of the "three term" model and the parameters are summarised in table 4.9.

| Parameter | Value | Units |
|---|---|---|
| $\mu$ | 3.6(2) | $\mu_B$ |
| $M_S$ | 0.49(3) | emu cm$^{-3}$ |
| $\theta$ | -3.1(1) | K |
| $\alpha$ | $1.98(6) \times 10^{-5}$ | K$^{-1.5}$ |
| $\beta$ | $78.2(1) \times 10^{-3}$ | emu cm$^{-3}$ |
| $b$ | $-5.45(3) \times 10^{-7}$ | emu cm$^{-3}$ Oe$^{-1}$ |
| $\chi^2_{red}$ | 1.13 | n/a |

Table 4.9: Best fit parameters for the three term model to the $M$ vs $T$ data sets reported in figure 4.17.

studies the magnetisation increases rapidly in a Curie behaviour as the temperature is reduced, suggesting the presence of a paramagnetic contribution from a magnetic moment on the order of 10 $\mu_B$. However, unlike in previous measurements each of the $M$ vs $T$ data sets show a small bump at $\approx$ 40 to 60 K. This feature is commonly attributed to trapped molecular oxygen,[165] arising during the transition from antiferromagnetic to paramagnetic, and despite attempts to flush the sample with inert gas it was never fully removed - suggesting a small physisorption to either the nanoparticles or Fomblin grease. As a result any analysis will be carried out using the data excluding the region 40 to 60 K in each data set.

In order to quantify the magnetic contribution arising from the surface species the $M$ vs $T$ data sets were fit with the "three term" model described earlier in section 4.2.2. The fit was carried out on both data sets (50, and 20 kOe) simultaneously with all parameters shared. The solid lines on figure 4.17 represent the calculated best fits of the model and the best fit parameters are summarised in table 4.9.

The three term model appear to closely reproduce the $M$ vs $T$ data taken for sample C (ignoring the oxygen feature), with a $\chi^2_{red}$ close to unity and both magnetisations ($H$ = 20, and 50 kOe) lying on their predicted curves. The best fit parameters likewise are on the same scale as for samples A and B, with a slight reduction in $\mu$ and $\theta$. The magnitude of the diamagnetic background, $b$, is increased compared to the Langevin function fit but this is because at high $T$ the small moment paramagnetic term is linear adding a small positive contribution to the background. Importantly, however, the ratio between the magnetic saturation of the shell, micro paramagnetic domains and the core, super-paramagnetic signal is still relatively large - and should serve as the necessary correction term to the Langevin analysed particle size.

Assuming that the parameters $M_S$ and $\beta$ are the magnetic saturation terms

of the shell and core, respectively, it is possible to project the average moment per shell, $\mu_{shell}$ = 210 (10) k$\mu_B$. This represents a remarkable increase in the moment arising from the shell, but this is unsurprising given both the greatly increased surface contribution of the larger diameter particle and the underestimation of the particle size from the Langevin approach. However, the "three term" model did suggest that the average moment of each of these micro-domains is reduced when compared to smaller particles - suggesting that either the average moment per atom is reduced or the number of atoms per domain has decreased. So, by comparing the average particle size from TEM, $d_{TEM}$ = 23.0(4) nm, with the size from the Langevin approach, $d_{Lang}$ = 11.0(6) nm, we can calculate the average shell volume, $V_{Shell} = 5.7(4) \times 10^3$ nm$^3$, and hence convert this to an average moment per atom, $\mu = 0.47(4)\mu_B$.

A value of $\mu_{shell} = 0.47(4)\ \mu_B$ atom$^{-1}$ is decreased from the values reported for sample A and B but is in keeping with the reduced value of $\mu$ suggested by the three term model. The increased value of $\mu_{Shell}$ compared to the bulk value was earlier linked to the $\sigma$-donating effect of the ligands. As the particle radius is increased the average distance to the surface states increases and so surface contributions are expected to decrease. The result of this is that we should not be surprised to see a decrease in the average shell moment as particle size increases. This effect may in fact explain the reason for the large range of values reported for the magnetic moment at the surface (ranging from 0.2 to 2 $\mu_B$ depending on sample thickness and surface chemistry).[155;146;157;166]

Conversely, as the aim of this work is to produce a method of sizing industrial catalysts, if we had simply assumed $\mu_{shell} = \mu_{bulk} = 0.61\ \mu_B$ atom$^{-1}$ then the particle size would have been estimated at $d$ = 21(1) nm. This value of $d$ undersizes by $\approx$ 2 nm which is a marked improvement when compared to the errors on Scherrer analysis and gas adsorption isotherms (on the order of 5 nm).

## 4.6 Magnetisation studies of sample D

Following the same protocols for sample C we will now apply the same magnetic analysis to sample D, which has an average particle size from TEM of $d_{TEM} \approx 12$ nm. This sample has a particle size mid way through the range already described, and hence test our current size dependent hypotheses.

| Parameter | Single Langevin | Dual Langevin | Units |
|---|---|---|---|
| $\mu_1$ | 11.7(1) | 19.2(7) | k$\mu_B$ |
| $\mu_2$ | n/a | 4.7(2) | k$\mu_B$ |
| $M_{S1}$ | $8.06(4) \times 10^{-3}$ | $4.64(3) \times 10^{-3}$ | emu cm$^{-3}$ |
| $M_{S2}$ | n/a | $4.17(3) \times 10^{-3}$ | emu cm$^{-3}$ |
| $b$ | $-3.75(5) \times 10^{-7}$ | $-4.49(5) \times 10^{-7}$ | emu cm$^{-3}$ Oe$^{-1}$ |
| $\chi^2_{red}$ | 7.90 | 1.37 n/a | |

Table 4.10: Best fit parameters for the Single and dual Langevin models to the $T =$ 200 K data sets shown in figure 4.18.

### 4.6.1 Langevin analysis

Figure 4.18 shows the $M$ vs $H$ data taken for sample D at 200 K. The magnetisation is reversible with applied field at this temperature with a negligible remanent magnetisation indicating that the material is above its blocking temperature and the super-paramagnetic assumption is applicable. As with sample C, the $M$ vs $H$ data has been taken at a higher temperature, 200 K, so that the $\theta$ correction term becomes negligible and the low $H$, $M$ vs $T$ analysis can be removed - hence increasing the speed of analysis, a key issue for industrial application. Inspection of figure 4.18 the high $H$ behaviour appears to have a larger diamagnetic signal than samples A to C - however, the diamagnetic contribution is actually the same and it is the scale of the super-paramagnetic contribution that is decreased due to a lower loading of nanoparticles. As previously stated measuring the actual loading of Ni within the Fomblin grease is impractical due to safety reasons but the fact we can observe the super-paramagnetic behaviour at lower loading of Ni does highlight the extreme sensitivity of the SQUID magnetometer to low Ni content.

The $M$ vs $H$ data was fit with both the Single and dual Langevin models, shown as the black and green lines on figure 4.18 respectively, and the best fit parameters are summarised in table 4.10. As with sample A and B it is the dual Langevin model that gives the superior fit (a $\chi^2_{red} = 1.37$ cf. 7.90 for the single Langevin model) and as expected from the shape of the response the value of $M_S$ is reduced compared to previous samples but the diamagnetic susceptibility, $b$, is comparable.

The values of $\mu$ found using the dual Langevin model show a slight increase when compared to samples A and B, but are smaller than sample C. Likewise, assuming the 20 - 80% behaviour as earlier predicts a value of $\mu_{average} = 9.5(3)$ k$\mu_B$, again an increase compared to samples A and B but smaller than sample C. Following

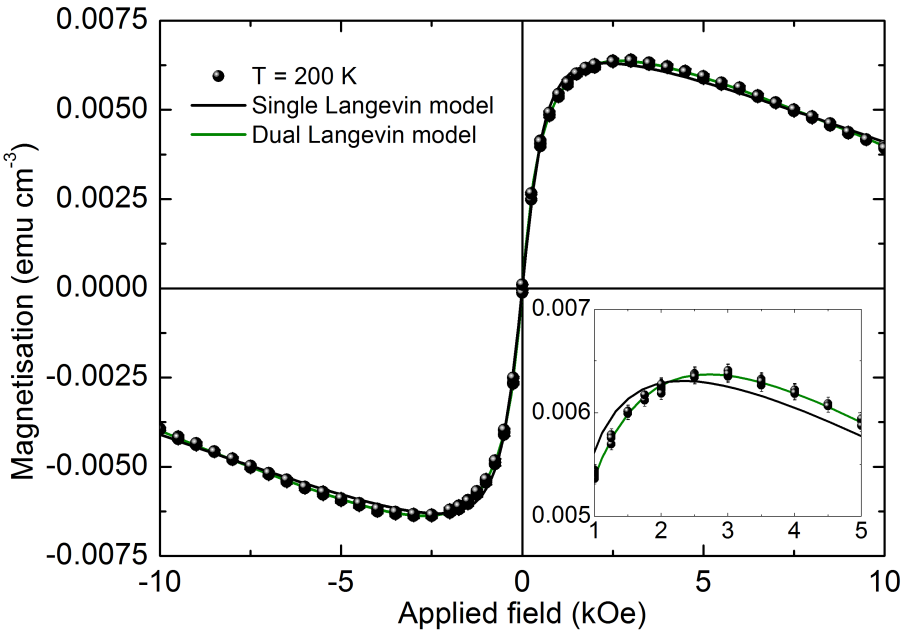


Figure 4.18: $M$ vs $H$ data set for sample D taken at $T = 200$ K. The data has been fit by both a Single and Dual Langevin function model (black and green lines respectively) and the parameters of these fits are listed in table 4.10. Inset - the $H$ region 0.5 to 5 kOe for sample D.

| Parameter | Value | Units |
|---|---|---|
| $\mu$ | 12.1(1) | $\mu_B$ |
| $M_S$ | 0.0348(3) | emu cm$^{-3}$ |
| $\theta$ | 15.0(2) | K |
| $\alpha$ | $2.2(2) \times 10^{-5}$ | K$^{-1.5}$ |
| $\beta$ | $9.36(3) \times 10^{-3}$ | emu cm$^{-3}$ |
| $b$ | $-5.21(1) \times 10^{-7}$ | emu cm$^{-3}$ Oe$^{-1}$ |
| $\chi^2_{red}$ | 1.28 | n/a |

Table 4.11: Best fit parameters for the three term model to the $M$ vs $T$ data sets reported in figure 4.19.

the same procedures as earlier this size of magnetic moment would predict an average particle diameter of 7.2(3) nm, cf. $d_{TEM} = 12.19(7)$ nm. This is a reduction of $\approx$ 5 nm - following the trend from samples A, B and C in which the larger diameter had the larger reduction in diameter. If this particle follows the same behaviour as previously seen we will expect to see a strong Curie-tail behaviour in the high $H$, $M$ vs $T$ response and expect to find a value of $\mu_{shell}$ between 0.4 and 1.1 $\mu_B$.

### 4.6.2 Curie behaviour at high $H$

Figure 4.19 is the $M$ vs $T$ data taken for sample D at $H = 10$ and 50 kOe (green and orange respectively). As with previous measurements the Curie-tail feature is clear at low temperatures, with a marked increase in $M$ as $T$ approaches 5 K. The two most striking features, however, are the large difference between the 10 and 50 kOe data sets (again due to a low loading of Ni compared to previous samples) and the apparent approach to saturation in the 10 kOe data set. Unlike previous samples, which have a gradual increase in $M$ on decreasing $T$ to 5 K, the 10 kOe data set appears to tend to a constant value in the range 5 to 15 K. This would suggest that the Weiss temperature may have changed sign (mathematically giving an asymptote at finite temperature) and the magnetic species leading to this Curie behaviour have a ferromagnetic correlation. If this is the case the low $T$ data will not follow the proposed model and data approaching the Weiss temperature will need to be ignored.

The data sets were fit by the three term model as previously described, with both 10 and 50 kOe data sets sharing all free parameters. To allow for the possibility of a positive Curie constant, data within 10 K of the Weiss temperature was excluded from the fit. The resultant best fit is shown on figure 4.19 as the black lines and the

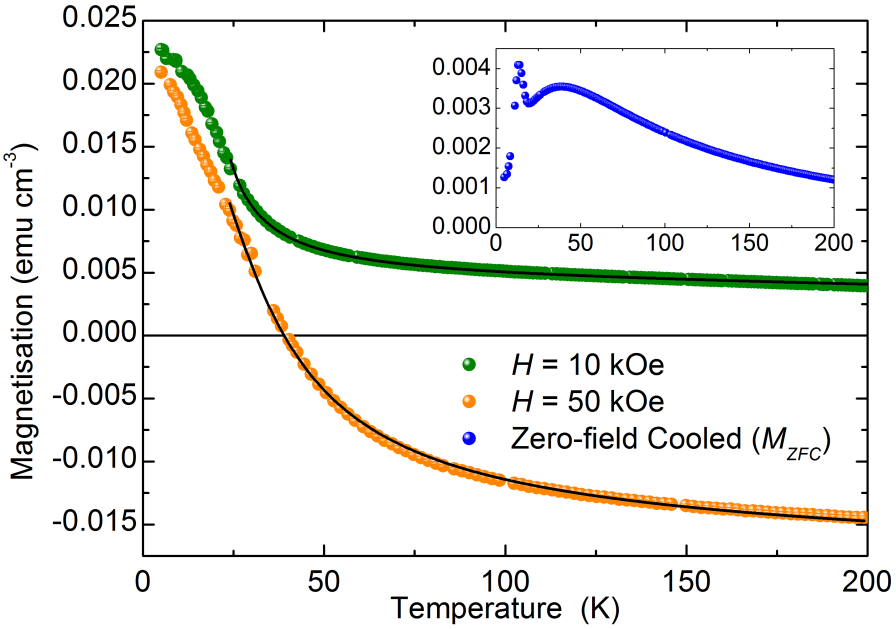


Figure 4.19: $M$ vs $T$ behaviour of sample D taken at $H = 10$ (green) and 50 kOe (orange). The lines represent the best fit to the data of the three term model and the parameters are summarised in table 4.11.

best fit parameters are summarised in table 4.11. Comparing the values found with samples A to C, the values of $\alpha$ and $b$ are of consistent size, however, $\mu$ has increased and (as predicted) $\theta$ is now positive.

A change in sign of $\theta$ is a sign that the surface magnetic species are now correlated ferromagnetically, instead of antiferromagnetically for previous samples. These species still have too large a magnetic moment to arise from a single atom, suggesting that this contribution to the magnetisation arises from multiple micro-domain ordered ferromagnetically within the domain and then correlated ferromagnetically to the neighbouring domains.

Corroboration of the value of $\theta$ can also be found by inspection of the zero-field cooled $M$ vs $T$ data (inset to figure 4.19), which shows a sharp peak in the magnetisation (unseen in the three previous samples where $\theta$ is negative) at 15 K. While these two values matching is far from conclusive, it does strengthen the case for a ferromagnetic correlation between the surface micro-clusters with $\theta \approx 15$ K.

Assuming at this stage that the parameters produced from the "three term" model are accurate and following the procedures previously outlined, the predicted average moment per shell, $\mu_{shell} = 35(1)$ k$\mu_B$. As previously stated, the Langevin and TEM predicted particle sizes differ by $\approx 5$ nm, accounting for a volume, $V_{shell} = 750(30)$ nm$^3$, and hence a magnetic moment per atom of $\mu_{shell} = 0.59(3)$ $\mu_B$. This value follows the same size dependence as previously suggested with $\mu_{shell}$ being slightly larger than that of sample D and close to the bulk value for Ni.

## 4.7 Summary and Conclusions

With the aim of verifying our methodology for determining the particle diameter of ferromagnetic nanoparticles via magnetisation measurements, we have applied the proposed method to 4 samples of Ni nanoparticle spanning the diameter range (according to TEM) 7 to 23 nm. For these four samples it is suggested that the Langevin fitting method previously described[36;62;30] in literature to compare the magnetic and physical volume of nanoparticles does not reflect the entire particle (as has been previously suggested[58;60;51]) with a "dead layer" of magnetic material at the surface.

An investigation of the low $T$, high $H$ magnetisation suggests that the atoms at the surface of the particle still possess a magnetic character and that at the surface the average moment per atom is increased. The surface moments mirror the magnetisation previously measured for ferrite nanoparticles,[97;154] demonstrating a Curie-tail

| $d_{TEM}$ (nm) | $d_{Lang}$ (nm) | $d_{Mag}$ (nm) | Sample I.D. |
|---|---|---|---|
| 7.69(6) | 5.4(1) | 9.0(2) | B |
| 8.88(7) | 5.6(1) | 10.6(2) | A |
| 12.19(7) | 7.2(3) | 12.1(5) | D |
| 23.0(4) | 11.0(6) | 21(1) | C |

Table 4.12: Summary of the particle sizes as found from TEM, the standard Langevin, and the surface corrected Langevin methods described above. To make comparisons easier the samples have been ordered based on their TEM sizes.

behaviour which is well modelled by a Weiss temperature corrected Langevin function, as previously applied to interacting "modified" super-paramagnetic systems.[149] These surface moments are consistent with the local ferromagnetic ordering of micro-clusters of atoms ($\approx$ 10 atoms), giving rise to a effective magnetic moment much larger than a single Ni atom could possess but much less than the comparable single domain moments. These cluster moments then form a magnetic structure with a "glassy" like behaviour, with the competing anisotropic and exchange interactions giving rise to both ferromagnetic and antiferromagnetic correlations between the surface magnetic micro-clusters.

Table 4.12 summarises the particle sizes predicted from TEM and Langevin fitting as well as the predicted particle size using the surface correction assuming that $\mu_{surface} = 0.61\ \mu_B$ (the bulk value). This assumption has been made as the technique is aimed at application to catalyst materials in which an exact comparison will not be available and understanding the magnitude of the systematic error introduced will describe the precision of this technique.

# Chapter 5

# Magnetic properties of Fischer-Tropsch and steam reforming catalysts

With our experimental approach tested on nanoparticle materials we can now address the industrial applicability of the magneto granulometry technique - whether or not magnetometry can be applied to supported nano-crystallites of Ni and Co as a method of determining their size. As previously stated the catalysts used industrially are relatively complex,[167] so the materials now being investigated will have a much wider pool of variables, not all of which will be well characterised. In particular, the support-metal interactions,[168] surface chemistry of the crystallites,[169] and distribution of metal/metal-oxide in crystallites[170] can be poorly defined, with a wide variation between catalysts preparations.[130]

To determine the potential agreement between the standard industrial techniques, of XRD and gas adsorption, and our proposed magnetometry methodology we will study three industrial catalysts, following the same procedure outlined in the previous chapter. We will first focus on the synthesis methods used to achieve a range of Ni crystallite sizes (section 5.1) before detailing the analysis of crystallite size via the current industrial methods of XRD and gas absorption utilised by Johnson-Matthey (JM) (section 5.2). With crystallite size values obtained using other techniques, and the relative difference between techniques which trouble catalysts characterisation demonstrated, the chapter will then turn to the magnetic techniques previously outlined. The magnetic analysis will first follow the Langevin approach (section 5.3.1), determining the average moment per particle from the

super-paramagnetic $H$ response and converting it to a crystallite size, before investigating the high $H$, $M$ vs $T$ behaviour to correct for the magnetic shell contribution (section 5.3.2). To finish, we will return to the "blocking temperature" analysis, described for samples A and B in the previous chapter (sections 4.2.5 and 4.3.5), to identify if $M$ vs $T$ data is also of use in determining the average crystallite size, and test for a sensitivity to a shift in the distribution of crystallite sizes (section 5.3.3).

## 5.1 Ni catalyst sample preparation

A standard Ni steam reforming catalyst was synthesised as described in section 3.2.2 by the Johnson-Matthey Chilton site. In order to achieve a range of particle sizes the final thermal treatment/ reduction step was carried out at a three temperatures (varying the treatment time in line with previous JM studies). The details of this treatment are summarised in table 5.1.

| Sample I.D. | Reduction time (hours) | Reduction temperature (°C) |
|---|---|---|
| $Ni_H$ | 8 | 700 |
| $Ni_S$ | 18 | 550 |
| $Ni_L$ | 62 | 400 |

Table 5.1: Reduction conditions for the three Ni samples studied.

In order to demonstrate the applicability of magnetometry as a crystallite sizing technique it is essential to compare the predicted crystallite sizes with the current industrial techniques. These take the form of gas adsorption, giving a catalyst surface area which can be converted to a crystallite size,[24] and x-ray diffraction (XRD), in which peak broadening can be converted to an average crystallite size.[171] Crystallite sizing can also be done via transmission electron microscopy (TEM)[172] however, due to the highly specialised nature, long sample preparation and poor image contrast (due to the similar atomic number between Ca in the support cement and the catalytic Ni), it is not a viable industrial technique.[173]

## 5.2 Ni catalyst - standard particle sizing techniques

### 5.2.1 Gas adsorption S.A.

Gas absorption isotherms have been measured, as previously outlined in section 3.1.5, using a $H_2$ gas feed for each of the three sample preparations. The experimental data for the gas adsorption studies carried out on the three preparations

i)

| Sample I.D. | D.o.R. (%)) | Abs.$_{Strong}$ ($m^2$ $g^{-1}$) | Abs.$_{Total}$ ($m^2$ $g^{-1}$) |
|---|---|---|---|
| $Ni_H$ | 98 | 17.7(5) | 22.3(5) |
| $Ni_S$ | 81 | 17.5(5) | 22.7(5) |
| $Ni_L$ | 61 | 20.9(5) | 25.0(5) |

ii)

| Sample I.D. | $d_{Strong}$ (nm) | $d_{Total}$ (nm) |
|---|---|---|
| $Ni_H$ | 14.5(4) | 11.5(3) |
| $Ni_S$ | 12.1(3) | 9.4(3) |
| $Ni_L$ | 7.6(2) | 6.4(2) |

Table 5.2: i) Measured gas adsorption and degree of reduction (D.o.R.) (taken from TPR) values for the three catalyst preparations. ii) Calculated crystallite diameters, $d$, based on both strong and total gas adsorption values.

($Ni_H$, $Ni_S$ and $Ni_L$) are given in table 5.2 i), reporting both total and strong adsorption, alongside the degree of reduction (D.o.R.) for each sample, measured via temperature-programmed reduction (TPR) by JM, Chilton. As is to be expected the TPR indicates the higher the reduction temperature the higher the degree of reduction.[174]

The gas absorption isotherm produces two measurements of the catalyst surface area, Abs.$_{Strong}$ and Abs$_{Total}$. Abs.$_{Total}$ refers to the total quantity of feed gas ($H_2$ for our experiments) absorbed by the sample during a continuous flow, while Abs.$_{Strong}$ refers to the quantity of Abs.$_{Total}$ that remains after exposure to a vacuum. These two values differ due to the different mechanisms of gas absorption, physisorption (arising from weak, long range interactions e.g. van der Waals and dipole-dipole) and chemisorption (arising from the chemical reaction of the surface and feed gas),[175] with Abs.$_{Total}$ dependent on both while Abs.$_{Strong}$ is dominated by chemisorption.[176]

When analysing the particulate size from gas absorption isotherms there are several factors to consider. Chemisorption favours a monolayer absorption compared to the multi layered structure possible for physisorption,[177] making analysis of Abs.$_{Strong}$ simpler. However, the chemisorption, while stronger than the physisorption, is also reversible meaning the value would reflect slightly less than a monolayer structure. Depending on the catalyst in question the preferred quantity varies (with different sections of JM relying on different analysis) hence we will present the analysis for both values.

Using these values and following the procedure outlined earlier (see section 3.1.5) the catalyst surface area and degree of reduction can be converted to an

average crystallite diameter.[178;179;180;181] These converted values are given in table 5.2 ii).

Clearly there is a relatively large discrepancy between the particle sizes determined from Abs.$_{Strong}$ and Abs.$_{Total}$, suggesting the mixture of Ni, NiO and catalyst support have led to a variety of absorption kinetics.[174] However, we do see a clear growth in particle size with an increase in the reduction temperature and the particle sizes are well within the diameter region already understood as being single domain ferromagnetic materials,[37] so the magnetic analysis should be applicable to these three samples.

### 5.2.2 X-ray diffraction (XRD) broadening analysis

Extracting crystallite sizes from gas adsorption studies assumes that the gas binds as a single, smooth monolayer and as such may over-estimate crystallite sizes (if the crystallite surface has a rough, fractal structure). XRD analysis uses the line broadening of the diffraction peaks to estimate crystallite size through the Scherrer equation, with the relationship derived in section 3.1.2. Scherrer analysis has the limitation that it assumes all line broadening arises from the particle size,[182] excluding broadening due to strain and imperfections in the crystal lattice and hence will always be an underestimation of the crystallite size. However, the two techniques taken together give boundaries to the actual crystallite size.

The XRD patterns taken from powdered samples of the catalysts are shown in figure 5.1. All 3 samples show scattering consistent with a mixture of bulk nickel[183] and nickel oxide[184] with an increasing NiO contribution for the lower reduction temperature - consistent with the degree of reduction (see table 5.2).

The XRD diffraction patterns were taken using a monochromated x-ray source, giving scattering from both the Cu K$\alpha_1$ and K$\alpha_2$ wavelengths. Hence, the XRD peaks were fitted with a superposition of two peak shapes, in this case the Pearson VII function,

$$I(q) = I_0 \left( 1 + \frac{4(2^{\frac{1}{s}} - 1)(q - q_0)^2}{w^2} \right)^{-s}, \tag{5.1}$$

where $I_0$ is the peak intensity, $q_0$ is the peak centre, $w$ is the full width half maxima (FWHM), and $s$ is the shape coefficient,[185] sharing a $d$ spacing but with individual wavelengths ($\lambda_1 = 1.5406$ Å and $\lambda_2 = 1.5444$ Å) where the intensity of the K$\alpha_2$ peak is half that of the K$\alpha_1$ peak. The four peaks assigned to nickel alone were fitted

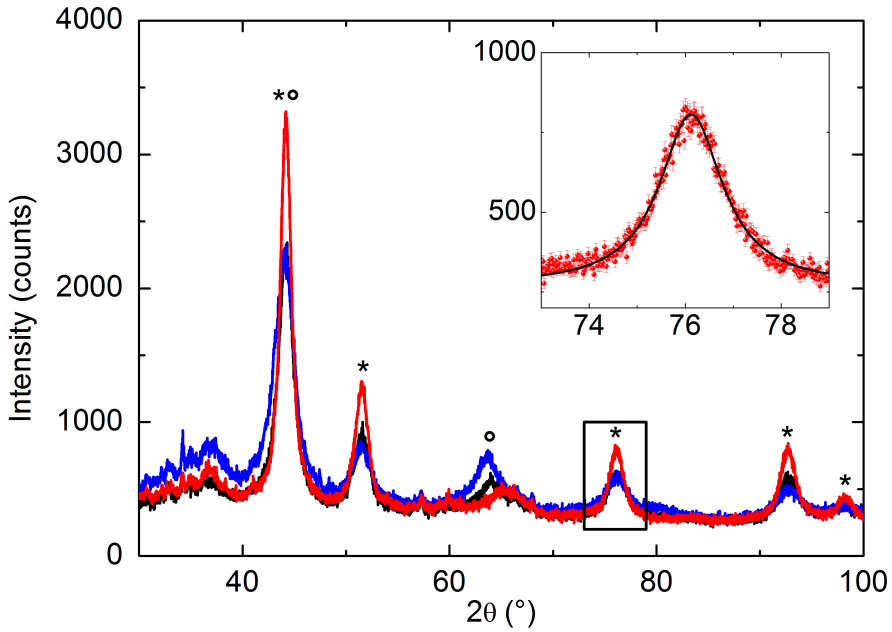


Figure 5.1: XRD patterns taken for sample $Ni_H$ (red), $Ni_S$ (black) and $Ni_L$ (blue) in the range $30 < 2\theta < 100$. The pattern has been assigned to the scattering of bulk nickel (*) and nickel oxide (°). Inset - an example fit of a Pearson VII function to the $Ni_H$ peak at $2\theta \approx 76°$.

| $2\theta$ (°) | $w$ (°) | $\tau$ (Å) | $a$ (Å) |
|---|---|---|---|
| 51.493(5) | 1.45(2) | 68.0(9) | 3.5488(3) |
| 76.127(7) | 1.54(2) | 71.4(9) | 3.5364(3) |
| 92.726(8) | 1.69(2) | 74(1) | 3.5324(2) |
| 98.19(2) | 1.46(8) | 73(3) | 3.5333(5) |

Table 5.3: Best fit parameters for the Pearson VII function fit to the XRD patterns for $Ni_H$ alongside the Scherrer analysed average crystallite size, $\tau$, and lattice parameter, $a$.

with a shared value for the peak shape parameter, $s$, but individual peak widths, $w$, and peak positions. The Pearson VII function has been chosen as a general peak function, reproducing both Gaussian and Lorentzian peak shapes ($s = \infty$ and 1 respectively) as well as behaviour in between the two. The peaks closely reproduce the data, with a typical peak fit shown in the inset to figure 5.1, and the best fit parameters given in table 5.3 alongside the calculated average crystallite size calculated, $\tau$, and lattice parameters, $a$. The values of $\tau$ were calculated using the Scherrer equation given in section 3.1.2 assuming a value of $\kappa = 1$.

The average crystallite size, $\tau$, and lattice parameter, $a$, for the $Ni_H$ sample determined from the 4 peaks are not in agreement, demonstrating a range in excess of the expected error, suggesting the current analysis is inaccurate. In order to reduce the number of free parameters available to the fit, the diffraction pattern is converted into $q$ space, using the K$\alpha_1$ wavelength, and the resulting diffraction pattern shown in figure 5.2. By analysing the data in $q$ space the peak width, $w$, is no longer dependent on the peak position. Hence, the peak width, $w$, and peak shape coefficient, $s$, can be shared between the 4 peaks when fitting.

To further reduce the number of free parameters, the $q$ space diffraction was fitted using a shared value of the lattice parameter, $a$, with the individual peak positions determined from the $d$ spacing for the relevant peaks following the equation,

$$d^2 = \frac{a^2}{h^2 + k^2 + l^2}, \tag{5.2}$$

assuming that the 4 peaks of interest in order of increasing $q$ are the 200, 220, 113 and 222, respectively.

Fitting the $Ni_H$ data set in this way fails to reproduce the data accurately, with a $\chi^2_{red.} = 2.71$ and a large discrepancy between the fit and data for the 200 peak (shown as the green line on the inset to figure 5.2). Calculating the skewness, defined as

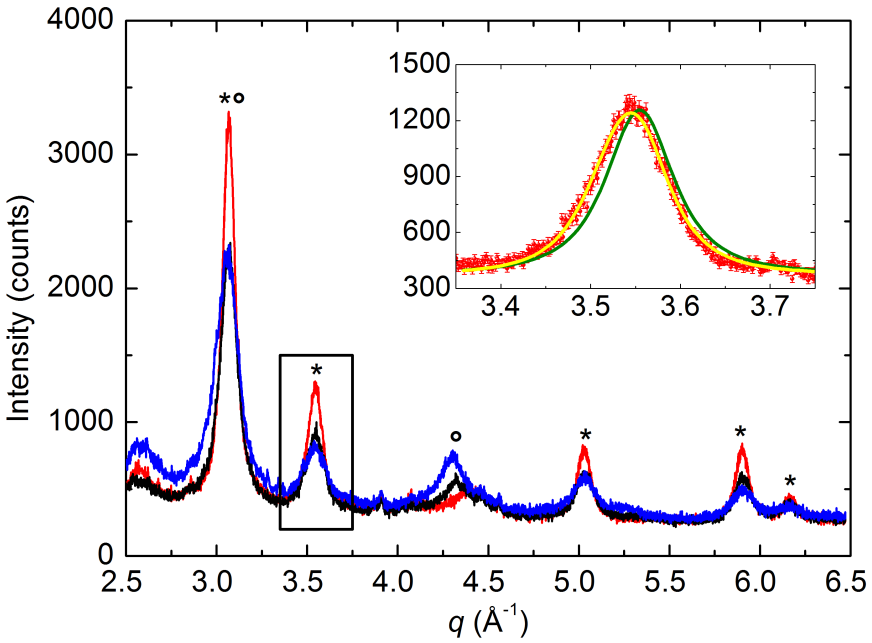


Figure 5.2: XRD patterns taken for sample $Ni_H$ (red), $Ni_S$ (black) and $Ni_L$ (blue) converted into $q$ space assuming $\lambda = 1.5406$ Å. The pattern has been assigned to the scattering of bulk nickel (*) and nickel oxide (°). Inset - a comparison of the Pearson VII fits with (yellow) and without (green) a shoulder to the $Ni_H$ peak at $q \approx 3.55$ Å.

$$g = \frac{\frac{1}{n}\sum_{i=1}^{n}(x-\bar{x})^3}{(\frac{1}{n}\sum_{i=1}^{n}(x-\bar{x})^2)^{\frac{3}{2}}}, \tag{5.3}$$

where $\bar{x}$ is the mean of the $x$ values, of the four peaks reveals a positive skew for the higher intensity peaks. It appears that the peaks centred at $q = 3.54$ Å$^{-1}$ and $q = 5.05$ Å$^{-1}$ possess a shoulder at lower $q$, and hence the data is re-fit allowing for a second peak function at both positions, applying the same wavelength split between the K$\alpha_1$ and K$\alpha_2$, with a shared peak width and shape parameter. This new approach gives an improved $\chi^2_{red.} = 1.26$ and a close reproduction of the data (shown as the yellow line on the inset to figure 5.2). The method has been repeated on the samples $Ni_S$ and $Ni_L$, with the diffraction patterns shown on figure 5.2, and the best fit parameters summarised in table 5.4.

| Sample | $a$ (Å) | $w$ (Å$^{-1}$) | $s$ | $\chi^2_{red.}$ |
|---|---|---|---|---|
| $Ni_H$ | 3.5334(2) | 0.079(1) | 1.19(9) | 1.26 |
| $Ni_S$ | 3.5315(4) | 0.106(2) | 1.1(2) | 1.22 |
| $Ni_L$ | 3.5324(6) | 0.131(4) | 1.4(3) | 1.25 |

Table 5.4: Best fit parameters for the Pearson VII function fit to the XRD patterns for $Ni_H$, $Ni_S$, and $Ni_L$ samples.

The Pearson VII fit shows a variation in peak width, $w$, between samples. In an XRD experiment we are measuring a Fourier transform of some real space distribution, and when applied to the Scherrer analysis we are comparing the width in reciprocal space, $\Delta q$, to the correlation length in real space, $\Delta x_{\frac{1}{e}}$ (i.e. the point at which the real space function drops to $\frac{1}{e}$ of its maximum). The relationship between these two terms is dependent on the peak shape such that,

$$\frac{f}{\Delta q} = \Delta x_{\frac{1}{e}} \tag{5.4}$$

where $f$ is 3.33 for a Gaussian and 2 for a Lorentzian peak shape. In the case of a Pearson VII peak, the value of $f$ will depend on the peak shape factor, $s$, but the behaviour can be deduced from the general peak shape by taking the inverse Fourier transform at $q_0 = 0$ and $A_0 = 1$. The variation in $f$ as a function of $s$ is shown in figure 5.3. The value, $f$, is related to the Scherrer constant by a factor of $\pi$ (i.e. $\kappa = \frac{f}{\pi}$) and hence the normal Scherrer analysis assumption that $\kappa = 0.9$ only holds at $s \approx 2.2$.

With the general behaviour of $f$ with variation in $d$ determined, it is possible

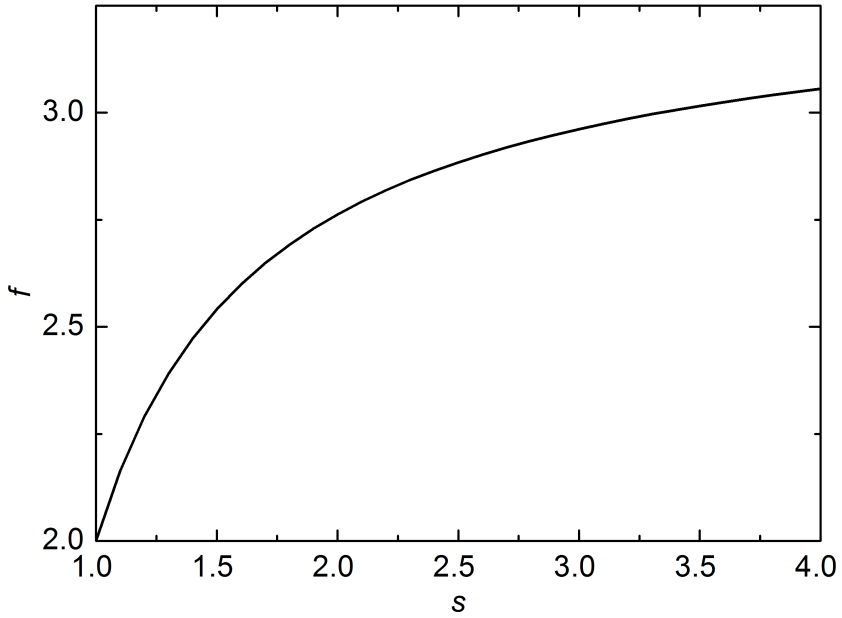


Figure 5.3: Variation in the conversion parameter, $f$, with the Pearson VII peak shape coefficient, $s$.

to convert the experimental peak broadening into a real space value, reflecting the radius at which the average scattering potential drops below $\frac{1}{e}$, and the values are given in table 5.5. Clearly, the XRD determined particle sizes are smaller than those determined from gas adsorption isotherms, but this is not surprising. The line broadening in $q$ relates to the correlation length of the real space scatterer, taking into account the range of particle sizes and any variation in scattering intensity between the centre and surface of the crystallites, while the gas adsorption is a surface technique, following only the outer most atoms.

| Sample | $f$ | $d_{XRD}$ (Å) |
|---|---|---|
| $Ni_H$ | 2.28(9) | 58(2) |
| $Ni_S$ | 2.2(2) | 42(2) |
| $Ni_L$ | 2.5(2) | 38(3) |

Table 5.5: $q$ space XRD analysis summary for the samples $Ni_H$, $Ni_S$, and $Ni_L$.

In order to explain the difference between gas adsorption and XRD particle

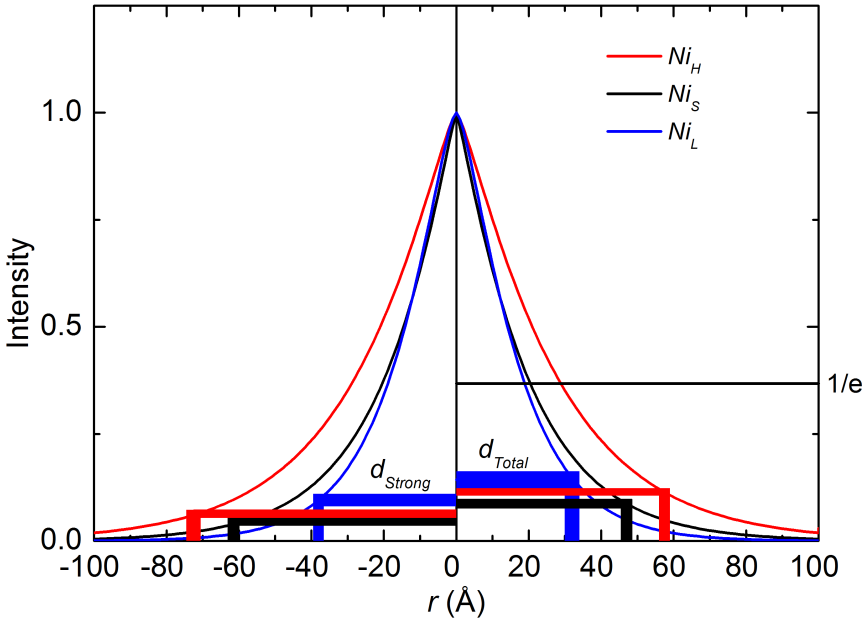


Figure 5.4: Real space scattering intensity of the samples $Ni_H$ (red), $Ni_S$ (black), and $Ni_L$ (blue) determined from the inverse Fourier transform of the peak shape. The solid lines represent the particle diameters from the gas adsorption studies and the predicted real space scattering intensities.

sizes, the real space scattering intensity is plotted as figure 5.4 with the equivalent gas adsorption particle sizes (from both strong and total values) included for comparison as the coloured rectangles, with thickness representative of the standard error. A disagreement between XRD and gas adsorption is generally expected due to the assumptions made during data analysis, but by comparing the real space scattering distribution of the XRD with the gas adsorption sizes it becomes clear that the two techniques are inherently sensitive to different parts of the particle, it is only if the real space scattering was a step function that we could expect the $\Delta x_{\frac{1}{e}}$ to be reflected in the gas adsorption studies.

The values of particle size arrived at from XRD and gas adsorption supply a window of crystallite sizes within which we can expect to find the distribution of crystallite diameters and demonstrates how the concept of a particle size can be misleading when applied to XRD as it is the average of the scattering that we observe.

When drawing comparisons between the magnetic granulometry particle diameters and the standard industrial sizing techniques, the XRD and gas adsorption sizes will have to be treated as boundaries for the true crystallite size.

## 5.3 Nickel catalyst magnetic studies

With the Ni catalysts analysed via the standard industrial methods we can now test the reliability and viability of the magnetic techniques. As with the Ni nanoparticles reported in the previous chapter all magnetisation studies have been carried out using the QD MPMS SQUID magnetometer working in dc-magnetisation mode. Unlike the previous investigation, in which the particles could be diluted using the Fomblin grease, the catalysts are to be studied as individual extrudites as would be supplied by JM.

The extrudites analysed are cylindrical with diameter and height of $\approx$ 3 mm consisting of Ni, NiO and calcium carbonate cement in varying quantities. The SQUID system has been calibrated to treat a sample of $\leq$ 3 mm as a point dipole,[186] placing the extrudites within the systems range. These larger samples (and the associated higher loading of Ni) also mean a greatly increased magnetic signal. The samples are mounted as solid extrudites within the magnetometer using the low background straws with the cylinder orientated within the direction of the applied field as represented schematically in figure 5.5.

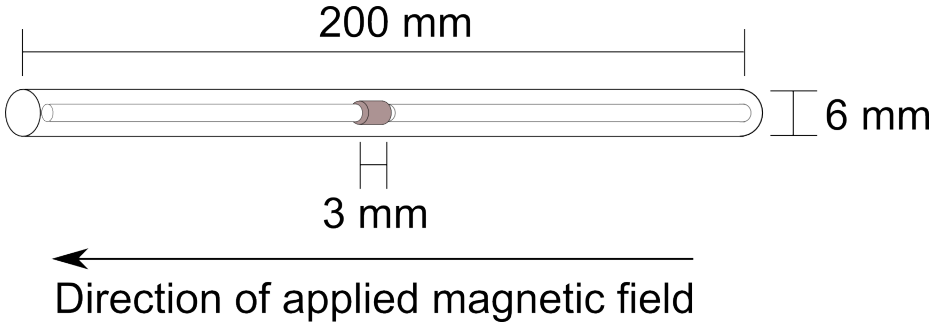


Figure 5.5: Schematic of the sample mounting demonstrating the Ni extrudite (a cylinder with a radius and height of 3mm, grey) positioned centrally in a straw formed of a plastic with a low magnetic susceptibility. The sample is held in place by two thin pieces of the same plastic and Kapton tape blocking one end. The uncovered end is attached to the sample rod via Kapton tape.

### 5.3.1 The Langevin approach

The magnetic investigation will begin with the commonly reported approach of the Langevin model.[42] As with the Ni nanoparticles the magnetisation is measured as a function of applied field however, as the aim is to produce a rapid technique, a single high $T$ data set will be used for each sample (as was done for samples C and D in section 4.4). The data is then fit with both single and dual Langevin functions, where $\mu$ is assumed to be proportional to the average crystallite size, to determine which model gives a closer reproduction of the observed $M$.

Figure 5.6 shows the $M$ vs $H$ data for sample $Ni_H$ taken at $T = 200$ K taken as a 6 quadrant scan ($H_{Max} = 50$ kOe). The magnetisation is reversible as is expected for a super-paramagnetic material. The fits to the data represent lines of best fits for both the single Langevin and dual Langevin models - in both cases corrected by a linear, $T$ independent background. The parameters for these models are summarized in table 5.6.

| Parameter | Single Langevin model | Dual Langevin model | Units |
|---|---|---|---|
| $\mu_1$ | 14.6(2) | 4.89(6) | k$\mu_B$ |
| $\mu_2$ | n/a | 28.9(3) | k$\mu_B$ |
| $M_{S1(200\ \mathrm{K})}$ | 8.57(3) | 3.86(5) | emu g$^{-1}$ |
| $M_{S2(200\ \mathrm{K})}$ | n/a | 5.12(5) | emu g$^{-1}$ |
| $b$ | $2.6(1) \times 10^{-5}$ | $1.42(2) \times 10^{-5}$ | emu g$^{-1}$ Oe$^{-1}$ |
| $\chi^2_{red}$ | 39.2 | 0.55 | |

Table 5.6: Best fit parameters for the single and dual Langevin models to the $M$ vs $H$ data for sample $Ni_H$ taken at $T = 200$ K. As expected the dual Langevin model gives a $\chi^2_{red}$ closer to 1 - indicating a superior fit.

The dual Langevin model gives a superior fit with the smaller $\chi^2_{red}$ and a closer reproduction of the data - especially at the low $H$ range (as shown in the inset to figure 5.6). Unlike for the previous nanoparticle studies the linear correction factor corresponds to a positive susceptibility - possibly arising from the calcium carbonate cement used to support the crystallites. Alternatively, as the nickel oxide has a very weak paramagnetic susceptibility[187] - the linear background may grow as the degree of reduction is decreased.

As with the nanoparticle materials the superior fit of the dual Langevin model can be assigned to a log-normal distribution of particles sizes, in which the values of $\mu_1$ and $\mu_2$ represent the 20 and 80 % limits of the cumulative distribution.

Figure 5.7 shows the $M$ vs $H$ data for sample $Ni_S$ taken at $T = 200$ K.

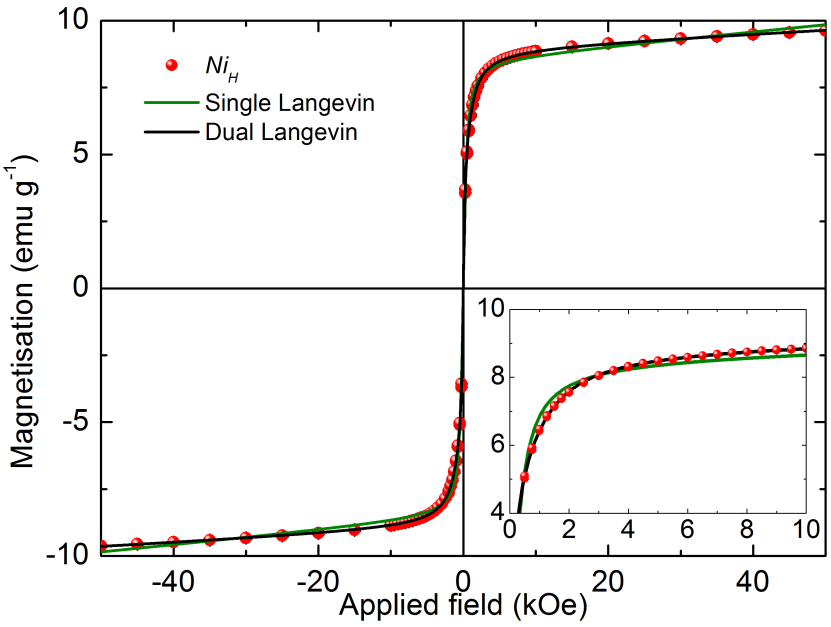


Figure 5.6: $M$ vs $H$ data for sample $Ni_H$ taken at $T = 200$ K. The lines represent the best fits by both the single and dual Langevin models (green and black respectively). Inset - Magnetisation data in the range $H = 1$ to 10 kOe demonstrating the superior fit of the dual Langevin model.

| Parameter | Single Langevin model | Dual Langevin model | Units |
|---|---|---|---|
| $\mu_1$ | 1.11(1) | 4.29(6) | k$\mu_B$ |
| $\mu_2$ | n/a | 21.9(3) | k$\mu_B$ |
| $M_{S1(200\ \mathrm{K})}$ | 10.70(3) | 5.51(7) | emu g$^{-1}$ |
| $M_{S2(200\ \mathrm{K})}$ | n/a | 5.77(7) | emu g$^{-1}$ |
| $b$ | $2.8(2) \times 10^{-5}$ | $1.13(3) \times 10^{-5}$ | emu g$^{-1}$ Oe$^{-1}$ |
| $\chi^2_{red}$ | 45.1 | 1.07 | |

Table 5.7: Best fit parameters for the single and dual Langevin models to the $M$ vs $H$ data for sample $Ni_S$ taken at $T = 200$ K. As for $Ni_H$ the dual Langevin model gives the better fit.

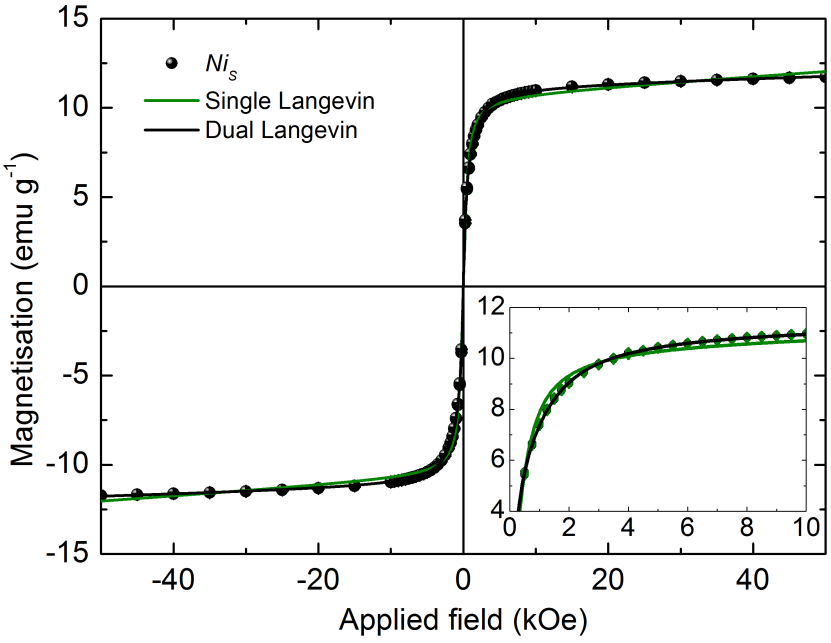


Figure 5.7: $M$ vs $H$ data for sample $Ni_S$ taken at $T = 200$ K. The lines represent the best fits by both the single and dual Langevin models (green and black respectively). Inset - Magnetisation data in the range $H = 1$ to 10 kOe demonstrating the superior fit of the dual Langevin model.

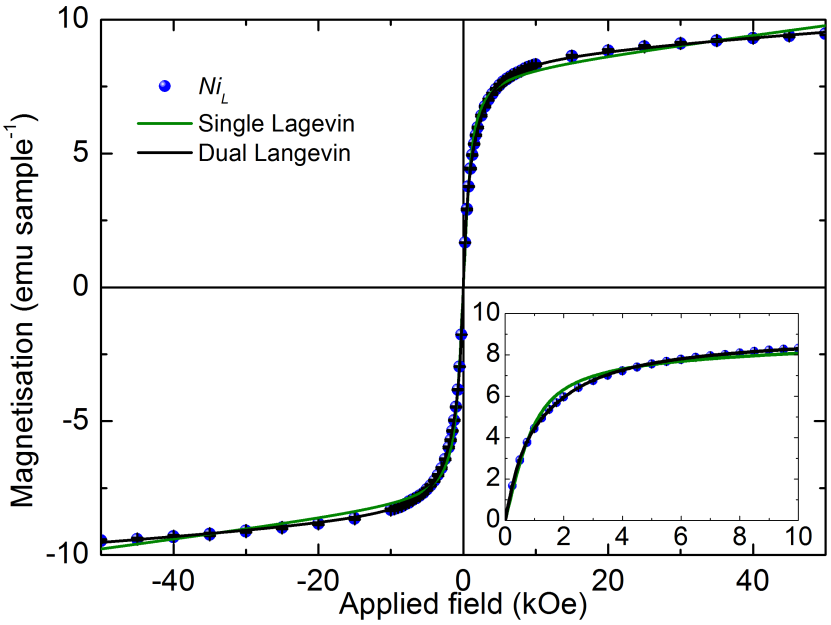


Figure 5.8: $M$ vs $H$ data for sample $Ni_L$ taken at $T = 200$ K. The lines represent the best fits by both the single and dual Langevin models (green and black respectively). Inset - the magnetisation data in the range $H = 1$ to 10 kOe demonstrating the superior fit of the dual Langevin model.

Again, the magnetisation is reversible with $H$ at this temperature. The data is fit by both single and dual Langevin models with a better fit by the dual Langevin model ($\chi^2_{red} = 1.07$ cf. 42.1 for the dual and single Langevin models, respectively). The best fit parameters are summarized in table 5.7. As is to be expected from the XRD and gas adsorption studies the $Ni_S$ sample gives a reduced moment per particle cf. $Ni_H$.

Figure 5.8 shows the $M$ vs $H$ data for sample $Ni_L$ at $T = 200$ K. As previously the magnetisation is reversible with $H$ at this temperature. The dual Langevin model gives the superior fit compared with the single Langevin model though the value of $\chi^2_{red}$ is higher than expected. The best fit parameters to the two model fits are summarized in table 5.8. The average moment per particle, $\mu$, for the $Ni_L$ sample cf. $Ni_S$ and $Ni_H$ follows the trend expected from gas adsorption and XRD analysis.

The values of $\mu$ determined via fitting can be converted into a volume if we

| Parameter | Single Langevin model | Dual Langevin model | Units |
|---|---|---|---|
| $\mu_1$ | 6.53(9) | 2.69(5) | k$\mu_B$ |
| $\mu_2$ | n/a | 12.8(2) | k$\mu_B$ |
| $M_{S1(200\ \mathrm{K})}$ | 8.09(4) | 4.72(8) | emu g$^{-1}$ |
| $M_{S2(200\ \mathrm{K})}$ | n/a | 4.00(8) | emu g$^{-1}$ |
| $b$ | $3.5(2) \times 10^{-5}$ | $1.87(5) \times 10^{-5}$ | emu g$^{-1}$ Oe$^{-1}$ |
| $\chi^2_{red}$ | 54.3 | 1.69 | |

Table 5.8: Best fit parameters for the single and dual Langevin models to the $M$ vs $H$ data for sample $Ni_L$ taken at $T = 200$ K. As for $Ni_H$ and $Ni_S$ the dual Langevin model gives the better fit.

assume 0.61 $\mu_B$ atom$^{-1}$ (the value for bulk Ni[153]) and a density, $\rho = 8.908$ g cm$^{-3}$. The values determined from the dual Langevin method represent the 20 and 80% limits of the cumulative distribution (assuming the crystallite sizes follow a log-normal distribution) and while these values can be used to determine the median particle size as the comparison techniques give a window of possible particle sizes the comparison will be made with the particle size limits. For each of the three samples the resultant parameters are summarised in tables 5.9 and 5.10 for both magnetic and structural terms, respectively.

| Sample | Mag$_{20\%}$ ($k\mu_B$) | Mag$_{80\%}$ ($k\mu_B$) | Mag$_{Median}$ ($k\mu_B$) |
|---|---|---|---|
| $Ni_L$ | 2.69(5) | 12.8(2) | 5.90(7) |
| $Ni_S$ | 4.29(6) | 21.9(3) | 9.69(9) |
| $Ni_H$ | 4.89(6) | 28.9(3) | 11.8(1) |

Table 5.9: Summary of the $\mu_{eff}$ values determined from the dual Langevin model alongside the calculated median value of the distribution. The calculation assumes a log-normal distribution of crystallite sizes where the fitted values lie at 20 and 80% of the cumulative total.

| Sample | $d_{Mag20\%}$ | $d_{Mag80\%}$ | $d_{Gas\ (Strong)}$ | $d_{Gas\ (Total)}$ | $d_{XRD}$ |
|---|---|---|---|---|---|
| $Ni_H$ | 5.51(2) | 9.96(4) | 14.5(4) | 11.5(4) | 5.8(2) |
| $Ni_S$ | 5.28(2) | 9.09(4) | 12.1(3) | 9.4(3) | 4.2(2) |
| $Ni_L$ | 4.51(3) | 7.60(4) | 7.6(2) | 6.4(2) | 3.8(2) |

Table 5.10: Comparison of the crystallite diameters predicted from the Langevin method with gas adsorption and XRD analysis, with all values stated in nm. The magnetic diameters are converted from the values of $\mu$ reported in table 5.9. These calculations assume the bulk values for the magnetic moment per atom, 0.61 $\mu_B$ atoms$^{-1}$, and density, $\rho = 8.908$ g cm$^{-3}$.

The $M$ vs $H$ studies produce an interesting situation. As previously stated the XRD can be expected to underestimate the average particle size, with values close to the 20% limit for the three sample. The gas absorption conversely, is expected to overestimate particle size - with the true value sitting somewhere between the $d_{Strong}$ and $d_{Total}$ values, but the 80% limit appear to be on the lower limit of the size window, suggesting some fraction of the particles is not being included. This is similar to the situation we observed for the nanoparticle samples in the previous chapter in which the larger samples possessed an increased effective "dead-layer" as the single domain structure grew. In order to investigate the "dead-layer" corrected values the high $H$, $M$ vs $T$ analysis will be repeated on these samples.

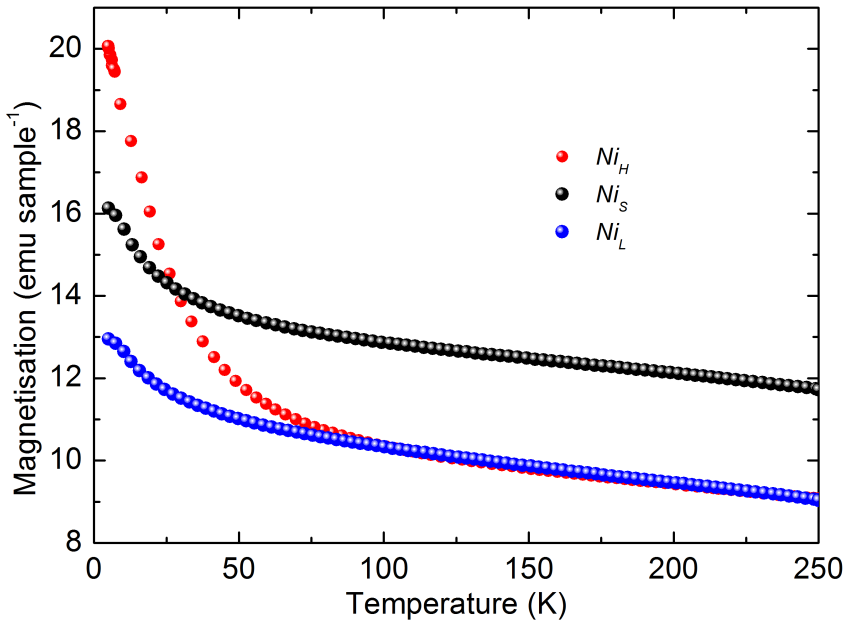


Figure 5.9: $M$ vs $T$ data sets for sample $Ni_H$, $Ni_S$, and $Ni_L$ taken at $H = 50$ kOe over the temperature range 5 to 250 K. The magnetisation at $T = 200$ K matches the values measured via $M$ vs $H$ scans but as $T$ decrease the magnetisation has a Curie-tail behaviour.

### 5.3.2 "Dead-layer" studies

Figure 5.9 shows the $M$ vs $T$ data for the three samples taken at $H = 50$ kOe. As the temperature is decreased the saturation magnetisation increases as a Curie behaviour - suggesting the presence of small magnetic moment, paramagnetic material. This behaviour mimics the behaviour observed for the nanoparticle materials across a range of particle sizes (see sections 4.2.2, 4.3.2, 4.5.2, and 4.6.2) as well as in samples of nano FeO[188] and has been suggested to arise from the surface atoms of the particle.

Interestingly, the saturation magnetisations at 5 K give a ratio (1.0:0.80:0.65) close to the ratio of degree of reduction previously determined (1.0:0.82:0.62). The saturation at low $T$ differs from the high $T$ values as they include the magnetisation of these smaller magnetic moments. This suggests two things - i) that we can determine the relative degree of reduction for the same Ni loading by comparing the low $T$ magnetisation and ii) that the magnetisation arising from the smaller paramagnetic moments may be proportional to the volume of the "dead-layer" at the particle surface.

Figure 5.10 shows the $M$ vs $T$ scan for the $Ni_H$ sample taken at $H = 50, 40$ and 30 kOe (red, black, and green respectively). For each applied field there is a rapid decrease in magnetisation at the temperature is increased, reaching a value of $M$ comparable to that observed from the $M$ vs $H$ scans. A close inspection of the curves show that in the high $T$ region (above $\approx$ 150 K) the magnetisation begins to curve downwards with increasing $T$. This is analogous to the decrease in magnetisation of a ferromagnetic domain by spin-waves as observed for the Ni nanoparticles in section 4.2.2.

This means we can model this system as a superposition of three terms,

$$M = M_S \left( \coth(\frac{\mu H}{k_B(T-\theta_{CW})}) - \frac{\mu H}{k_B(T-\theta_{CW})}^{-1} \right) + \beta(1 - \alpha T^{\frac{3}{2}}) + bH, \quad (5.5)$$

comprising a Langevin term, for the small moment paramagnetic moments (where $M_S$ is the saturation magnetisation, $\theta_{CW}$ is a thermal correction for inter-moment correlations and $\mu$ is the size of the magnetic moment), a spin wave term (with a scaling factor $\beta$ which is the magnetic saturation of the super-paramagnetic moment at $T = 0$ K and a proportionality constant $\alpha$), and a $T$ independent background term $b$ (which scales linearly with $H$). The physical interpretation of this model is illustrated in figure 5.11 demonstrating our current hypothesis that the magnetic

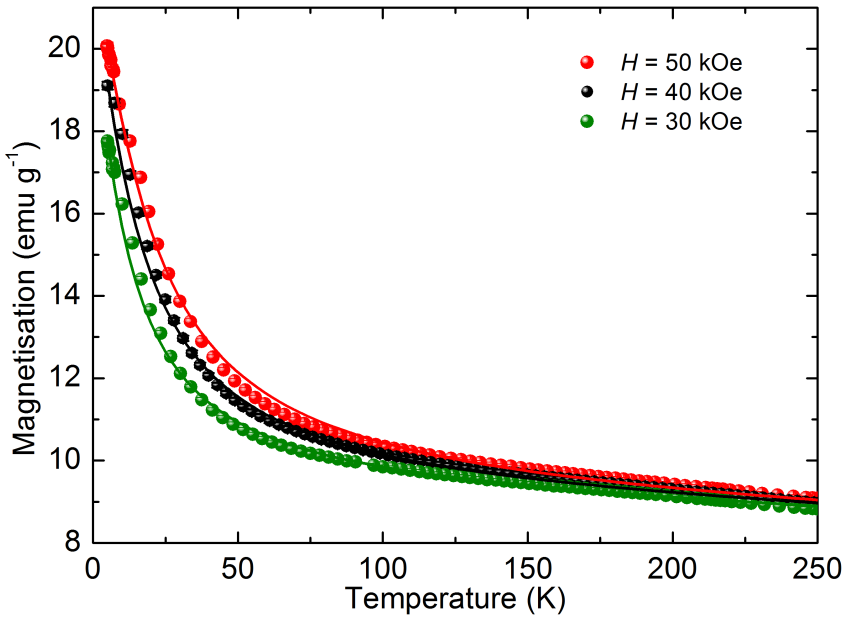


Figure 5.10: $M$ vs $T$ data sets taken for sample $Ni_H$ at $H$ = 50, 40, and 30 kOe. The data sets from all applied fields show a Curie tail behaviour in the low $T$ range (≈5 to 100 K). The lines represent the best fit to the "three term" model given in equation 5.5.

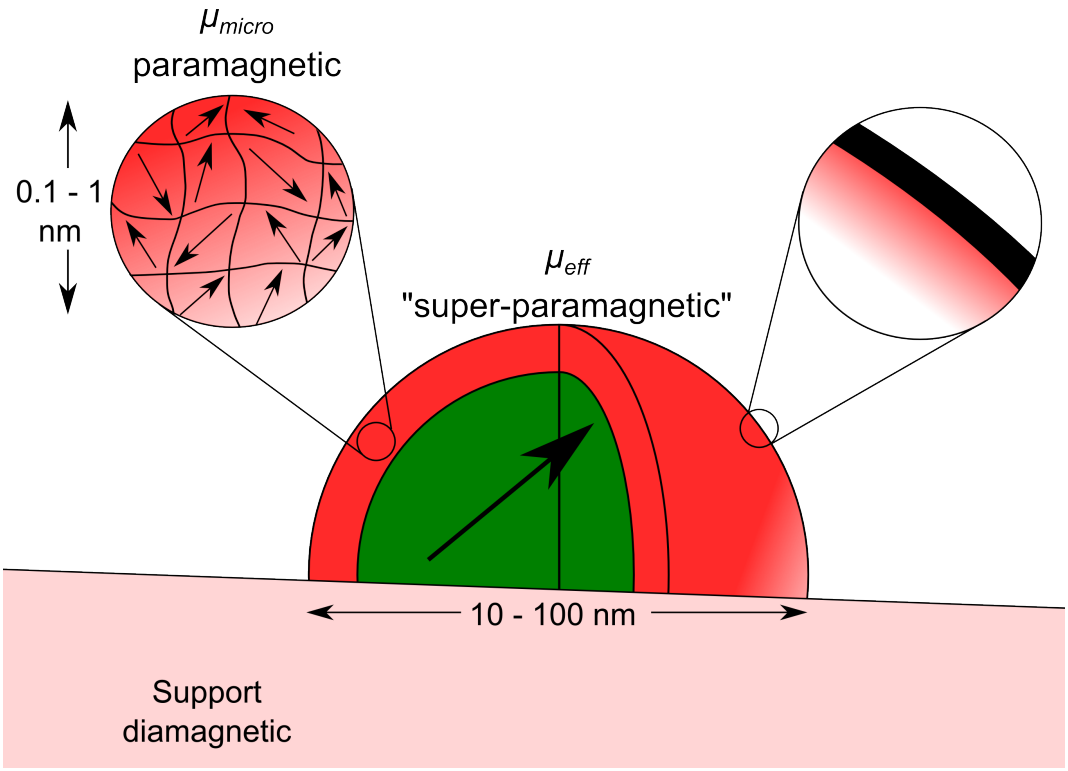


Figure 5.11: Schematic representation of the proposed magnetic system comprising three magnetic contributions; i) a super-paramagnetic core magnetic moment (green) of $\approx 10^4 \mu_B$ ii) multiple paramagnetic shell magnetic moments (red) each of $\approx 10\ \mu_B$ iii) a linear contribution arising from the diamagnetic support and NiO.

signal is composed of a super-paramagnetic contribution from the crystallite core, a small moment paramagnetic contribution from the outer shell and a $T$ independent contribution arising from both NiO and the support material.

The fit was carried out on the 30, 40, and 50 kOe data sets simultaneously with all free parameters shared - the result of which are plotted as the solid lines in figure 5.10. The same procedure is carried out on the $Ni_S$ and $Ni_L$ samples (see figures 5.12 and 5.13) and the best fit parameters for all 3 are summarized in tables 5.11 and 5.12.

The best fit parameters serve to reinforce the larger magnetisation of the $Ni_H$ sample when the temperature is reduced - an increase in $M$ of $\approx 1.5$ between the 5 and 200 K measurements. As with the previous work done on nanoparticles, the model requires a Weiss temperature, $\theta_{CW}$, in order to reproduce the experimental measurements. This parameter suggests an antiferromagnetic correlation between

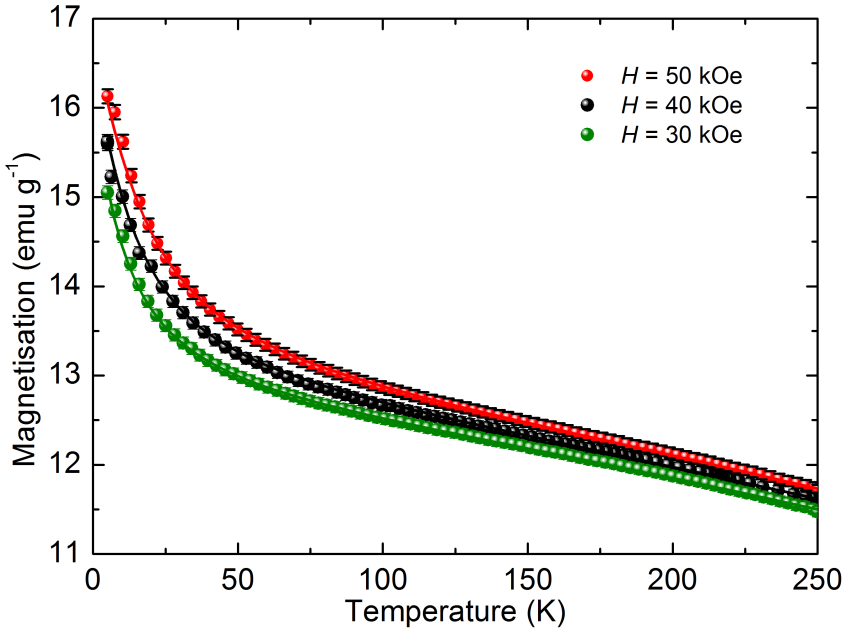


Figure 5.12: $M$ vs $T$ data sets for sample $Ni_S$ with $H = 50$, 40, and 30 kOe. The lines represent the best fit to the "three term" model given in equation 5.5.

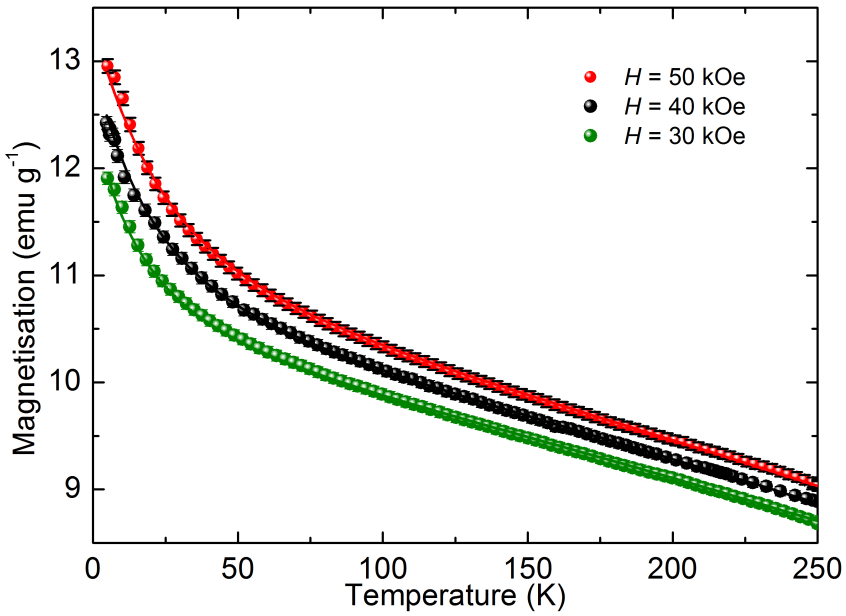


Figure 5.13: $M$ vs $T$ data sets for sample $Ni_L$ with $H = 50$, 40, and 30 kOe. The lines represent the best fit to the "three term" model given in equation 5.5.

| Sample | $\mu$ ($\mu_B$) | $M_S$ (emu g$^{-1}$) | $\theta_{CW}$ (K) |
|---|---|---|---|
| $Ni_H$ | 11.7(1) | 15.61(7) | -5.5(1) |
| $Ni_S$ | 10.7(2) | 4.9(1) | -5.7(3) |
| $Ni_L$ | 15.0(3) | 4.3(1) | -12.4(5) |

Table 5.11: Best fit parameters of the surface term of the "three term" model for each of the three sample $Ni_H$, $Ni_S$, and $Ni_L$.

| Sample | $\beta$ (emu g$^{-1}$) | $\alpha$ ($K^{-\frac{3}{2}}$) | $b$ (emu g$^{-1}$ Oe$^{-1}$) | $\chi^2_{red}$ |
|---|---|---|---|---|
| $Ni_H$ | 9.03(2) | $1.02(5) \times 10^{-5}$ | $-8.6(7) \times 10^{-6}$ | 1.84 |
| $Ni_S$ | 12.25(1) | $2.28(2) \times 10^{-5}$ | $7.0(3) \times 10^{-6}$ | 0.21 |
| $Ni_L$ | 9.491(7) | $3.40(2) \times 10^{-5}$ | $1.08(2) \times 10^{-5}$ | 0.18 |

Table 5.12: Best fit parameters of the core and support terms of the "three term" model for each of the three sample $Ni_H$, $Ni_S$, and $Ni_L$.

the surface magnetic clusters. The increase in $|\theta_{CW}|$ for the $Ni_L$ sample cf. $Ni_S$ and $Ni_H$ is likely a result of either the variation in particle size or the increasing nickel oxide content (due to nickel oxides antiferromagnetic nature,[108] $T_N = 525$ K). Comparable sized nanoparticles studied in the previous chapter (see section 4) did not show this increased magnitude, suggesting it is due to the oxide content.

The three catalyst samples possess a negative Weiss temperature, suggesting each cluster of atoms in the shell experience an antiferromagnetic correlation with the other surface states (as was demonstrated for samples A, B and C in sections 4.2.2, 4.3.2, and 4.5.2 respectively). The $M$ vs $T$ data sets for the three samples show no clear evidence for a transition to an antiferromagnetically ordered state, though the $Ni_L$ sample does demonstrate a slight deviation from the predicted behaviour below $\approx 15$ K.

Interestingly the effective moment of each body in the outer shell, $\mu$, is of a similar size, $\approx 10 - 15$ $\mu_B$. This moment is too large to arise from a single Ni atom - suggesting a local micro-domains of several atoms is formed. These micro-domains consists of ferromagnetically order nickel moments, with each micro-domain experiencing an antiferromagnetic correlation to the neighbouring micro-domain (manifesting as the $\theta_{CW}$ parameter). This competition between the ferromagnetic ordering and antiferromagnetic correlations, alongside the magneto-crystalline and surface anisotropies, is likely the reason for this system magnetic behaviour being similar to the "glassy" ferrite materials previously reported with this high $H$ Curie behaviour.[97;154]

Comparing these fits to the $M$ vs $H$ data taken at 200 K it is clear that the

linear background terms $b$ do not match. This is because at high $T$ the $M$ vs $H$ background is a superposition of both the surface and linear contributions, while in the high $H$, $M$ vs $T$ analysis it is solely the linear contribution. In the case of the $Ni_H$ sample the linear background is a simple diamagnetic background due to the sample mounting and the cement. However, for the $Ni_S$ and $Ni_L$ samples the increased NiO content introduces its own weak paramagnetic susceptibility creating a positive background term, with a larger signal from the $Ni_L$ sample due to its higher NiO content.

At this point we have identified the average effective magnetic moment per particle (which we will assume arises purely from the core of the crystallite), the magnetic saturation of the core and the magnetic saturation of the outer-shell. Using the ratio of core and shell saturation we can calculate the average moment per shell for each preparation method - the values for which are summarized in table 5.13.

| Sample | $M_{S\ Core}$ (emu g$^{-1}$) | $M_{S\ Shell}$ (emu g$^{-1}$) | $\mu_{Core}$ ($k\mu_B$) | $\mu_{Shell}$ ($k\mu_B$) |
|---|---|---|---|---|
| $Ni_H$ | 9.03(2) | 15.61(7) | 11.8(1) | 20.3(2) |
| $Ni_S$ | 12.25(1) | 4.9(1) | 9.69(9) | 3.87(8) |
| $Ni_L$ | 9.491(7) | 4.3(1) | 5.90(7) | 2.67(7) |

Table 5.13: Comparisons of the projected magnetic saturation of the core and shell components along with the associated $\mu_{Core}$ and $\mu_{Shell}$.

So - it is clear that if this model is correct a large percentage of the total magnetisation arises from the "dead-layer" structure. In the literature the average moment per atom of Ni at a surface ranges from 0.2 to 2.0 $\mu_B$ depending on surface chemistry effects. As these materials are passivated with a thin layer of nickel oxide the chemical effects will be minimal so we will assume $\mu_{Core} \approx \mu_{bulk} = 0.61\ \mu_B$ atom$^{-1}$. The average crystallite sizes using this value and the comparable gas adsorption and XRD crystallite sizes are reported in table 5.14.

| Sample | $d_{20\%\ Corrected}$ (nm) | $d_{80\%\ Corrected}$ (nm) | $d_{Gas(Strong)}$ (nm) | $d_{XRD}$ (nm) |
|---|---|---|---|---|
| $Ni_H$ | 7.69(6) | 13.9(1) | 14.5(4) | 5.8(2) |
| $Ni_S$ | 5.90(4)(3) | 10.17(8) | 12.1(3) | 4.2(2) |
| $Ni_L$ | 5.10(6) | 8.60(8) | 7.6(2) | 3.8(3) |

Table 5.14: Comparison of the crystallite diameters as investigated via magnetisation, gas adsorption and XRD techniques.

The values The values of the crystallite size calculated assuming $\mu_{Core} \approx \mu_{bulk}$ for $Ni_H$ and $Ni_S$ lie between the boundaries defined by the XRD and gas adsorption

isotherms having assumed an average moment of 0.61 $\mu_B$ atom$^{-1}$. In the case of $Ni_L$ however, the 20 and 80% limits appear to have a slight overestimate, suggesting the moment per atom in the surface increases as the particle size decreases as was the situation for nanoparticles in the previous chapter.

### 5.3.3 Blocking temperature ($T_B$) studies

The ferromagnetic volume of the crystallites can also be measured via the variations in the low field, $M$ vs $T$ response, as was described for sample A and B in sections 4.2.5 and 4.3.5. The difference between the $M_{ZFC}$ and $M_{FC}$ behaviour can be used to deduce the distribution in blocking temperatures and, from this, the distribution in particle sizes.

For each of the three samples $Ni_H$, $Ni_S$, and $Ni_L$ magnetisation curves were recorded at $H = 100$ Oe in the temperature range 2 to 300 K after both zero field cooling ($H_{cool} = 0$ Oe) and field cooling ($H_{cool} = 10$ kOe). The resulting $M$ vs $T$ responses are shown in figure 5.14 a). In each case the difference between $M_{ZFC}$ and $M_{FC}$ is largest at low $T$ decreasing gradually as the system temperature is increased.

From the FC and ZFC data sets we can calculate the difference between the magnetic responses, $\Delta M$, as a function of the sample temperature (see the inset to figure 5.14 b)). For the distribution of blocking temperatures we are interested in the rate at which the $\Delta M$ term changes as the temperature changes - so the $\frac{d\Delta M}{dT}$. This was determined following the procedure described earlier for samples A and B (sections 4.2.5 and 4.3.5) in which a superposition of cumulative normal distributions were fitted to the data, with the associated probability distributions shown in figure 5.14 b).

At this stage we have the distribution of particle blocking temperatures, where the magnitude of $\frac{d\ M_{FC}-M_{ZFC}}{d\ T}$ at a given temperature is proportional to the volume of material unblocking in that temperature range. The issue is that in order to convert a blocking temperature to a particle volume we have to make several assumptions - including assuming a uni-axial anisotropy, a value for the anisotropy constant, the temperature dependence of this parameter, the particle morphology and whether or not the energy barrier to magnetic reversal arises from the full atomic volume or purely from the "core" structure. Of these assumptions, the Neél relaxation has been demonstrated for multiple nanoparticle samples previously,[189] so is likely to still hold, and the samples appear to have the majority of the material unblocking in a tight temperature range (5 to 40 K) suggesting any anisotropy variance

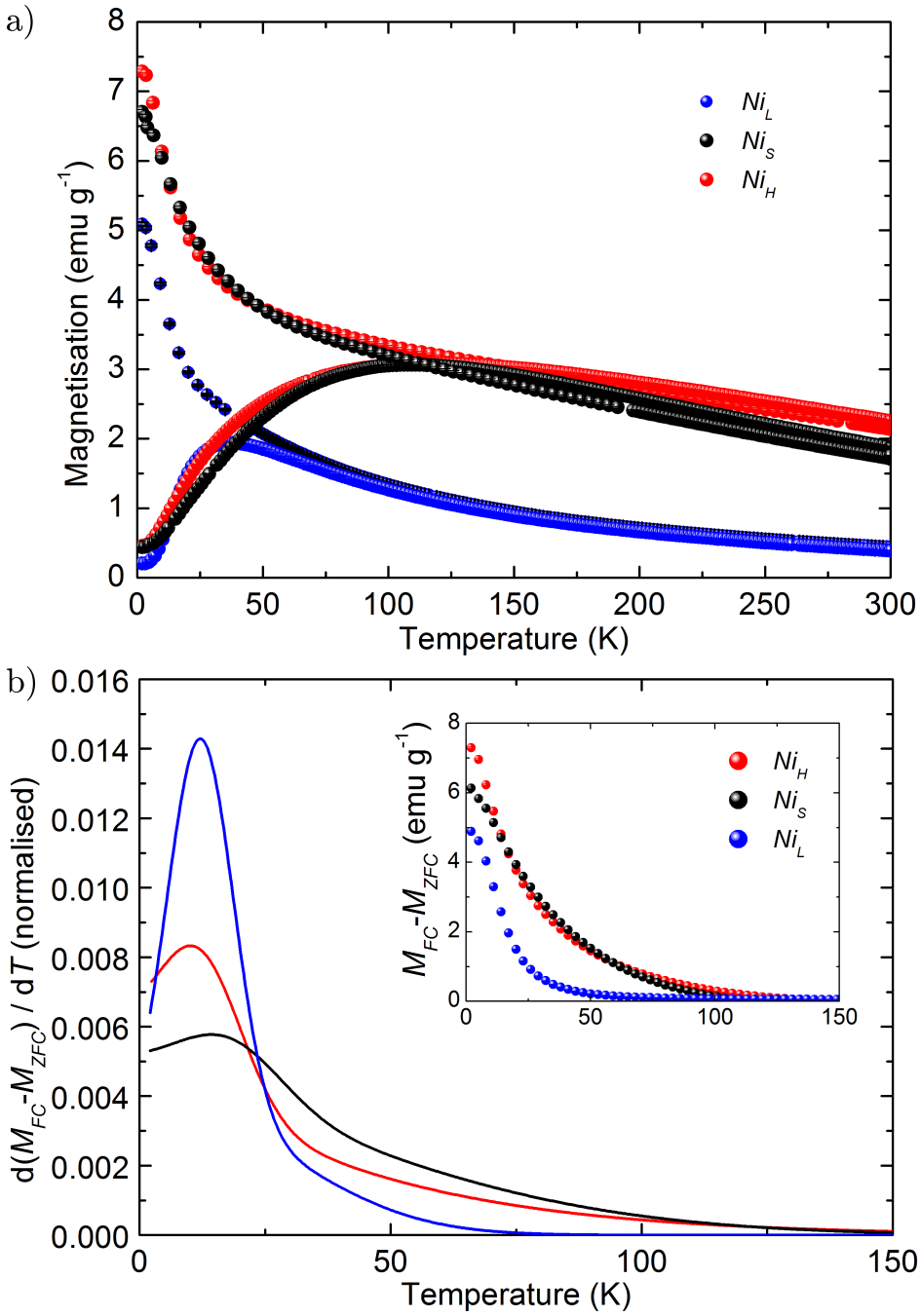


Figure 5.14: a) $M$ vs $T$ behaviour of samples $Ni_H$ (red), $Ni_S$ (black), and $Ni_L$ (blue) taken at $H = 100$ Oe after ZFC ($H_{cool} = 0$ Oe) and FC ($H_{cool} = 10$ kOe). In each case the ZFC has the lower value of $M$ at 5 K. b) Temperature differential of the difference between $M_{ZFC}$ and $M_{FC}$ as a function of temperature. Each line was determined by fitting a pair of cumulative Gaussian functions to the raw $M_{FC} - M_{ZFC}$ (shown as the inset) corrected by an offset (to allow for the trapped field difference).

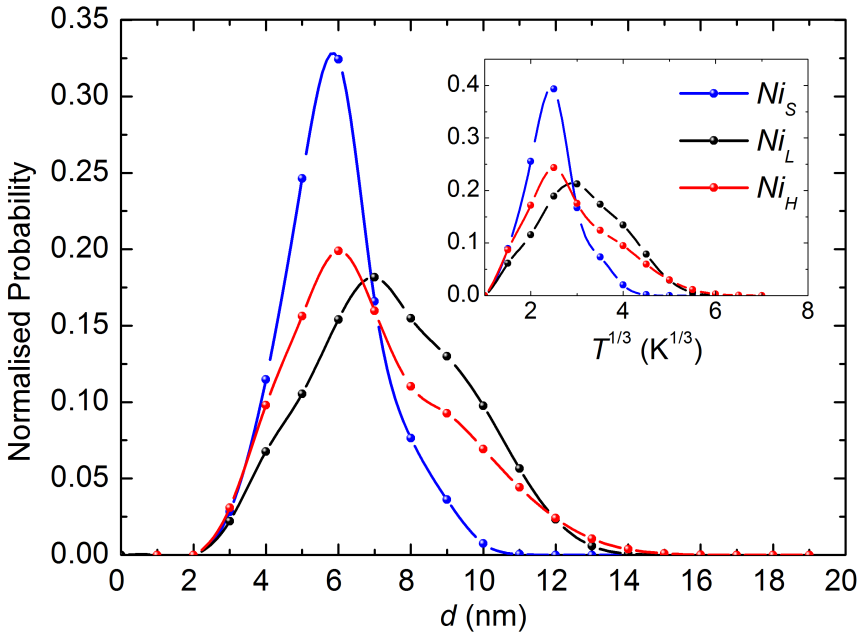


Figure 5.15: Distribution of crystallite diameters arising from the $\frac{dM_{ZFC}}{dM_{FC}}$ analysis. The data has been re-binned into equally spaced crystallite diameters for ease of interpretation.

will be small.

As was demonstrated for the NP materials in the previous chapter the value of the anisotropy constant can vary dramatically when compared to the bulk value (5,500 J m$^{-3}$) so instead we will determine an average value. Using the simplified Neél equation from section 2.2.7, the blocking temperature is related to the particle radius as described in equation 5.6,

$$r = \left( \frac{25 k_B T_B}{K} . \frac{3}{4\pi} \right)^{\frac{1}{3}}, \tag{5.6}$$

where $T_B$ is the blocking temperature and $K$ is the anisotropy constant. The inset to figure 5.15 demonstrates the $T^{1/3}$ distribution for the three samples, re-binning the data into discrete steps of 0.5 K$^{1/3}$, from which the median value of $T_B^{\frac{1}{3}}$ can be found.

Aside from finding the average blocking temperature we have also used the

20 and 80 % particle size limits from the Langevin analysis to calculate the median particle size, the values for which are repeated in table 5.15 i). Using the median values individual anisotropy constants were calculated, giving an average $K = 48(6) \times 10^3$ J m$^{-3}$. Using this value and equation 5.6 the blocking temperature distribution was converted to a diameter distribution and is shown in figure 5.15 (in comparison to the gas absorption and XRD particle sizes that are restated in table 5.15 ii) for ease of comparison).

i)

| Sample | $d_{Mag\ 20\%}$ (nm) | $d_{Mag\ 80\%}$ (nm) | $d_{Mag\ 50\%}$ |
|---|---|---|---|
| $Ni_H$ | 5.51(2) | 9.96(4) | 7.40(2) |
| $Ni_S$ | 5.2(2) | 9.09(4) | 6.93(3) |
| $Ni_L$ | 4.51(3) | 7.60(4) | 5.85(2) |

ii)

| Sample | $d_{Gas\ Strong}$ (nm) | $d_{Gas\ Total}$ (nm) | $d_{XRD}$ (nm) |
|---|---|---|---|
| $Ni_H$ | 14.5(4) | 11.5(4) | 5.8(2) |
| $Ni_S$ | 12.1(3) | 9.4(3) | 4.2(2) |
| $Ni_L$ | 7.6(2) | 6.4(2) | 3.8(3) |

Table 5.15: i) Crystallite diameters predicted from the Langevin analysis in section 5.3.1 - assuming that the two values of $\mu$ determined from the dual Langevin analysis represent the 20 and 80% points of a cumulative log normal distribution. The conversions from magnetic moment to particle diameters assume the bulk values for the magnetic moment per atom, 0.61 $\mu_B$ atoms$^{-1}$, and density, $\rho = 8.908$ g cm$^{-3}$. ii) Reiteration of the crystallite diameters calculated in section 5.2 via gas absorption and XRD.

The particle diameter and blocking temperature distributions bring to light information about the particle size distribution, which XRD and gas adsorption are relatively insensitive to, and, if our data and analysis are accurate, suggest that the crystal growth that occurs during reduction lead to two forms of particle growth. The $Ni_L$ sample (having been reduced at low $T$ for a long period of time) appears to have remained as a relatively tight particle size - with little evidence of crystallite sintering or secondary nucleation. The $Ni_L$ and $Ni_S$ samples, however, have been exposed to higher temperatures (albeit for shorter times) leading to the $Ni_S$ sample gradually increasing in size as the particle sinter, with a relatively even increase in particle size while the $Ni_L$ (which had the shortest reduction period) appears to have undergone more of a secondary nucleation step - with a slightly increased tail out to higher particle sizes.

Utilising the thermal magnetic properties in this way gives more information about the particle size distribution than the previous Langevin approach, however, it is less reliable as it only allows for magnetic moments arising from the "core" super-

| Sample | $d_{Lower}$ (nm) | $d_{Upper}$ (nm) | $d_{Lower\ Corrected}$ | $d_{Upper\ Corrected}$ |
|---|---|---|---|---|
| $Ni_H$ | 5.0(3) | 8.5(3) | 7.0(6) | 11.9(6) |
| $Ni_S$ | 4.5(3) | 10.0(3) | 5.0(5) | 11.1(5) |
| $Ni_L$ | 4.5(3) | 7.0(3) | 5.1(5) | 7.9(5) |

Table 5.16: Limits of the FWHM from the blocking temperature analysis shown in figure 5.15 alongside the values scaled for the surface contribution determined in the high $H$, $M$ vs $T$ analysis.

paramagnetic species - completely ignoring the dead layer. This is why the $Ni_S$ and $Ni_H$ samples appear to be relatively similar in size, as the extra volume of the larger $Ni_H$ particles form a thicker "dead-layer" giving the larger Curie behaviour in the high $H$, $M$ vs $T$ magnetometry analysis in section 5.3.2.

As with the Langevin analysis in section 5.3.1, the blocking temperature analysis without a dead-layer correction gives a relatively accurate reflection of the smaller particle sizes (assuming the XRD sizes reflect the lower boundary values), however, the upper particle sizes are too small. In order to try to allow for the "dead-layer" effects particle sizes will be taken from the distribution at the full width at half maxima and these sizes re-scaled for the difference in "core" and "shell" using the high $H$, $M$ vs $T$ data given in section 5.3.2. The particle sizes (corrected and un-corrected) are given in table 5.16.

The "dead-layer" corrected particle sizes now have an upper boundary consistent with the gas absorption isotherms, but the lower boundaries now overestimate compared to the XRD. The XRD and gas absorption values are expected to differ as the diffraction broadening analysis will general underestimate a particle size and gas absorption will overestimate - however, these values may also differ as they probe different physical entities. Is it possible that the nano-crystallites only possess an f.c.c. crystal structure within the "core" of the structure, with the surface states causing dislocations disrupting the crystal lattice. If this were true, the XRD broadening analysis would underestimate the average crystallite size before carrying out the "dead-layer" correction. The gas absorption technique, conversely, is purely surface sensitive and (due to the possibility of a rough surface) would give a slight overestimation of the average (dead-layer corrected) particle size.

This hypothesis serves to explain why, despite the XRD and gas absorption particle sizes varying, the magnetic studies can be taken as being in reasonable agreement with both - depending on whether or not you include a surface correction term. At present this study has been limited to one Ni catalyst preparation method, in

a relatively tight range of particle sizes, however, it has demonstrated that magnetometry can produce values of particle sizes in keeping with the current industrial methods without requiring any form of chemical treatment. Similarly, this method has shed light on the disparity between XRD and gas absorption isotherms and provides a direct measure of the catalyst size distribution (currently only achievable via cryo-TEM and hence impractical on an industrial scale).

## 5.4 Conclusions

The study of nickel crystallite catalysts detailed in this chapter serve to demonstrate that the magnetic granulometry methods outlined for nanoparticle materials in chapter 4 can be applied to steam reforming catalysts. The Langevin method, used to determine the single domain moment, was shown to under-estimate particle diameter when applied to colloidal nanoparticles and this is repeated for the catalyst materials. It appears that the XRD determined diameter and the lower boundary of the Langevin method distribution are in reasonable agreement. However, the gas adsorption determined diameter and upper-boundary of the uncorrected Langevin diameters show a marked difference, with the magnetic technique under-estimating the size.

The addition of a "shell" term, based on the low $T$, high $H$ Curie behaviour, brings the upper boundary of the Langevin analysis into closer agreement with the gas adsorption diameter. It appears that the size of the shell is dependent on the size of the crystallite, with smaller diameter particles possessing a reduced volume fraction of shell compared to the core, as was observed for the nanoparticle samples in chapter 4. This effect will also be compounded due to the variation in the average atomic moment within the shell, with a thinner outer-layer leading to a higher average moment.

This is repeated when using the blocking temperature analysis, with the crystallite sizes determined under-sizing the sample for the larger samples ($Ni_S$ and $Ni_H$) before applying the surface correction and an over-estimation of $Ni_L$ when corrected. The issue remains that the reliability of the magnetically determined crystallite size are dictated by the reliability of the techniques against which we calibrate. However, magnetometry does give an interesting alternative as data collection is rapid, does not require any chemical treatment and, as it is sensitive to volume not surface area or diameter, it possesses a superior resolution when compared to XRD or gas adsorption studies.

# Chapter 6

# Small Angle Neutron Scattering

The previous two chapters have focused on the development of a new technique for determining the crystallite size of Ni catalysts. During these experiments we have identified a magnetic reduction in the super-paramagnetic volume compared to the atomic volume which varies with sample preparation method. SANS has previously been used to investigate the magnetic and nuclear core-shell structure of nano-ferromagnetic materials[53;54;55] and will be used here, following similar procedures, to support our findings in chapter 5.

The three supported Ni samples presented in chapter 5 have been analysed via SANS measurements at the Institut Laue-Langevin in Grenoble, France on the D33 instrument. The experiment was carried out using polarised neutrons[190] with an RF-flipper to alter the incident polarisation[191] and all experiments were carried out at a neutron wavelength of $\lambda = 6$ Å, chosen to obtain the highest resolution for the expected small particles.

The neutron scattering experiments were carried out with an aim of determining the average nuclear and magnetic crystallite sizes,[53] as well as the magnitude of the magnetic moment giving rise to the magnetic scattering.[192] To achieve these aims the scattering was measured both with and without the RF-flipper, giving rise to two spin channels ($I^+$ and $I^-$) with opposite neutron polarisation, with scattering measured as a function of temperature (using a standard ILL "Orange" cryostat for thermal control) and applied field (varied using an electromagnet, rated up to $\approx 10$ kOe).

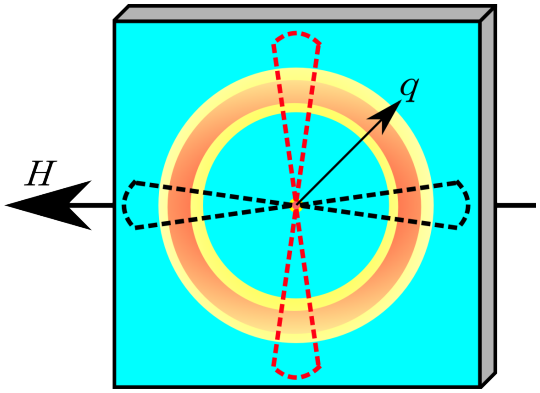


Figure 6.1: Schematic representation of the small angle scattering projected onto a 2D detector. The magnetic field, $H$, is applied horizontally. For data analysis 1D cuts are taken parallel and perpendicular to the direction of $H$, represented by the black and red dashed regions, respectively.

## 6.1 SANS experimental details

The D33 instrument [124] uses a 2D detector comprising banks of $^3$He neutron detectors producing a scattering-map centred on the sample as a function of $q$, the scattering vector, and $\theta$, the angular rotation away from the direction of the applied field (horizontal). The scattering can then be reduced into two channels, the nuclear and magnetic,[193] according to the selection rules given in equations 6.1 assuming that the magnetic moment is approaching magnetic saturation in the direction of applied field. A graphical representation of the nuclear and magnetic projections are shown on figure 6.1.

$$S(q)^{\theta=0^\circ}_{Nuclear} = \frac{I^+ + I^-}{2}, \qquad (6.1)$$
$$S(q)^{\theta=90^\circ}_{Magnetic} = \frac{I^+ - I^-}{2}.$$

## 6.2 Analysis of $Ni_H$ scattering

### 6.2.1 2D scattering maps

Typical 2D detector maps for the nuclear and magnetic spin channels for the $Ni_H$ sample discussed in the previous chapter are shown in figure 6.2. The nuclear channel

($I^+ + I^-$) demonstrates a strong scattering at low $q$, $\approx 0.01$ to $0.03$ $Å^{-1}$, gradually decreasing with increasing $q$. The random orientation of the crystallites means the nuclear scattering should have no $\theta$ dependence,[194] as seen, if the two channels have the same magnitude of magnetic scattering (but opposite in sign). The magnetic channel ($I^+$ - $I^-$) demonstrates a strongly anisotropic scattering, with an enhanced scatter at $\theta = 90°$.

The magnetic neutron cross section possesses a cross product of the neutron polarisation and the magnetic moment, so scattering will only occur when the two are perpendicular to each other.[190] The data set shown in figure 6.2 was taken at 2K and $\approx$ 10 kOe, applied in the $q_x$ axis, and the lack of scattering in the $q_x$ axis suggests the moments are saturated in this direction.[54] With evidence for the magnetic signal being saturated under these experimental conditions we can analyse the $q$ dependence.

### 6.2.2 1D cross section analysis

Figure 6.3 a) shows the cross sections of the nuclear and magnetic spin channels, taken at $\theta = 0°$ and $90°$ respectively. In comparison, Figure 6.3 b) shows the expected scattering, $S$, with increasing scattering vector, $q$, for a dilute system of mono-disperse spherical particles (the black line), using the spherical form factor given in section 3.1.6,[195] clearly showing a highly structured scattering comprising a series of minima in $S(q)$ with the $q$ position dependent on the particle size. Figure 6.3 b) also demonstrates the simulated behaviour at low and high poly-dispersity ($\sigma$ = 2% and 25% of the average particle size for the orange and green data sets respectively) with the high-poly-dispersity data set closely resembling our experimental scattering behaviour. Clearly, as the particle distribution becomes broader the local minima expected of the spherical form factor become increasingly shallow until the high $q$ region has no clear structure. The result of this loss of the "humped" behaviour is that the spherical form factor can not be relied on to give an accurate representation of the poly-dispersity of the samples - merely give a lower boundary on the spread in particle size. Similarly, fitting to a highly poly-disperse form factor can be misleading, being unable to discern between spherical, hemispherical, or cubic crystallite form factors,[196] and the resulting particle size is dependent on the assumed shape.

An alternative method for analysing particle sizes from SANS data is via the Guinier method.[122;197] The Guinier approximation only deals with low $q$ data and

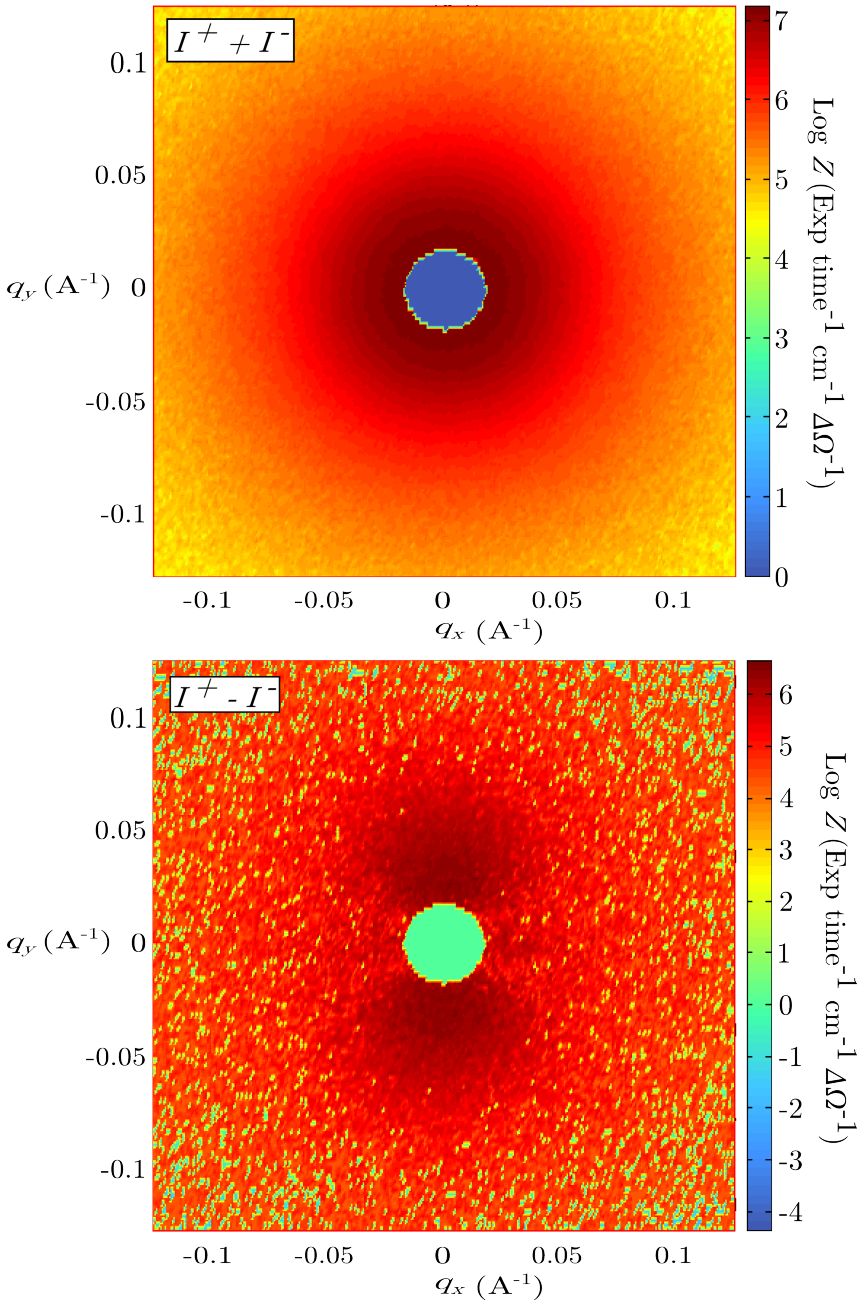


Figure 6.2: Typical 2D detector images produced from the sample $Ni_H$ of the nuclear $(I^+ + I^-)$ and magnetic $(I^+ - I^-)$ spin channels over an experiment. This data set was taken at $T = 2$ K and $H \approx 10$ kOe.

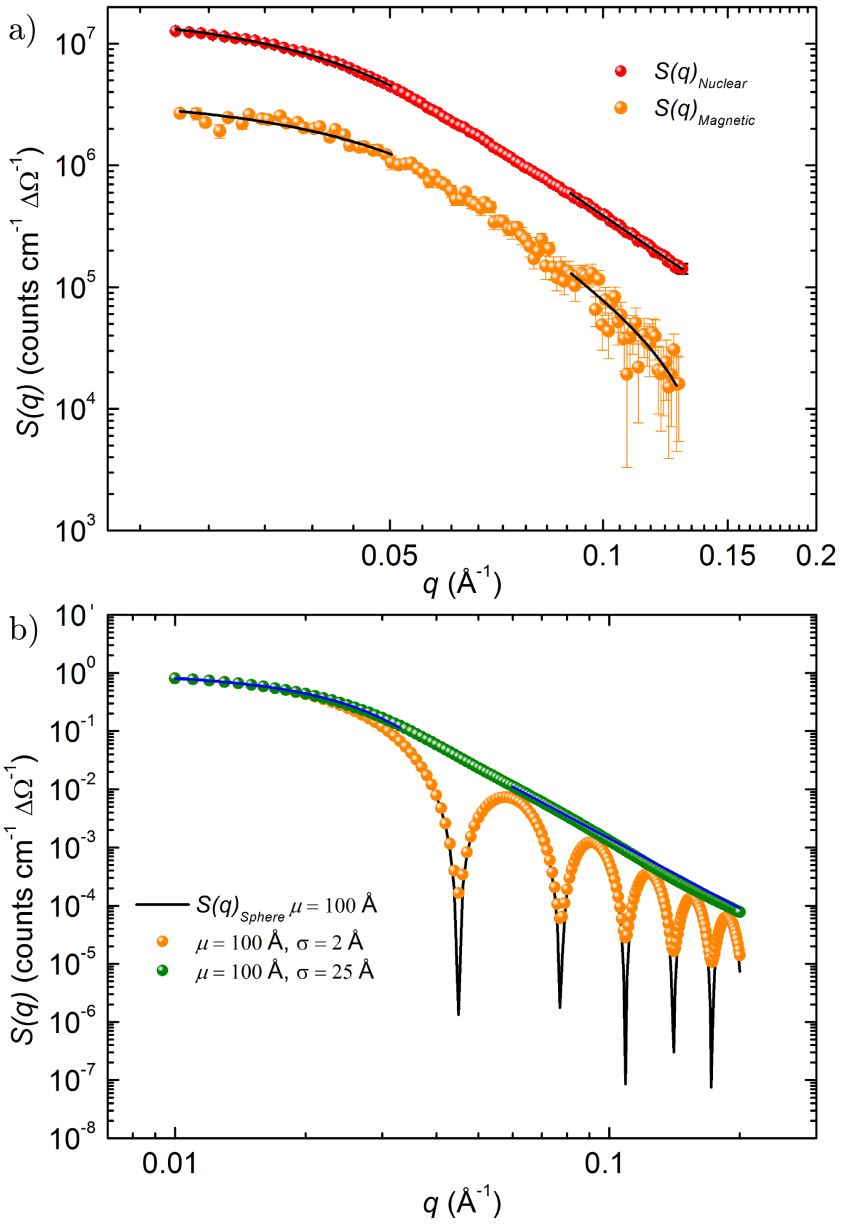


Figure 6.3: a) 1D projections of the nuclear (red, $\theta = 0°$, $I^+ + I^-$ spin channel) and magnetic (orange, $\theta = 90°$, $I^+ - I^-$ spin channel) scattering for $Ni_H$ at $T = 2$ K and $H \approx 10$ kOe. The line represents the best fit to the Guinier-Porod model given in equation 6.2. b) The simulated scattering for dilute spherical spheres based on the sphere form factor given in section 3.1.6 with average size, $\mu = 100$ Å, and increasing poly-dispersity.

| Parameter | $S_{Nuclear}$ | $S_{Magnetic}$ | Units |
|---|---|---|---|
| $R_g$ | 41.4(2) | 37.3(6) | Å |
| $k_1$ | $1.86(1) \times 10^7$ | $3.7(2) \times 10^6$ | counts cm$^{-1}$ $\Delta\Omega^{-1}$ |
| $k_2$ | 38.4(5) | 10.1(9) | counts cm$^{-1}$ $\Delta\Omega^{-1}$ Å$^4$ |
| $y_0$ | $4(4) \times 10^4$ | $-20(7) \times 10^4$ | counts cm$^{-1}$ $\Delta\Omega^{-1}$ |
| $\chi^2_{red}$ | 1.41 | 1.13 | |

Table 6.1: Best fit parameters of the Guinier-Porod model to the nuclear and magnetic data for sample $Ni_H$ as shown in figure 6.3 a).

depends on the radius of gyration (based on particle morphology, and affected by both shape and size). As the Guinier method only holds at low $q$ the fitted value for the background count rate is unreliable, however, the high $q$ data may follow the Porod approximation.[198] Combining the two approximations into a Guinier-Porod approximation (see equation 6.2) we can fit the low $q$ and high $q$ data sets simultaneously with a shared value for the count background.

$$S(q) = \begin{cases} k_1 e^{-\frac{q^2 R_g^2}{3}} + y_0 & \text{low } q; \\ k_2 q^{-4} + y_0 & \text{high } q. \end{cases} \tag{6.2}$$

The Guinier-Porod method was tested on the high poly-dispersity data set in figure 6.3 b) producing the black line of best fit. The model closely reproduces the low $q$ data and predicts an average radius of gyration, $R_g = 77.1(1)$ Å. The conversion between radius of gyration and atomic radius, $R$, is dependent on the particle shape however for a sphere $R^2_{Sphere} = \frac{5R_g^2}{3}$. Using this conversion predicts an average particle size of 99.5(1) Å - within 1 Å of the simulated size, suggesting the Guinier-Porod approach is relatively reliable.

The Guinier-Porod approach has been applied to the nuclear and magnetic scattering taken at $T = 2$ K, $H \approx 10$ kOe, and is shown as the accompanying pairs of black lines, at high and low $q$, to figure 6.2 with the associated best fit parameters in table 6.1. The magnetic scattering channel appears to be reproduced well by the Guinier-Porod approach with both $q$ ranges fit accurately and a value of $\chi^2_{red}$ approaching 1. The nuclear channel has a slightly increased $\chi^2_{red}$ and, on inspection of the residual, the fit diverges most at the lowest $q$. A drawback with the Guinier-Porod approach is that it does not allow for inter-particle scattering,[199] which will happen over longer distances and hence at the lowest $q$ range, possibly explaining a small divergence. However, it does not appear to be a large effect so the values predicted by the Guinier-Porod approach are reasonably reliable.

The Guinier-Porod approach has produced a difference between the magnetic and nuclear radius of gyration, $R_{g\ Nuclear} = 41.4(2)$ Å and $R_{g\ Magnetic} = 37.3(6)$ Å respectively. If we assume a near spherical morphology these values would convert to a spherical radius, $R_{Nuclear} = 53.4(3)$ Å and $R_{Magnetic} = 48.2(8)$ Å suggesting an outer layer of $\approx \frac{1}{2}$ nm, on the scale previously reported. This difference between the magnetic and nuclear scattering mirrors the behaviour seen during the magnetisation analysis in section 5.3.1 in which the core, "super-paramagnetic" moment was surrounded by a shell of moments. During the magnetisation experiments we observed this magnetic shell had a lower susceptibility, due to the reduced magnitude of the magnetic moments, compared to the core moment and hence would not be fully saturated at $H \approx 10$ kOe and as a result be unobserved in the coherent magnetic scattering.

### 6.2.3 The effect of applied field and temperature on SANS studies

Aside from observing the difference between the magnetic and nuclear $R_g$ the polarised SANS study can also serve as a magnetometer tuned to the core magnetic moment. At $q = 0$ the intensity of the nuclear scattering is proportional to the scattering length of nickel (10.3 fm)[200] and the intensity of the magnetic scattering is proportional to the magnetic moment on the scattering atom. Hence, from the ratio of $k_{1\ Nuclear}$ and $k_{1\ Magnetic}$, we can follow the magnetic properties of the core species.

Figure 6.4 shows the effect of applied field on the ratio between the projected $S_{q=0}$ for the magnetic and nuclear scattering channels at $T = 300$ K. During the experiment the applied magnetic field was varied using an electromagnet - varying the current in order to vary the applied field. During the experiment the effective applied field was measured at the surface of the cryostat using a Hall probe/Gauss meter at various current settings (the result of which is plotted as the inset to figure 6.4 a)). The scattering ratio, $S(0)_{Ratio} = \frac{S(0)_{Magnetic}}{S(0)_{Nuclear}}$ shows a growth in the strength of the magnetic channel as the applied field was increased, approaching 0 at the lowest applied field and $\approx 0.156(9)$ at high field.

As well as having a $H$ dependence the crystallite magnetisation also identified a strong $T$ dependence, however, at high $H$ we only assigned a Bloch's law behaviour to the super-paramagnetic species.[201] If we are not observing scattering from the outer layer of magnetic material it will not be included in the $S(0)$ thermal behaviour. Figure 6.4 b) shows the effect of temperature on the $S(0)$ ratio, fit by Bloch's law

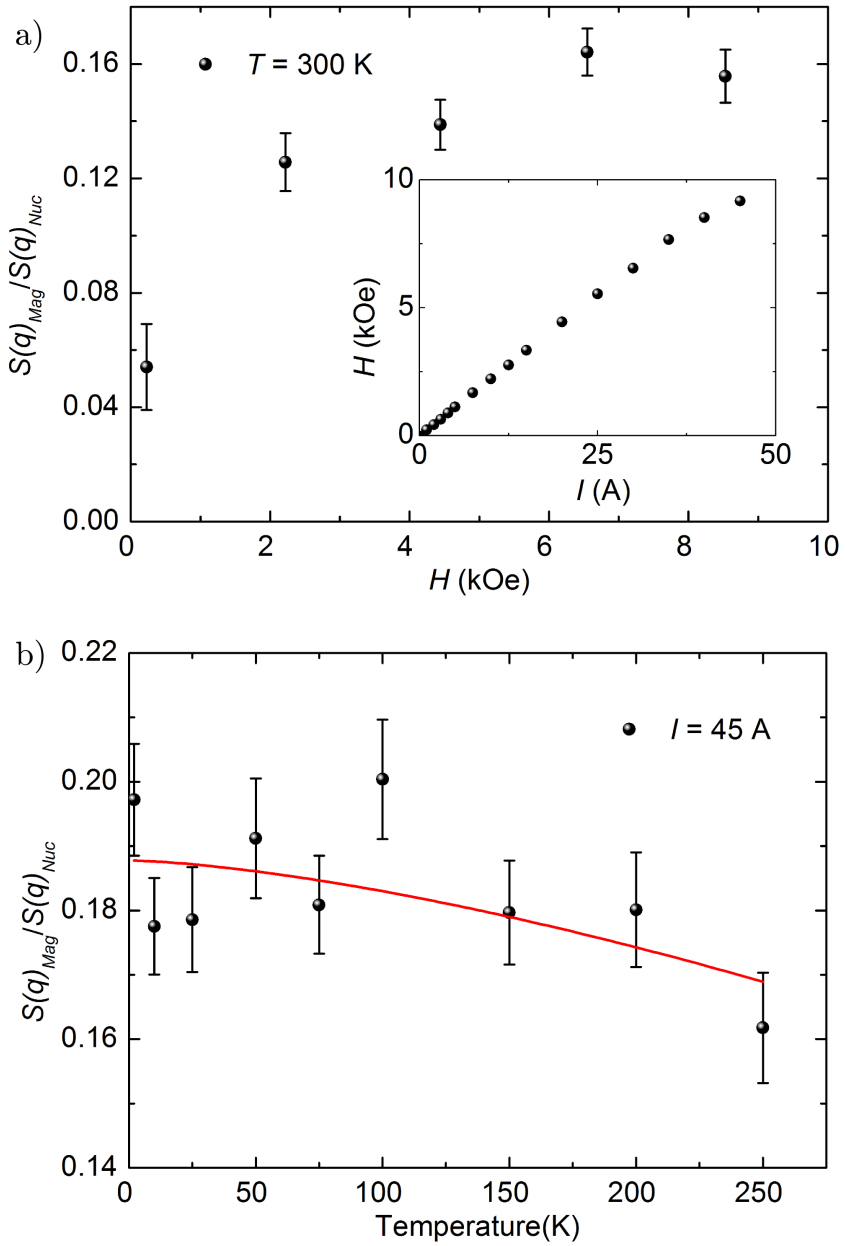


Figure 6.4: The effect of a) applied field, and b) temperature on the ratio of magnetic to nuclear scattering projected to $q = 0$ Å$^{-1}$. Inset - current to magnetic field behaviour of the electromagnet utilised during the SANS measurements.

for low $T$ spin waves,

$$\frac{M}{M_S} = 1 - \alpha T^{\frac{3}{2}}. \tag{6.3}$$

The large error bars and the weak temperature dependence within this region makes it difficult to be certain about the temperature dependence and is reflected in a large error bar for the value of $\alpha = 2(1) \times 10^{-5}$ K$^{-\frac{3}{2}}$, however, we do not see the same Curie behaviour evident in magnetometry studies and the value of $\alpha$ is consistent with the value deduced earlier ($1.02 \times 10^{-5}$). The fit has a reasonable $\chi^2_{red} = 1.33$ and predicts the $S(0)_{Ratio} = 0.188(4)$.

As well as following the change in the ratio at S(0) each SANS measurement also provides values of the nuclear and magnetic $R_g$. Interestingly, the data shows no temperature dependence, suggesting that the previously reported thermal contraction of metallic nanoparticles has no effect here,[202;203] and the data sets can be used together to give average values, $R_{g\ Nuclear} = 41.12(5)$ Å and $R_{g\ Magnetic} = 34.9(5)$ Å.

The magnetic neutron scattering length, $b_m$, can be related to the size of the magnetic moment on the species, $\mu$, by the equation

$$|b_m| \approx \gamma r_0 F(Q) |\mu|, \tag{6.4}$$

where $r_0$ is the electron radius ($2.82 \times 10^{-15}$ m), $\gamma$ is the gyromagnetic radius ($\approx 2$) and $F(q)$ is the magnetic form factor ($F(0) = 1$ and $F(\infty) = 0$). If we assume that the nuclear Ni scattering has the same coherent scattering length as bulk Ni (10.3 fm) then the ratio $\frac{S(0)_{Magnetic}}{S(0)_{Nuclear}} \approx 0.548|\mu|$ when the magnetisation is saturated. Using the value of $S(0)_{ratio}$ deduced from the $H \approx 10$ kOe data set this predicts an average moment $\mu = 0.34(1)\ \mu_B$ atom$^{-1}$, a reduction compared to the bulk value assumed of 0.61 $\mu_B$ atom$^{-1}$. However, this value does not take into account the different scattering volumes (reflected by the difference in $R_g$) which once corrected for increases the average moment to $\mu = 0.58(4)\ \mu_B$ atom$^{-1}$ much closer to the bulk value of Ni.

## 6.3 Analysis of $Ni_S$ and $Ni_L$ scattering

Following the same procedure the nuclear and magnetic scattering have also been measured for the $Ni_S$ and $Ni_L$ samples.

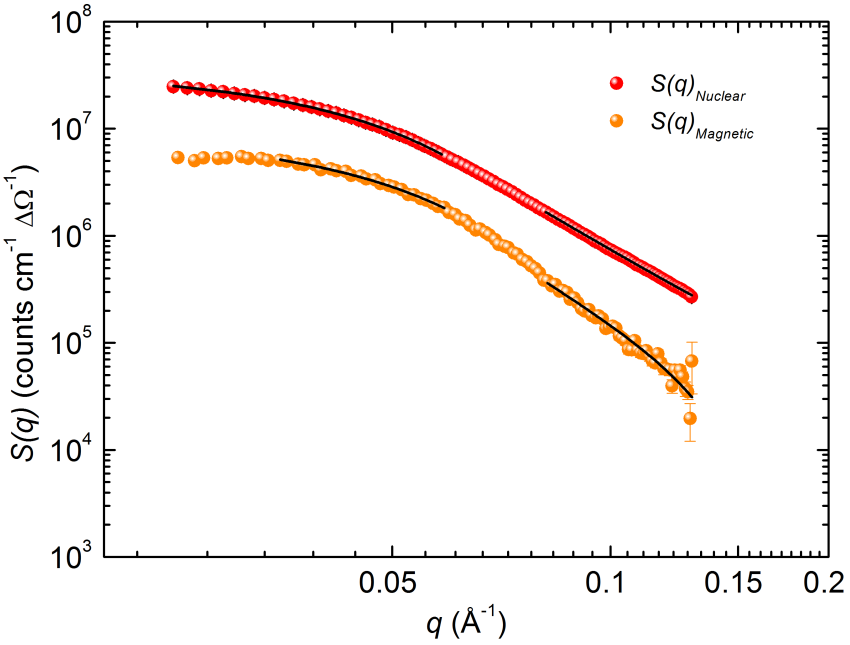


Figure 6.5: Typical 1D projections of the nuclear (red) and magnetic (orange) scattering for the $Ni_S$ sample taken at $T = 10$ K, $H \approx 10$ kOe. Both data sets have been fit by the Guinier-Porod model (black lines) with the best fit parameters given in table 6.2.

### 6.3.1 1D cross section analysis

Figure 6.5 shows the nuclear and magnetic scattering channels for the supported Ni catalyst $Ni_S$ taken at $T = 10$ K and $H \approx 10$ kOe. As with the previous sample the wide poly-dispersity of the samples means that the high $q$ structure of the form factor has been smeared into a continuous Porod behaviour, so the Guinier-Porod approximation will have to be relied upon to evaluate the crystallite size.

The black lines on figure 6.5 represent the best fit to the Guinier-Porod model previously described with the associated parameters listed in table 6.2. The Guinier-Porod model gives a reasonable reproduction of the SANS data, with a $\chi^2_{red} \approx 1$ in both cases, however, in order to achieve this the lowest $q$ region of the magnetic scattering channel has had to be excluded from the fit.

The Guinier-Porod model implies a higher scattering count in the low $q$ region than has been measured, suggesting there are features which are excluded from

| Parameter | $S_{Nuclear}$ | $S_{Magnetic}$ | Units |
|---|---|---|---|
| $R_g$ | 39.66(4) | 36.9(2) | Å |
| $k_1$ | $3.460(8) \times 10^7$ | $9.02(1) \times 10^6$ | counts cm$^{-1}$ $\Delta\Omega^{-1}$ |
| $k_2$ | 72.4(2) | 17.6(4) | counts cm$^{-1}$ $\Delta\Omega^{-1}$ Å$^4$ |
| $y_0$ | $2.2(1) \times 10^4$ | $-3.1(3) \times 10^4$ | counts cm$^{-1}$ $\Delta\Omega^{-1}$ |
| $\chi^2_{red}$ | 1.14 | 1.61 | |

Table 6.2: Best fit parameters of the Guinier-Porod model to the nuclear and magnetic data of sample $Ni_S$ shown in figure 6.5.

the Guinier approximation. Such a feature is possibly a result of inter-particle interactions (occurring at low $q$ the feature needs to be associated with a long range scattering event) or a result of a core-shell structure. However, due to the high polydispersity of the sample this feature is too widely spread to be thoroughly understood in this study.

The radius of gyration values determined from the fitting show a slight reduction in $R_{g\ Nuclear}$ compared to the $Ni_H$ sample by $\approx 2$ Å - less than is to be expected from the previous gas adsorption and XRD peak broadening analysis. Interestingly, the difference between the magnetic and nuclear $R_g$ terms has decreased - mimicking the decreased shell magnetic contribution observed for the $Ni_S$ sample compared to the $Ni_H$ sample during magnetometry investigations in chapter 5.3.1.

### 6.3.2 The effect of applied field on SANS studies

As with the previous sample the relative strength of the core magnetisation can be expressed as a function of the applied magnetic field by following the change in the projected $S(0)$ scattering as a function of applied field. Figure 6.6 shows the change in the $S(0)$ ratio for the $Ni_S$ and $Ni_L$ samples as a function of applied field, suggesting a saturation of the core magnetic species at fields above $\approx 5$ kOe. Interestingly we again see no evidence of the smaller moment magnetic species believed to make up the outer shell structure - suggesting that the magnetic moments are randomly aligned and hence do not add to the coherent magnetic scattering.

As well as calculating the S(0) ratio, each data set also furnishes a value of the magnetic and nuclear radius of gyration terms, the average values for all three samples are summarised in table 6.3 for ease of comparison. Comparison of the nuclear $R_g$ values clearly shows that the samples do descend in atomic size $Ni_H$ to $Ni_S$ to $Ni_L$, in agreement with the order predicted by XRD and gas absorption studies, however, the magnetic $R_g$ do not follow the same behaviour. As was seen in the pre-

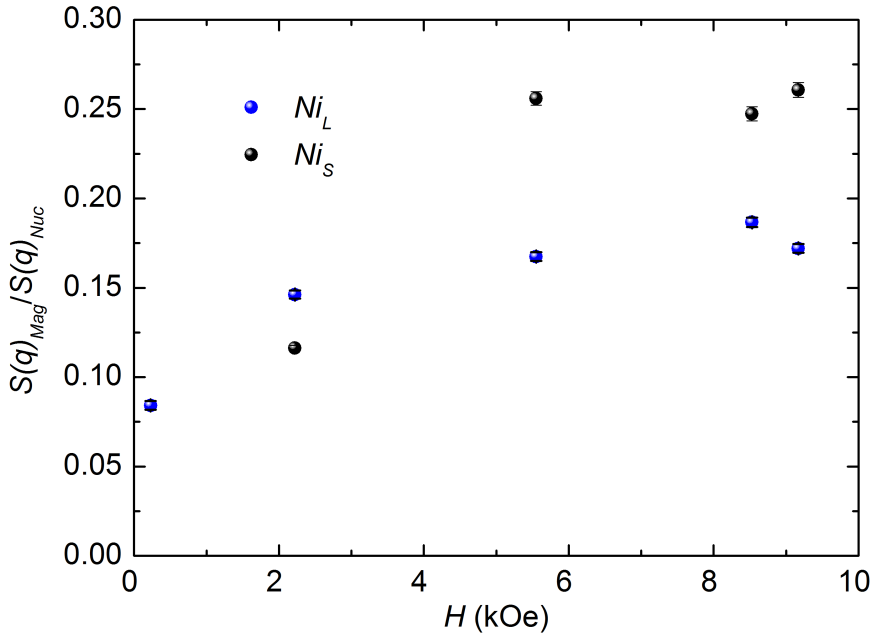


Figure 6.6: Effect of applied field on the ratio of magnetic to nuclear scattering for sample $Ni_S$ (black) and $Ni_L$ (blue) projected to $q = 0$ Å$^{-1}$.

| Parameter | $R_{g\ Nuclear}$ | $R_{g\ Magnetic}$ | Units |
|---|---|---|---|
| $Ni_H$ | 41.12(5) | 34.9(5) | Å |
| $Ni_S$ | 39.62(5) | 37.2(3) | Å |
| $Ni_L$ | 36.0(3) | 31.0(1) | Å |

Table 6.3: Summary of the radius of gyration for the nuclear and magnetic scattering analysis for catalyst samples $Ni_H$, $Ni_S$, and $Ni_L$.

vious chapter in the $M$ vs $T$ behaviour the $Ni_H$ sample appears to have a smaller magnetic volume than the $Ni_S$ sample despite its larger nuclear volume - giving it a smaller "core" super-paramagnetic moment and meaning more of its magnetisation resides in the outer magnetic "shell' structure. The $Ni_S$ sample follows a similar behaviour, with a smaller nuclear and magnetic $R_g$ than the other two materials, and a shell thickness $\approx$ half way between the other two. Interestingly, the $R_g$ values show a smaller range than the gas absorption and XRD values found in the previous chapter, a fact mirrored in the $M$ vs $T$, blocking temperature analysis, in which the thee samples appeared to have a comparable average size but a stronger variation in the extremities of the distribution.

Taking the average of the $S(0)$ ratio, assuming above $H = 5$ kOe the "core" magnetic species is saturated at $T = 10$ K, we get saturation ratios, $S_{Sat.\ Ni_S} = \frac{S(0)_{Magnetic}}{S(0)_{Nuclear}} = 0.255(3)$ and $S_{Sat.\ Ni_L} = 0.175(2)$. Following the previous method the saturation ratios can be converted to average moments of $\mu = 0.471(5)$ and $0.319(4)$ $\mu_B$ atom$^{-1}$ for the $Ni_S$ and $Ni_L$ samples respectively. Clearly, these values are both greatly reduced compared to the bulk average ($0.61$ $\mu_B$ atom$^{-1}$) and inconsistent with each other and the previous $Ni_H$ sample. Carrying out the volume correction (correcting for the difference in atomic volume of scattering between the magnetic and nuclear using the $R_g$ terms) give corrected average moments $\mu = 0.57(2)$ and $0.51(2)$ $\mu_B$ atom$^{-1}$ for the sample $Ni_S$ and $Ni_L$ respectively, bringing the three values into closer agreement with the bulk value and each other.

## 6.4 Conclusions

The SANS measurements presented here add credence to our hypothesis that the catalyst crystallites exist as a core-shell structure, in which the core exists as a super-paramagnetic moment with a volume reduced from the nuclear structure. The thickness of the shell, however, does not appear to have a clear dependence on either the change in particle size or degree of reduction.

| Parameter | SANS ratio | Magnetic ratio |
|---|---|---|
| $Ni_H$ | 0.58(4) | 0.366(2) |
| $Ni_S$ | 0.82(2) | 0.714(4) |
| $Ni_L$ | 0.64(2) | 0.688(5) |

Table 6.4: Summary of ratios between the volumes of the core and total particle as found via SANS and magnetometry (see chapter 5). For the SANS values this is the ratio of $(\frac{R_{g\ \text{Magnetic}}}{R_{g\ \text{Nuclear}}})^3$ and for magnetic value the ratio between $\frac{V_{\text{Core}}}{V_{\text{Core}}+V_{\text{Shell}}}$.

A direct comparison between the SANS $R_g$ value and the magnetically determined particle sizes is not viable, as we cannot be certain of the crystallite morphology. However, if we assume that the magnetic and nuclear scattering bodies have the same shape, then the SANS volume ratio, $R_{g\ \text{Magnetic}}^3 : R_{g\ \text{Nuclear}}^3$, should be proportional to the core:shell volume ratio found in chapter 5, $V_{Core} : V_{Core} + V_{Shell}$, (these ratios are shown in table 6.4). Clearly, these ratios are not equal, however, they follow a similar behaviour, with the largest shell contribution coming from $Ni_H$ (largest sample, highest degree of reduction) and followed by $Ni_L$ (smallest sample, lowest degree of reduction). The issue here is that this analysis assumes that the magnetic core morphology is dictated by the particle shape - but this may not be true. The core super-paramagnetic moment could easily be cubic within a spherical particle or spherical within a cubic particle, rendering our previous assumption incorrect, and leading to a systematic error in our $R_g$ ratio.

Aside from giving evidence for a reduction in magnetic volume compared to the nuclear volume of the catalysts, the SANS experiments have also giving a value for the average moment per atom within the core-structure (once scaled for the relative quantity of scattering bodies). We have assumed previously that the core nickel would have a moment per atom comparable to bulk (0.61 $\mu_B$ atom$^{-1}$), in comparison to other papers in which a reduction in Ni moment is used to explain the decrease in magnetisation from the Langevin analysis that we have assigned to the core shell structure. Finding an average moment in the range 0.5 - 0.6 $\mu_B$ atom$^{-1}$ for each sample suggests there may be some competition between both factors - with the smallest sample having the lowest predicted moment ($Ni_L$ = 0.51 $\mu_B$ atom$^{-1}$ compared to $\approx 0.58$ for the $Ni_S$ and $Ni_H$ samples).

In attempting to apply magneto granulometry methods to catalysts we have introduced a vast range of extra variables, including variations in degree of reduction, crystallite support interactions, and crystallite morphology, on top of the already competing surface driven, and inter-particle interactions. In attempting to explain

the crystallite behaviours fully, and be able to predict with accuracy the change in behaviours from one system to anther, we would need samples with controlled variations in surface contributions, finite size effects on both the core and shell average moment and intercalation of other elements e.g. oxygen, representing a level of synthetic design impractical for catalytic materials. However, we have outlined the techniques, principles, and analysis methods by which these features can be studied if both a wide range of control samples were available and the time for analysis feasible.

The SANS studies presented in this chapter support our hypothesis that each crystallite consist of two distinct regions, behaving as a core of single domain ferromagnetic material that approaches saturation at $H \approx 10$ kOe for $T$ on the order of 100 K surrounded by a shell of atoms. Unlike the magnetic studies in which this shells magnetisation has been explored, the lower $H$ available for SANS measurements have meant that the behaviour of this shell can not be identified. However, this dual region structure does suggest our addition of a surface driven magnetic term to the existing Langevin and blocking temperature based granulometry approaches is based on a measurable feature of the particle.

# Chapter 7

# Summary and Conclusions

This thesis has dealt with the development of the magnetic granulometry methods first outlined by Elmore[34] in 1931 for the study of the single-domain, superparamagnetic moment that arises when a ferromagnetic material is reduced to the nano-scale. Modelling the magnetic susceptibility via a Langevin function has long been relied upon to determine the average particle moment,[36] assuming that every atom adds to this super moment. Motivated by a number of studies in which the surface magnetic states have been demonstrated to disconnect from the central moment,[97;96] we aimed to develop a correction term that would account for this magnetic contribution, and produce a particle sizing technique which is reliable, accurate and rapid for application by Johnson-Matthey to heterogeneous catalysts in an industrial setting.

## 7.1 Summary

The experimental content of this thesis begins with the synthesis and study of a range of colloidal Ni nanoparticles, with the aim of studying their magnetic properties as a simplified analogue of the heterogeneous catalyst materials. By varying three synthesis parameters (temperature of reduction, surfactant composition, and Ni precursor loading) 4 samples were synthesised, with TEM confirming the particle diameters span the range 7 to 25 nm. The largest of the sample diameters was achieved by removing the trioctyl phosphine (TOP) surfactant, relying on a purely oleyl amine (OA) system, which also lead to the widest polydispersity. The TEM studies also revealed that the samples would readily self-assemble on evaporation into a hexagonally ordered colloidal crystal structure.

The magnetic studies of the colloidal nickel nanoparticles are outlined in section 4 and served to demonstrate that, for surfactant stabilised nanoparticles with a range of average diameters and poly dispersity, while the Langevin function (allowing for a polydisperse sample) can reproduce the magnetisation as a function of applied field at high $T$ the moment single domain moment is reduced compared to the TEM-imaged size. The magnetic behaviour, however, was not adequately described by the existing theories (the Langevin function at high $T$ and the Stoner-Wohlfarth model at low $T$). The low $T$ magnetic susceptibility behaviour showed a marked increase in magnetic saturation beyond that associated with the saturated Langevin functions, manifesting as a Curie tail behaviour on top of the expected decrease in magnetisation with increasing $T$ at high $H$ associated with the creation of spin-waves.

The low $T$, high $H$ magnetisation was well modelled by a super-position of Bloch's law (allowing for the saturated single-domain moment) with a Curie Weiss modified Langevin function to describe the Curie behaviour. This model was interpreted as the core manifesting as a saturated single-domain structure, which at high $T$ exhibited the Langevin behaviour associated with nano-ferromagnetic materials, and the particle shell splitting into multiple micro-cluster (of 5 - 10 $\mu_B$) where within the cluster the moment are ordered ferromagnetically but experience a correlation between the nearest neighbours and single domain core, which can be either ferromagnetic or antiferromagnetic. Such a situation can be likened to the case previously reported for ferrite nanoparticles,[97;96] which manifested as a single-domain core surrounded by a spin-glass shell structure of multiple magnetic moments.

The use of the high $H$, $M$ vs $T$ data sets allows for the thickness of the shell structure to be approximated due to the relative quantity of the particle magnetisation arising from the core or shell, and from this difference scale the total particle volume appropriately. This approach demonstrates that the average moment in the shell structure appears to be linked to the size of the particle, with a decrease in radius leading to a thinner shell and an increased moment per atom ($\approx 1.2\ \mu_B$ atom$^{-1}$) in comparison to the bulk value (0.61 $\mu_B$ atom$^{-1}$). However, assuming the shell moment is equal to the bulk only led to a difference of $\approx 2$ nm between magnetic and TEM sizes, cf. 3 - 10 nm without the shell term.

The magnetic studies of the nanoparticles required that the particles be dispersed in a media with a low magnetic background in order to minimise the colloidal crystal self assembly, which would lead to a close inter-particle distance and hence strong dipole-dipole interactions. To this end, the nanoparticles have been dispersed

in a commercially available fluorinated grease, Fomblin - chosen over other greases for its low diamagnetic contribution, lack of paramagnetic impurities, ready availability and non-conductive nature, removing possible RKKY interactions.

The magnetic approaches outlined for the nano-particle materials have been applied to a series of steam reforming nickel catalyst as a model for JM process technologies heterogeneous catalyst materials. The same behaviour has been identified in which the Langevin analysis underestimates the size of the single domain core structure, and the low $T$, high $H$ magnetic susceptibility demonstrates a growth in magnetisation akin to a modified-Langevin function superimposed on Bloch's law.

Using the high $H$, $M$ vs $T$ data sets the individual magnetic contributions from the core (Bloch's law) and surface (modified-Langevin) can be projected to saturation, and hence the crystallite volumes scaled. Carrying out this surface correction brings the expected crystallite sizes in line with the sizes predicted from the two most used industrial sizing techniques, gas adsorption isotherms and XRD analysis. These two techniques are known to overestimate and underestimate, respectively, the particle sizes of crystallites and as a result are treated as a window for agreement. The magnetic analysis determines the 20% and 80% limits of the cumulative distribution which, in the case of the larger crystallite systems, are in good agreement with the average of the XRD and gas values, once the particle volume has been scaled for the shell effect seen in the high $H$, $M$ vs $T$ data sets, assuming the bulk moment per atom. The sample with the smallest diameter (as determined from XRD, gas adsorption and magnetic measurements) appears to be overestimated by $\approx 1$ nm, likely a result of the increased moment per atom seen for smaller samples in the nanoparticle section, but this is a small error in comparison to the reliability of the industrial techniques.

Aside from the Langevin method, the particle volume distributions have also be determined via the "blocking temperature" method utilising the low $H$, $M$ vs $T$ data. This method has suffered from the same issues as the uncorrected Langevin analysis, underestimating the larger crystallite preparations. Correcting for the core-surface scaling removes this issue giving good agreement between the particle size distribution and the particle sizes determined from XRD and gas adsorption techniques.

The heterogeneous catalyst samples were finally investigated using SANS using polarised neutrons in order to compare the magnetic and nuclear scattering volumes. The catalysts showed a similar behaviour in terms of the nuclear volume being larger than the magnetic volume, with values of the average moment per atom

within the core similar to the bulk value of Ni, confirming the presence of a shell structure on top of the single ferromagnetic domain. The SANS studies were carried out at fields below 10 kOe throughout, under which conditions the surface magnetic contribution is relatively weak, meaning the scattering could not be de-convolved from the core to analyse the magnetic behaviour of the surface but confirming the presence of a shell.

## 7.2 Further Work

In order to further the studies presented it would be of particular interest to explore the variation in the magnetic properties of the catalysts at different stages of the industrial process. The creation of multiple surface states, including carbides and varying oxide levels, alongside measurement of the nuclear particle size variation to allow for sintering and agglomeration, would allow for analysis of possible routes to catalyst deactivation (e.g. "coking") and the methods by which these can be followed magnetically. Unfortunately, the industrial reactors can have catalysts on-stream for months at a time, meaning that we would need to have understood the protocols for analysing the materials far earlier in time to expand on this work here.

Aside from these studies, it would be of interest to expand this work to include a range of Co particles. Nickel was chosen for this thesis as the lower anisotropy constant of the bulk material implied a larger range of super-paramagnetic particle sizes would be achievable within our experimental set up, however, cobalt is an interesting alternative for investigation. As mentioned earlier, Co/CoO is a well understood exchange biased material[56] in which the quantity of CoO can be used to tune the shift in coercivity at low temperatures. A study of a range of Co Fischer Tropsch catalysts - applying the methods described here to quantify the metallic cobalt core-shell structure alongside the shift in coercivity caused by the exchange biasing could illustrate the thickness of CoO - identifying if the shell structure encompasses the oxide or if the layer adds a separate magnetic and physical term.

Aside from these studies, the industrial applicability of the work means that the reliability of the technique will need to be addressed. In these studies the nanoparticle systems had a high homogeneity, meaning that relatively small samples closely reflected the bulk average, and large catalyst extrudites were studied in order to avoid sampling bias. In many heterogeneous systems the catalysts will have a large spread of physical properties (e.g. crystallite diameter, degree of reduction, or loading) at different positions of the catalyst bed. Hence, it would be important

to evaluate the number of catalyst extrudites required for analysis in order to arrive at a general picture, be it an overall average or a shift in behaviour at different positions. This study is similar to the downside of TEM, that imaging a small region may not be reflective of the bulk, on a larger scale. This work would also inherently involve the study of a wider range of particle diameters, following sintering at different positions of the catalyst bed, as well as a wider range of support materials, with variation of both the chemical properties (investigating silica and titania supports) and physical properties (investigating the effect of different support porosities and variation in metal-support interactions).

The final study that we would recommend is a return to the SANS measurements. In the studies reported here, the catalysts have a relatively wide polydispersity - resulting in the data being limited to a radius of gyration analysis. If a catalyst system with a tighter size distribution could be synthesised, it would allow for the SANS data (both magnetic and nuclear) to be assigned to either a spherical, hemispherical or cubic morphology. This would identify both the catalyst shape on the support (difficult due to the limitations of TEM) and determine the core-shell structure in terms of magnetic contributions, adding to the understanding of the "glassy" surface behaviour.

## 7.3 Conclusions

In conclusion, this thesis has demonstrated a series of magnetic measurement protocols, based on the Langevin magnetic susceptibility and Neél thermal barrier, which allow for the study of industrially viable catalytic materials. Building upon previous work in the field, we have identified a method for quantifying the thickness of the nanoparticle shell which is decoupled from the central single-domain core and demonstrated a magnetisation dependent on particle diameter. As an industrial sizing technique, a perfect value of particle size may not always be available to calibrate against and, as such, we have demonstrated that an assumption of bulk behaviour leads to a systematic error in particle accuracy of $\pm 2$ nm - an improvement on the error demonstrated without the surface correction (3 to 10 nm, increasing with a larger particle diameter).

Alongside the main findings of this work we have also demonstrated the effect of three synthesis parameters (reduction temperature, surfactant system composition and nickel loading) on the resulting average particle diameter and the polydispersity of the diameter distribution as well as identifying Fomblin grease as a readily

available media for the dispersion of nanoparticles for magnetic studies.

The analysis of the catalyst crystallites via these methods have laid the foundations for the industrial use of magnetometry methods for the analysis of catalysts within Johnson-Matthey. The methods outlined have the advantage over the current techniques in that it furnishes information on the crystallite size distribution, either the 20% and 80% limits for the corrected-Langevin approach or a full radial distribution for the corrected-blocking temperature method, while remaining relatively insensitive to the support materials, requiring short time scales ($\approx$ 8 hours for data collection) and a simple sample preparation method (in comparison to TEM).

# Bibliography


[1] C. Bartholomew and R. Farrauto, *Fundamentals of Industrial Catalytic Processes* (Wiley, New Jersey, USA, 2011).

[2] R. Sheldon, I. Arends, and A. Dijksman, Catal. Today **57**, 157 (2000).

[3] J. Mlynarski and S. Bas, Chem. Soc. Rev. **43**, 577 (2014).

[4] K. P. de Jong and J. W. Geus, Catal. Rev. **42**, 481 (2000).

[5] Johnson-Matthey, *Johnson-Matthey annual reports & accounts* (2013).

[6] F. Fischer, Ind. Eng. Chem. **17**, 574 (1925).

[7] J. Vanhook, Catal. Rev. **21**, 1 (1980).

[8] H. Schulz, Catal. Today **228**, 113 (2014).

[9] A. Khodakov, B. Peregryn, A. Lermontov, J.-S. Girardon, and S. Pietrzyk, Catal. Today **106**, 132 (2005).

[10] A. Y. Khodakov, Catal. Today **144**, 251 (2009).

[11] D. Sanfilippo, CATTECH **4**, 56 (2000).

[12] M. Z. Lukawski, B. J. Anderson, C. Augustine, L. E. Capuano Jr, K. F. Beckers, B. Livesay, and J. W. Tester, J. Petrol. Sci. Eng. **118**, 1 (2014).

[13] G. Haarlemmer, G. Boissonnet, E. Peduzzi, and P.-A. Setier, Energy **66**, 667 (2014).

[14] H. Sajjad, H. Masjuki, M. Varman, M. Kalam, M. Arbab, S. Imtenan, and S. Rahman, Renew. Sust. Energ. Rev. **30**, 961 (2014).

[15] B. Jager and R. Espinoza, Catal. Today **23**, 17 (1995).

[16] S. Freni, G. Calogero, and S. Cavallaro, J. Power Sources **87**, 28 (2000).

[17] W. McDowall and M. Eames, Energ. Policy **34**, 1236 (2006).

[18] K. Weissermel and H. Arpe, *Industrial Organic Chemistry* (Wiley-VCH, Weinheim, Germany, 2003).

[19] D. L. Trimm, Catal. Rev. **16**, 155 (1977).

[20] J. R. Rostrup-Nielsen, *Steam Reforming* (Wiley-VCH, Weinheim, Germany, 2008).

[21] T. Zhang and M. D. Amiridis, Appl. Catal. A **167**, 161 (1998).

[22] A. J. Akande, R. O. Idem, and A. K. Dalai, Appl. Catal. A **287**, 159 (2005).

[23] G. L. Bezemer, J. H. Bitter, H. P. C. E. Kuipers, H. Oosterbeek, J. E. Holewijn, X. Xu, F. Kapteijn, A. J. van Dillen, and K. P. de Jong, J. Am. Chem. Soc. **128**, 3956 (2006).

[24] J. L. Carter, J. A. Cusumano, and J. H. Sinfelt, J. Phys. Chem. **70**, 2257 (1966).

[25] D. G. Mustard and C. H. Bartholomew, J. Catal. **67**, 186 (1981).

[26] S. Rapagná, H. Provendier, C. Petit, A. Kiennemann, and P. Foscolo, Biomass Bioenerg **22**, 377 (2002).

[27] P. A. Chernavskii, J. A. Dalmon, N. S. Perov, and A. Y. Khodakov, Oil Gas Sci. Technol. **64**, 25 (2009).

[28] P. Chernavskii, A. Khodakov, G. Pankina, J.-S. Girardon, and E. Quinet, Appl. Catal. A **306**, 108 (2006).

[29] R. Chantrell, J. Popplewell, and S. Charles, IEEE T. Magn. **14**, 975 (1978).

[30] R. W. Chantrell and K. O'Grady, J. Phys. D Appl. Phys. **25**, 1 (1992).

[31] D. Weller and A. Moser, IEEE T. Magn. **35**, 4423 (1999).

[32] E. Duguet, S. Vasseur, S. Mornet, and J.-M. Devoisselle, Nanomed. **1**, 157 (2006).

[33] S. Mornet, S. Vasseur, F. Grasset, and E. Duguet, J. Mater. Chem. **14**, 2161 (2004).

[34] W. Elmore, Phys. Rev. **54**, 1092 (1938).

[35] J. Frenkel and J. Dorfman, Nature **126**, 274 (1930).

[36] C. Bean and I. S. Jacobs, J. Appl. Phys. **27**, 1448 (1956).

[37] C. Kittel, Phys. Rev. **70**, 965 (1946).

[38] W. F. Brown, J. Appl. Phys. **29**, 470 (1958).

[39] E. H. Frei, S. Shtrikman, and D. Treves, Phys. Rev. **106**, 446 (1957).

[40] L. Néel, Rev. Mod. Phys. **25**, 293 (1953).

[41] E. C. Stoner and E. P. Wohlfarth, Philos. T. R. Soc. Lond. **240**, 599 (1948).

[42] S. Bedanta and W. Kleemann, J. Phys. D: Appl. Phys. **42**, 013001 (2009).

[43] Q. A. Pankhurst, J. Connolly, S. Jones, and J. Dobson, J. Phys. D Appl. Phys. **36**, R167 (2003).

[44] L. Brannon-Peppas and J. O. Blanchette, Adv. Drug Deliver. Rev. **64**, 206 (2012).

[45] A. Jordan, R. Scholz, P. Wust, H. Fähling, and R. Felix, J. Magn. Magn. Mater. **201**, 413 (1999).

[46] A.-H. Lu, E. L. Salabas, and F. Schüth, Angew. Chem. Int. Edit. **46**, 1222 (2007).

[47] C. Chouly, D. Pouliquen, I. Lucet, J. Jeune, and P. Jallet, J. Microencapsulation **13**, 245 (1996).

[48] D.-X. Chen, A. Sanchez, E. Taboada, A. Roig, N. Sun, and H.-C. Gu, J. Appl. Phys. **105**, 083924 (2009).

[49] T. Sato, T. Iijima, M. Seki, and N. Inagaki, J. Magn. Magn. Mater. **65**, 252 (1987).

[50] A. Berkowitz, R. Kodama, S. A. Makhlouf, F. Parker, F. Spada, E. M. Jr., and S. Foner, J. Magn. Magn. Mater. **196**, 591 (1999).

[51] M. Mikhaylova, D. K. Kim, N. Bobrysheva, M. Osmolowsky, V. Semenov, T. Tsakalakos, and M. Muhammed, Langmuir **20**, 2472 (2004).

[52] D.-X. Chen, O. Pascu, A. Roig, and A. Sanchez, J. Magn. Magn. Mater. **322**, 3834 (2010).

[53] K. Krycka, R. Booth, J. Borchers, W. Chen, C. Conlon, T. Gentile, C. Hogg, Y. Ijiri, M. Laver, B. Maranville, et al., Physica B **404**, 2561 (2009).

[54] K. L. Krycka, R. A. Booth, C. R. Hogg, Y. Ijiri, J. A. Borchers, W. C. Chen, S. M. Watson, M. Laver, T. R. Gentile, L. R. Dedon, et al., Phys. Rev. Lett. **104**, 207203 (2010).

[55] K. Krycka, A. Jackson, J. Borchers, J. Shih, R. Briber, R. Ivkov, C. Grüttner, and C. Dennis, J. Appl. Phys. **109**, 07B513 (2011).

[56] V. Skumryev, S. Stoyanov, Y. Zhang, G. Hadjipanayis, D. Givord, and J. Nogues, Nature **423**, 850 (2003).

[57] R. Kodama, J. Magn. Magn. Mater. **200**, 359 (1999).

[58] F. Bödker, S. Mørup, and S. Linderoth, Phys. Rev. Lett. **72**, 282 (1994).

[59] D. A. Garanin and H. Kachkachi, Phys. Rev. Lett. **90**, 065504 (2003).

[60] L. Berger, Y. Labaye, M. Tamine, and J. M. D. Coey, Phys. Rev. B **77**, 104431 (2008).

[61] K. O'Grady, IEEE. T. Magn. **26**, 1870 (1990).

[62] M. Knobel, W. C. Nunes, L. M. Socolovsky, E. De Biasi, J. M. Vargas, and J. C. Denardin, J. Nanosci. Nanotechnol. **8**, 2836 (2008).

[63] S. Blundell, *Magnetism in Condensed Matter (Oxford Master Series in Physics)* (Oxford University Press, Oxford, UK, 2001), 1st ed.

[64] X. Chen, S. Bedanta, O. Petracic, W. Kleemann, S. Sahoo, S. Cardoso, and P. Freitas, Phys. Rev. B **72**, 214436 (2005).

[65] K. Binder and A. P. Young, Rev. Mod. Phys. **58**, 801 (1986).

[66] P. Poddar, T. Telem-Shafir, T. Fried, and G. Markovich, Phys. Rev. B **66**, 060403 (2002).

[67] A. P. Young, *Spin Glasses and Random Fields* (World Scientific, Singapore, 1997).

[68] P. Jönsson, M. F. Hansen, and P. Nordblad, Phys. Rev. B **61**, 1261 (2000).

[69] J. Du, B. Zhang, R. K. Zheng, and X. X. Zhang, Phys. Rev. B **75**, 014415 (2007).

[70] S. Mørup, M. Bo Madsen, J. Franck, J. Villadsen, and C. J. Koch, J. Magn. Magn. Mater. **40**, 163 (1983).

[71] A. Sugawara and M. R. Scheinfein, Phys. Rev. B **56**, R8499 (1997).

[72] L. Heyderman, H. Solak, C. David, D. Atkinson, R. Cowburn, and F. Nolting, Appl. Phys. Lett. **85**, 4989 (2004).

[73] S. Bedanta, T. Eimüller, W. Kleemann, J. Rhensius, F. Stromberg, E. Amaladass, S. Cardoso, and P. Freitas, Phys. Rev. Lett. **98**, 176601 (2007).

[74] K. Raj and R. Moskowitz, J. Magn. Magn. Mater. **85**, 233 (1990).

[75] M. De Cuyper and M. Joniau, Langmuir **7**, 647 (1991).

[76] R. Massart, IEEE. T. Magn. **17**, 1247 (1981).

[77] H. Bönnemann, W. Brijoux, R. Brinkmann, N. Matoussevitch, N. Waldöfner, N. Palina, and H. Modrow, Inorg. Chem. Acta. **350**, 617 (2003).

[78] J. Nogués and I. K. Schuller, J. Magn. Magn. Mater. **192**, 203 (1999).

[79] E. Eftaxias and K. Trohidou, Phys. Rev. B **71**, 134406 (2005).

[80] C. Vericat, M. Vela, G. Benitez, P. Carro, and R. Salvarezza, Chem. Soc. Rev. **39**, 1805 (2010).

[81] Z. Ban, Y. A. Barnakov, F. Li, V. O. Golub, and C. J. O'Connor, J. Mater. Chem. **15**, 4660 (2005).

[82] Z. Lu, M. D. Prouty, Z. Guo, V. O. Golub, C. S. Kumar, and Y. M. Lvov, Langmuir **21**, 2042 (2005).

[83] J. Zhang, M. Post, T. Veres, Z. J. Jakubek, J. Guan, D. Wang, F. Normandin, Y. Deslandes, and B. Simard, J. Phys. Chem. B **110**, 7122 (2006).

[84] W. Stöber, A. Fink, and E. Bohn, J. Colloid Interface Sci. **26**, 62 (1968).

[85] Y. Lu, Y. Yin, B. T. Mayers, and Y. Xia, Nano Lett. **2**, 183 (2002).

[86] A. P. Philipse, M. P. Van Bruggen, and C. Pathmamanoharan, Langmuir **10**, 92 (1994).

[87] C. R. Vestal and Z. J. Zhang, Nano Lett. **3**, 1739 (2003).

[88] F. G. Aliev, M. A. Correa-Duarte, A. Mamedov, J. W. Ostrander, M. Giersig, L. M. Liz-Marzán, and N. A. Kotov, Adv. Mater. **11**, 1006 (1999).

[89] L. Bedel, A. Roger, C. Estournes, and A. Kiennemann, Catal. Today **85**, 207 (2003).

[90] Y. Ichiyanagi and S. Yamada, Polyhedron **24**, 2813 (2005).

[91] F. Romero, J. Jiménez, and J. Del Cerro, J. Magn. Magn. Mater. **280**, 257 (2004).

[92] P. Chernavskii, A. Lermontov, G. Pankina, S. Torbin, and V. Lunin, Kinet. Catal. **43**, 268 (2002).

[93] W. Chu, P. A. Chernavskii, L. Gengembre, G. A. Pankina, P. Fongarland, and A. Y. Khodakov, J. Catal. **252**, 215 (2007).

[94] A. Barbier, A. Tuel, I. Arcon, A. Kodre, and G. A. Martin, J. Catal. **200**, 106 (2001).

[95] A. Barbier, A. Hanif, J.-A. Dalmon, and G. A. Martin, Appl. Catal. A **168**, 333 (1998).

[96] F. G. Silva, R. Aquino, V. Dupuis, J. Depeyrot, F. A. Tourinho, and R. Perzynski, in *Journal of Physics: Conference Series* (IOP Publishing, 2010), vol. 200, p. 072035.

[97] R. Aquino, J. Depeyrot, M. H. Sousa, F. A. Tourinho, E. Dubois, and R. Perzynski, Phys. Rev. B **72**, 184435 (2005).

[98] C. Herring and C. Kittel, Phys. Rev. **81**, 869 (1951).

[99] R. D. Desautels, E. Skoropata, Y.-Y. Chen, H. Ouyang, J. W. Freeland, and J. van Lierop, Appl. Phys. Lett. **99**, 262501 (2011).

[100] K. Tagaya, J. Phys. Soc. Jpn. **50**, 2533 (1981).

[101] J. T. Richardson and W. Milligan, Phys. Rev. **102**, 1289 (1956).

[102] L. F. Bates, *Modern Magnetism* (CUP Archive, Cambridge, UK, 1961).

[103] A. Aharoni, *Introduction to the Theory of Ferromagnetism* (Oxford University Press, Oxford, UK, 2000).

[104] K. Stewart, *Ferromagnetic Domains* (Cambridge University Press, Cambridge, UK, 1954).

[105] M. McElfresh, *Fundamentals of Magnetism and Magnetic Measurement* (1994).

[106] A. Barone and G. Paternò, *Physics and Applications of the Josephson Effect*, UMI Out-of-Print Books on Demand (Wiley, New Jersey, USA, 1982).

[107] N. H. Balshaw, *Practical cryogenics - an Introduction to Laboratory Cryogenics (Oxford Instruments)* (2001).

[108] C. Kittel, *Introduction to Solid State Physics* (Wiley, New Jersey, USA, 1971).

[109] J. Kortright, D. Awschalom, J. Stöhr, S. Bader, Y. Idzerda, S. Parkin, I. K. Schuller, and H.-C. Siegmann, J. Magn. Magn. Mater. **207**, 7 (1999).

[110] M. Fitzsimmons and I. K. Schuller, J. Magn. Magn. Mater. **350**, 199 (2014).

[111] W. Bragg and W. Bragg, Proc. R. Soc. London. Ser. A **88**, 428 (1913).

[112] A. Guinier, *X-ray Diffraction: in Crystals, Imperfect Crystals, and Amorphous Bodies* (Courier Dover Publications, New York, USA, 2013).

[113] B. Cullity, *Elements of X-ray diffraction*, Addison-Wesley metallurgy series (Addison-Wesley Pub. Co., Boston, USA, 1956).

[114] P. Forzatti and L. Lietti, Catal. Today **52**, 165 (1999).

[115] P. Arnoldy and J. Moulijn, J. Catal. **93**, 38 (1985).

[116] A. Parmaliana, F. Arena, F. Frusteri, and N. Giordano, J. Chem. Soc., Faraday Trans. **86**, 2663 (1990).

[117] D. B. Williams and C. B. Carter, *The Transmission Electron Microscope* (Springer, New York, USA, 1996).

[118] J. M. Thomas, W. J. Thomas, J. Anderson, and M. Boudart, *Principles and Practice of Heterogeneous Catalysis*, vol. 638 (VCH Weinheim, Weinheim, Germany, 1997).

[119] P. Lindner and T. Zemb, *Neutrons, X-rays and Light: Scattering Methods Applied to Soft Condensed Matter*, vol. 188 (North-Holland Amsterdam, Amsterdam, Netherlands, 2002).

[120] V. F. Sears, Neutron news **3**, 26 (1992).

[121] B. Chu and T. Liu, J. Nanopart. Res. **2**, 29 (2000).

[122] O. Glatter and O. Kratky, *Small Angle X-ray Scattering*, vol. 102 (Academic press London, London UK, 1982).

[123] J. W. Lynn, J. Appl. Phys. **75**, 6806 (1994).

[124] C. Dewhurst, Meas. Sci. Technol. **19**, 034007 (2008).

[125] T. Hyeon, Chem. Commun. **8**, 927 (2003).

[126] M. Roller, Inhalation Toxicology **21**, 144 (2009).

[127] T. Myojo, A. Ogami, T. Oyabu, Y. Morimoto, M. Hirohashi, M. Murakami, K. Nishi, C. Kadoya, and I. Tanaka, Advanced Powder Technology **21**, 507 (2010).

[128] M. V. Twigg and M. Twigg, *Catalyst Handbook* (CSIRO, Canberra, Australia, 1989).

[129] A. Y. Khodakov, W. Chu, and P. Fongarland, Chem. Rev. **107**, 1692 (2007).

[130] A. Haryanto, S. Fernando, N. Murali, and S. Adhikari, Energy Fuels **19**, 2098 (2005).

[131] E. Derouane, A. Simoens, C. Colin, G. Martin, J. Dalmon, and J. Védrine, J. Catal. **52**, 50 (1978).

[132] A. K. Gupta and M. Gupta, Biomaterials **26**, 3995 (2005).

[133] S. Sun and H. Zeng, J. Am. Chem. Soc. **124**, 8204 (2002).

[134] D.-H. Chen and S.-H. Wu, Chem. Mater. **12**, 1354 (2000).

[135] C. P. Collier, T. Vossmeyer, and J. R. Heath, Annu. Rev. Phys. Chem. **49**, 371 (1998).

[136] C. Suryanarayana and G. M. Norton, *X-ray Diffraction A Practical Approach* (Plenum Press, Berlin, Germany, New York, NY, USA, 1998).

[137] D. P. Lide, ed., *CRC Handbook of Chemistry and Physics* (CRC PRESS, Floride, USA, 2000), 81st ed.

[138] S. Deshpande, S. Patil, S. V. Kuchibhatla, and S. Seal, Appl. Phys. Lett. **87**, 133113 (2005).

[139] C. Igathinathane, L. Pordesimo, E. Columbus, W. Batchelor, and S. Methuku, Computers and electronics in agriculture **63**, 168 (2008).

[140] Q. Zhang, Y. Kusaka, X. Zhu, K. Sato, Y. Mo, T. Kluz, and K. Donaldson, J. Occup. Health **45**, 23 (2003).

[141] M. Bandyopadhyay and S. Dattagupta, Phys. Rev. B **74**, 214410_1 (2006).

[142] W. Luo, S. R. Nagel, T. Rosenbaum, and R. Rosensweig, Phys. Rev. Lett. **67**, 2721 (1991).

[143] G. A. Held, G. Grinstein, H. Doyle, S. Sun, and C. B. Murray, Phys. Rev. B **64**, 012408 (2001).

[144] Y. Chen, D.-L. Peng, D. Lin, and X. Luo, Nanotechnology **18**, 505703 (2007).

[145] R. W. Chantrell, N. Walmsley, J. Gore, and M. Maylin, Phys. Rev. B **63**, 024410 (2000).

[146] P. Hendriksen, S. Linderoth, and P.-A. Lindgård, J. Magn. Magn. Mater. **104**, 1577 (1992).

[147] P. Allia, M. Coisson, P. Tiberto, F. Vinai, M. Knobel, M. A. Novak, and W. C. Nunes, Phys. Rev. B **64**, 144420 (2001).

[148] C. Cannas, G. Concas, D. Gatteschi, A. Falqui, A. Musinu, G. Piccaluga, C. Sangregorio, and G. Spano, Phys. Chem. Chem. Phys. **3**, 832 (2001).

[149] O. Petracic, X. Chen, S. Bedanta, W. Kleemann, S. Sahoo, S. Cardoso, and P. Freitas, J. Magn. Magn. Mater. **300**, 192 (2006).

[150] J. M. Vargas, W. C. Nunes, L. M. Socolovsky, M. Knobel, and D. Zanchet, Phys. Rev. B **72**, 184428 (2005).

[151] L. B. Kiss, J. Söderlund, G. A. Niklasson, and C. G. Granqvist, Nanotechnology **10**, 25 (1999).

[152] J. Soderlund, L. B. Kiss, G. A. Niklasson, and C. G. Granqvist, Phys. Rev. Lett. **80**, 2386 (1998).

[153] H. Danan, A. Herr, and A. J. P. Meyer, J. Appl. Phys. **39**, 669 (1968).

[154] F. Silva, R. Aquino, J. Depeyrot, F. Tourinho, V. Dupuis, and R. Perzynski, Phys. Proc. **9**, 28 (2010).

[155] S. E. Apsel, J. W. Emmert, J. Deng, and L. A. Bloomfield, Phys. Rev. Lett. **76**, 1441 (1996).

[156] I. M. L. Billas, A. Chtelain, and W. A. d. Heer, Science **265**, pp. 1682 (1994).

[157] M. B. Knickelbein, J. Chem. Phys. **116**, 9703 (2002).

[158] C. Yang and C. W. Garl, J. Phys. Chem. **61**, 1504 (1957).

[159] B. B. Wayland and M. E. Abd-Elmageed, J. Am. Chem. Soc. **96**, 4809 (1974).

[160] S. Mørup and E. Tronc, Phys. Rev. Lett. **72**, 3278 (1994).

[161] M. F. Hansen and S. Morup, J. Magn. Magn. Mater. **184**, 262 (1998).

[162] C. A. Neugebauer, Phys. Rev. **116**, 1441 (1959).

[163] W. H. Meiklejohn and C. P. Bean, Phys. Rev. **105**, 904 (1957).

[164] C. Li and Y.-W. Chen, Thermochim. Acta **256**, 457 (1995).

[165] *QD MPMS Appliation Note 1014-210: Oxygen Contamination* (1997).

[166] D. A. van Leeuwen, J. M. van Ruitenbeek, L. J. de Jongh, A. Ceriotti, O. D. Pacchioni, G. Häberlen, and N. Rösch, Phys. Rev. Lett. **73**, 1432 (1994).

[167] A. T. Bell, Science **299**, 1688 (2003).

[168] D. Duprez, Appl. Catal. A **82**, 111 (1992).

[169] F. Besenbacher, I. Chorkendorff, B. S. Clausen, B. Hammer, A. M. Molenbroek, J. K. Nrskov, and I. Stensgaard, Science **279**, 1913 (1998).

[170] J. Richardson, M. Lei, B. Turk, K. Forster, and M. V. Twigg, Appl. Catal. A **110**, 217 (1994).

[171] J. Sehested, A. Carlsson, T. Janssens, P. Hansen, and A. Datye, J. Catal. **197**, 200 (2001).

[172] A. K. Datye, Q. Xu, K. C. Kharas, and J. M. McCarty, Catal. Today **111**, 59 (2006).

[173] J. C. Yang, M. W. Small, R. V. Grieshaber, and R. G. Nuzzo, Chem. Soc. Rev. **41**, 8179 (2012).

[174] C. H. Bartholomew and R. J. Farrauto, J. Catal. **45**, 41 (1976).

[175] K. S. W. Sing, Pure Appl. Chem. **57**, 603 (1985).

[176] P. C. Carman and F. A. Raal, Proc. R. Soc. London Ser. A **209**, 59 (1951).

[177] G. A. Somorjai, *Introduction to Surface Chemistry and Catalysis* (Wiley, New Jersey, USA, 1994), 1st ed.

[178] F. Delannay, *Characterization of Heterogeneous Catalysts*, Chemical industries (M. Dekker, New York, USA, 1984).

[179] D. Lide, *CRC Handbook of Chemistry and Physics, 85th Edition*, CRC Handbook of Chemistry and Physics, 85th Ed (Taylor & Francis, Oxford, UK, 2004).

[180] P. Webb, C. Orr, and M. I. Corporation, *Analytical Methods in Fine Particle Technology* (Micromeritics Instrument Corporation, Georgia, USA, 1997).

[181] S. Lowell, *Characterization of Porous Solids and Powders: Surface Area, Pore Size and Density*, Particle Technology Series (Springer, New York, USA, 2004).

[182] S. Wang and G. Lu, Appl. Catal. A **169**, 271 (1998).

[183] W. P. Davey, Phys. Rev. **25**, 753 (1925).

[184] D. Rodic, V. Spasojevic, V. Kusigerski, R. Tellgren, and H. Rundlof, Phys. Status Solidi B **218**, 527 (2000).

[185] P. S. Prevéy, Advances in X-ray Analysis **29**, 103 (1986).

[186] *QD MPMS Aplication Note 1014-201: Sample Mounting Considerations* (2000).

[187] F. Davar, Z. Fereshteh, and M. Salavati-Niasari, J. Alloy. Compd. **476**, 797 (2009).

[188] H. Kachkachi, A. Ezzir, M. Nogués, and E. Tronc, Eur. Phys. J. B **14**, 681 (2000).

[189] S. Shylesh, V. Schünemann, and W. Thiel, Angew. Chem. Int. Edit. **49**, 3428 (2010).

[190] A. Wiedenmann, J. Appl. Crystallogr. **33**, 428 (2000).

[191] A. Petoukhov, K. Andersen, D. Jullien, E. Babcock, J. Chastagnier, R. Chung, H. Humblot, E. Lelièvre-Berna, F. Tasset, F. Radu, et al., Physica B **385**, 1146 (2006).

[192] M. Blume, Phys. Rev. **130**, 1670 (1963).

[193] A. Wiedenmann, Physica B **356**, 246 (2005).

[194] D. Ballard, P. Cheshire, G. Longman, and J. Schelten, Polymer **19**, 379 (1978).

[195] J. S. Pedersen, J. Appl. Crystallogr. **27**, 595 (1994).

[196] S. R. Kline, J. Appl. Crystallogr. **39**, 895 (2006).

[197] J. Pleštil, H. Pospíšil, P. Kadlec, Z. Tuzar, J. Kříž, and V. Gordeliy, Polymer **42**, 2941 (2001).

[198] G. Beaucage, J. Appl. Crystallogr. **28**, 717 (1995).

[199] D. Farrell, Y. Ijiri, C. Kelly, J. Borchers, J. Rhyne, Y. Ding, and S. Majetich, J. Magn. Magn. Mater. **303**, 318 (2006).

[200] A. Dianoux, G. Lander, P. L. G. Institut Max von Laue, and I. Laue-Langevin, *Neutron Data Booklet* (Old City, 2001).

[201] W. Jian-Ping and L. He-Lie, J. Magn. Magn. Mater. **131**, 54 (1994).

[202] W.-H. Li, S. Wu, C. Yang, S. Lai, K. Lee, H. Huang, and H. Yang, Phys. Rev. Lett. **89**, 135504 (2002).

[203] X. Zheng, H. Kubozono, H. Yamada, K. Kato, Y. Ishiwata, and C. Xu, Nature Nano. **3**, 724 (2008).